

ION RUNAWAY DURING MAGNETIC RECONNECTION IN
THE REVERSED-FIELD PINCH

by

Scott Eilerman

A dissertation submitted in partial fulfillment of
the requirements for the degree of

Doctor of Philosophy

(Physics)

at the

UNIVERSITY OF WISCONSIN – MADISON

2014

Defended on 7 May 2014

Dissertation approved by the following members of the Final Oral Committee:

Cary Forest · Professor of Physics

John Sarff · Professor of Physics

Jan Egedal · Professor of Physics

Jay Anderson · Doctor of Physics

Ellen Zweibel · Professor of Astronomy

© Copyright Scott Eilerman 2014

All Rights Reserved

Abstract

The anomalous heating and energization of ions during magnetic reconnection events in astrophysical and laboratory plasmas has been an ongoing research topic for decades. Numerous measurements have been made during impulsive bursts of reconnection in the reversed-field pinch to further our understanding of the heating process. Discoveries have been made regarding the conditions necessary for heating, its scaling with various plasma parameters, and the anisotropies and other features associated with the resulting distribution; however, no one mechanism for the conversion of magnetic to kinetic energy has been definitively identified that explains all of the observed phenomena. This work introduces new information to the ongoing study by using a neutral beam injector to study the effects of reconnection on a well-known population of ions with initial energies much higher than the bulk population. The acceleration/energization of the fast ions is measured using a new neutral particle analyzer which collects the charge exchange products of the fast ions and the background neutral gas. Measurements indicate an energy gain of 1-10 keV, depending on plasma conditions and initial ion energy (10-25 keV). The acceleration is well described by runaway in a parallel electric field that is inductively generated due to the change in global magnetic flux during reconnection-driven current relaxation. Equilibrium reconstructions indicate this electric field can range from 50-100 V/m and typically lasts around 200 μ s.

The effect of the electric field on fast particles has been modeled using a test particle formulation and using the CQL3D Fokker-Planck solver. Both models predict particle acceleration in agreement with measurements. However, the predicted evolution of the bulk and impurity ion distributions from the same electric field greatly differ from previous measurements. It is well known that $\langle \tilde{\mathbf{v}} \times \tilde{\mathbf{b}} \rangle$ and other turbulent

electromotive forces are of great importance to the dynamics of the thermal particles; however, the large gyro-orbit and altered rotational transform of the magnetically decoupled fast ions allow them to largely ignore the magnetic fluctuations and directly accelerate in the presence of the inductive electric field. This work motivates the consideration of multiple mechanisms of heating and energization for particles in different regimes of susceptibility to fluctuation-based terms in the parallel force balance.

Acknowledgements

“In all your travels, have you ever seen a star go supernova? No? Well, I have. I saw a star explode and send out the building blocks of the Universe. Other stars, other planets and eventually other life. A supernova! Creation itself! I was there. I wanted to see it and be part of the moment. And you know how I perceived one of the most glorious events in the universe? With eyes designed to perceive only a tiny fraction of the EM spectrum. With ears designed only to hear vibrations in the air. I want to see gamma rays! I want to hear X-rays! I want to smell dark matter! I want to reach out with something other than these prehensile paws, and feel the wind of a supernova flowing over me. I can know much more. I can experience so much more.”

— Brother Cavil (paraphrased), *Battlestar Galactica*

Genocidal robots aside, I believe the quote above summarizes the aspirations of all experimental physicists. Physics is humanity’s eternal quest to understand and describe the beauty of the natural world, the underlying mathematical principles that are the foundation of our existence. When we reach the limits of our own abilities to observe, we must find new ways, new instruments, new techniques for looking under the hood of the universe. That is the charge of experimental physics, and I am extremely proud and grateful that I have been given the opportunity to contribute to such a profound cause. However, I have not done it alone. In addition to the many great scientists whose shoulders I stand upon, I would like to take a moment to thank some of the people who have directly contributed to my journey as a physicist and as a person.

First, I would like to thank the many teachers and professors who have instructed

me over the 23 years I've been a student. If it takes a village to raise a child, then it takes a small country to educate a physicist. There are two teachers who I'd like to thank for their exceptional impact: Ms. McCormick, thank you for teaching an entire generation of 5th graders to respect and protect this beautiful planet that we live on, and Mr. Krauskopf, thank you for challenging me, believing in me, and teaching me to always give 110%.

Of course, this work would not be possible without the array of outstanding scientists, engineers, students, and administrative staff that comprise the MST team. Madison is truly an outstanding place to learn and practice plasma physics, and every member of this research group contributes to the success of the students who graduate. Thank you to the NSF, DOE, and CMSO for funding the outstanding science that goes on here.

To my advisor, Cary Forest, and the principal investigator for MST, John Sarff: thank you for your guidance, your leadership, your extensive knowledge, and your ability to place this work in context within the enormous field of plasma physics.

To my supervisor and mentor, Jay Anderson: almost every idea and result in this thesis originated from conversations in your office. For your patience in teaching and reteaching me the fundamentals of plasma physics, for our numerous brainstorming sessions, and for reviewing every poster, talk, and paper I've produced – thank you.

To the many J's of the NBI/NPA group: Jay, Josh, Jon, Jeff, James, Jungha, Jordan, Jerry (and also Mark, Deyong, Bill, Eli, Liang, Steve – get your names in order), thank you for the countless hours operating, fixing, and discussing results from the neutral beams and NPAs. What started as a small hardware meeting has become a forum for ideas and scientific discussion and a driving force behind a significant amount of MST's research.

Deyong, Josh, and Jungha - thank you for your instrumental work (ha ha) in

the development of the ANPA. Diagnostics can be fickle beasts, but together we've managed to tame this one and teach it to do our bidding.

To the other UW graduate students in my year – from weekend-long homework sessions to qualifying exams to corn maze competitions to closing the bars, you guys have been through all of this with me and that has made a huge difference. Solitary confinement is a bummer; having a rag-tag group of inmates to plot your escape with is far more entertaining.

To the Wright State crew – you guys rock.

To my parents and brother: you raised me well, and no amount of thanks can ever repay that. I know you are proud of me, but you should also be proud of yourselves. You've taught me kindness, respect, and generosity – things the world could use quite a bit more of. You've always respected and supported my decisions, given me advice when I've asked for it, and let me find my own way when I haven't. You've provided a foundation of love and warmth from which all of my endeavors have stemmed. Thank you.

To my cat, Kaylee: thank you for your repeated attempts to contribute to this thesis. Unfortunately, the committee did not agree with your assertion that “the mechanism responsible for anomalous ion heating in the reversed-field pinch is
 qqqqqqqqqqqqwwwwwwwwaaaaaaaSSSSSSSSSSSS`~~~~~!!!eeeeee.”

Finally, to my wife, Crystal – no words can express my gratitude for your endless understanding, encouragement, love, and support. Few people look back at their work in graduate school as “fun,” but it will be hard for me to remember this time in my life without remembering the relationship we've built and the laughs we've shared. This degree has been hard at times, but it would have been so much harder without you. Thank you so much, for everything.

Contents

Abstract	i
Acknowledgements	iii
List of Figures	x
Chapter 1: Introduction	1
1.1 The reversed-field pinch	3
1.2 The Madison Symmetric Torus	5
Neutral Beam Injection	5
The sawtooth cycle in MST	9
Magnetic reconnection	11
1.3 Previous results: anomalous ion heating during MST sawteeth	11
Chapter 2: Overview and development of the ANPA	15
2.1 Basics of neutral particle analysis	15
2.2 Hardware design	16
Alignment	20
2.3 Calibration	20
Ion source design	20
Procedure	24
Results	26
2.4 Modeling of signal contributions on different viewports	33

2.5	Initial survey data and analysis techniques	43
	F=0 plasmas	43
	“Standard” (F=-0.2) plasmas	44
	Enhanced confinement (“EC”) plasmas	45
	PPCD	46
	Deconvolving contributions from changes in neutral density	47
	QSH/SHAx	49
	Bulk plasma measurements	50
2.6	Noise analysis and subtraction	52
2.7	Summary	55
Chapter 3: Modeling of the sawtooth-induced electric field		56
3.1	Ion runaway physics	56
3.2	Calculation of plasma friction	61
3.3	Calculation of the electric field profile	63
3.4	Expected energization of fast ions	68
Chapter 4: Measurements and analysis of fast ion energization during reconnection events		70
4.1	Analysis techniques	70
	Sawtooth ensembling	70
	Average energy formulation	72
	Sawtooth-triggered beam turn-off	75
	Removing contributions from the half-energy beam component	78
	Error estimation	80
4.2	Experiments to characterize fast ion energization	81
	Scaling with electric field strength	81

Scaling with initial ion energy	83
Deceleration in counter- I_p beam injection	85
Dependence on ANPA viewing angle	89
4.3 Summary of results	91
Chapter 5: Bulk ion heating and other implications	92
5.1 Modeling with the CQL3D code	93
The Fokker-Planck equation	93
Modeling the fast ion tail	95
Modeling bulk and impurity ions	98
Effects on thermal electrons	100
5.2 Discussion	102
Chapter 6: Conclusions	107
6.1 Summary of key results	107
Development of the ANPA diagnostic	108
Ion runaway during reconnection in the RFP	108
Applicability to thermal ion heating	109
6.2 Suggestions for future work	110
Determining the threshold for runaway applicability	110
Studies of core and edge reconnection events	110
Investigation of other energization phenomena	112
Measurements of the high-energy tail	113
Development of additional ion diagnostics	114
Bibliography	116
Appendix A: D_α emission measurements and neutral density modeling	127

A.1	Overview	127
A.2	Expansion and calibration of D_α detectors	129
A.3	NENE Monte Carlo code	131
	Motivation	131
	Description of inputs, outputs, and particle tracking	132
	Fitting to D_α measurements	133
	Uncertainty and comparison to other estimates	137
A.4	Summary and future work	139
Appendix B: Sign conventions in MSTFit, MDSPlus, and machine		
	coordinates	142
B.1	Introduction	142
B.2	MST sign conventions	143
B.3	Sign inconsistencies in the MDSPlus database	145
	Reversing the direction of the plasma current (“counter-injection”) .	145
B.4	Sign conventions and inconsistencies in MSTFit	146
	The <code>out</code> structure	146
	The <code>bfield.pro</code> routine	147
B.5	Calculating electric fields	148
	Using multiple MSTFit files to study time dependence	148
	Toroidal electric field using poloidal magnetic field	149
	Poloidal electric field using toroidal magnetic field	151
	Using fluxes instead of fields	152
B.6	Clarification of gap voltage directions	155
B.7	Sawtooth-generated electric fields with respect to NBI-born fast ions .	155
B.8	Summary	156

List of Figures

1.1	A diagram of the RFP configuration	3
1.2	A typical q profile in the Madison Symmetric Torus	4
1.3	TRANSP modeling of the fast ion distribution in MST	6
1.4	Energy dependence of the fusion cross-section	8
1.5	The fast ion rotational transform differs from q_m	8
1.6	Fast ion guiding center in a stochastic magnetic field	9
1.7	The peaked current density profile relaxes during a sawtooth event.	10
1.8	Magnetic energy is the ultimate energy source for ion heating in MST	12
1.9	A non-Maxwellian tail is generated at the sawtooth crash	13
2.1	Schematic diagram of the ANPA	17
2.2	Photograph of SEM detectors	18
2.3	An overhead view of MST showing the locations of the NBI, DNB, and two ANPA views.	19
2.4	Photograph of mounting structure for ANPA tangential view	21
2.5	Schematic of ANPA calibration source	22
2.6	Photograph of cylindrical mesh (calibration source)	22
2.7	Modeling of effect of copper shielding on equipotential surfaces	23
2.8	Photograph of copper shielding (calibration source)	23

2.9	Diagram of ANPA calibration setup	25
2.10	ANPA energy calibration data	27
2.11	Molecular contributions to calibration data	27
2.12	Channel output for varying voltage on the steering capacitor	29
2.13	Effects of ANPA steering capacitor on energy bins and relative gain	30
2.14	Effects of electrostatic focusing lens on energy bins and relative gain	31
2.15	Diagram of Channeltron operation	31
2.16	Effects of detector bias voltage on energy bins and relative gains	32
2.17	Path length vs. r/a for the tangential, radial ANPA views	35
2.18	Line of sight signal modeling, radial view	36
2.19	Line of sight signal modeling, tangential view	37
2.20	Line of sight signal modeling, tangential view with DNB	38
2.21	Line of sight signal modeling, tangential view with DNB, PPCD	39
2.22	Fast ion loss rate during EPMS suggest core-localization of measurement	41
2.23	Edge particle orbits transition from lost to confined in low-current discharges	42
2.24	Sample ANPA data from an $F=0$ discharge	43
2.25	Sample ANPA data from an $F=-0.2$ discharge	44
2.26	Sample ANPA data from an $F=-0.3$ “EC” discharge	45
2.27	Sample ANPA data from a PPCD discharge	46
2.28	Sample PPCD data with D_α normalization	48
2.29	Sample ANPA data from a QSH discharge	50
2.30	Sample ANPA data from an EC discharge with no NBI	51
2.31	Scatterplots show the relationship between each ANPA channel and the noise detector	53
2.32	Radial ANPA data before and after noise subtraction	54

3.1	Contours of E^*/E are plotted vs. Z_{eff} and trapped electron fraction . . .	60
3.2	Trapped fraction and E^*/E are plotted for MST parameters	61
3.3	Friction for a test electron and ion in a standard MST plasma	62
3.4	Dependence of friction on plasma parameters	63
3.5	The toroidal electric field is calculated from the change in poloidal magnetic flux through a circular disc in the $R - \phi$ plane	64
3.6	The poloidal electric field is calculated from the change in toroidal magnetic flux through a circular surface in the $r - \theta$ plane	65
3.7	Toroidal and poloidal magnetic field profiles before and after a sawtooth event	66
3.8	Core electric field throughout a sawtooth crash	67
3.9	Toroidal, poloidal, and parallel components of the electric field at its peak.	67
3.10	100 predictions of ion energization with Monte Carlo variation in assumptions	69
4.1	An example of sawtooth-ensampled data	71
4.2	Average energy calculations for sample distribution functions	74
4.3	Approximate distribution functions before and after a sawtooth	75
4.4	Average energy calculated throughout a sawtooth cycle	76
4.5	Sawtooth-triggered NBI turn-off provides a clearer picture of energization	78
4.6	Sawtooth-triggered NBI turn-off in a colder plasma	79
4.7	The fast ions can be energized multiple times at subsequent reconnection events	79
4.8	Spread in individual sawteeth used for error calculation	81
4.9	Fast ion acceleration scaling with electric field	82
4.10	Fast ion acceleration scaling with drop in stored magnetic acceleration .	83

4.11	Fast ion acceleration scaling with initial ion energy	84
4.12	Beam energy scans at low and high density	85
4.13	Diagrams of electric field orientation in co- and counter-injection	86
4.14	Deceleration measurement in counter-injection	87
4.15	Beam energy scan in counter-injection	88
4.16	Radial ANPA data show no sawtooth acceleration	89
4.17	Ensembled radial ANPA data show no sawtooth acceleration	90
5.1	CQL3D results for fast ion acceleration	96
5.2	Evolution of the fast ion distribution function	97
5.3	CQL3D results for bulk and impurity ions	99
5.4	Evolution of electron density and temperature during a sawtooth	101
5.5	ANPA measurements of the bulk (no NBI) fast ion tail	105
6.1	Summary of ion runaway results	109
6.2	ANPA signal reduction during a core event	111
6.3	Energization observed during QSH ramp-up	112
A.1	Diagram of the D_α boxport and detectors	129
A.2	Diagram of the D_α calibration setup	130
A.3	Measured transmission function of a D_α bandpass filter	131
A.4	$\langle \sigma v \rangle_{ionization}$ vs. T_e	132
A.5	Flowchart summarizing the interaction between NENE and D_α emission analysis	134
A.6	n_0 and simulated D_α emission is plotted for three basis profiles and the data-constrained solution	136
A.7	Comparison of fit quality and n_0 before and after improvement of the D_α array and fitting process	137

A.8	A series of equilibrium and NENE reconstructions show increases in n_0 at sawtooth events	138
A.9	Comparison of n_0 and χ_{red}^2 with variation in the sourced neutral energy .	139
B.1	Toroidal and poloidal cross-sections of MST with coordinate, current, field, and flow directions	143
B.2	Diagram showing the toroidal electric field generated by a change in poloidal magnetic flux	149
B.3	Diagram showing the poloidal electric field generated by a change in toroidal magnetic flux	151

Chapter 1

Introduction

The topic of anomalous ion heating in laboratory plasmas has been studied since the early years of fusion research. Initial measurements of ion temperatures in excess of expectations from collisional coupling to the Ohmically heated electrons can be traced back to results from ZETA in 1962 [1]. Since then, numerous other devices have reported similar observations [2–5]: some mechanism within the plasma must be responsible for providing additional energy to the ion population. Whether tied to understanding a confinement-threatening instability or potentially harnessed as a method for increasing plasma temperature and thus fusion output, the mechanism or mechanisms behind this anomalous ion heating process are of great interest to fusion research.

Additionally, such mechanisms are of interest in astrophysical research, where problems such as heating of the solar corona and generation of high-energy cosmic rays have been attributed to self-organized plasma processes that are not fully understood [6–14]. One such process, magnetic reconnection, was proposed by Sweet and Parker in 1956 and has been a topic of subsequent study ever since [15]. Many revisions [16,17] have been made to the original model, and all allow for the conversion of free

magnetic energy into kinetic or thermal particle energy, but no universally applicable model has been proposed (based solely on reconnection or on other processes) that explains all of the anomalous ion heating observations throughout the laboratory and the cosmos [18].

This thesis adds yet another observation to the long list of ion energization measurements in the reversed-field pinch configuration. Suprathermal ions introduced to the plasma via neutral beam injection are observed to accelerate well above their initial injection energy during reconnection-driven plasma relaxation events. While previous ion heating measurements at these “sawtooth” events have helped constrain which heating theories may be applicable in the RFP, the measurements of fast ion acceleration in this thesis can be clearly traced to the mechanism responsible: an inductive electric field generated during the large-scale magnetic flux change at the event.

Perhaps expectedly, the proposed mechanism cannot explain all previous ion heating measurements. However, the conclusion that this mechanism is at work in MST plasmas represents an important insight: multiple heating/energization mechanisms **must** be considered for particles in different regimes. The notion that one process will explain the heating of all types of ions in plasmas ranging from tabletop experiments to reactors to the intergalactic medium is aesthetically and scientifically appealing, but must ultimately give way to a more nuanced approach.

The remainder of this thesis is laid out as follows: Chapter 1 provides additional historical context and background information; Chapter 2 details the Advanced Neutral Particle Analyzer (ANPA) diagnostic that is used to measure the acceleration of suprathermal ions; Chapter 3 reviews the theory on ion runaway in an electric field and the relevant calculations for MST plasmas; Chapter 4 presents the primary experimental measurements and comparison with the runaway theory; Chapter 5 ad-

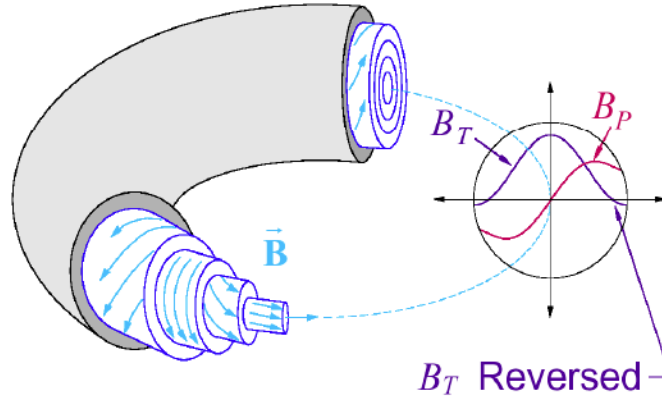


Figure 1.1: A diagram of the RFP configuration. The toroidal and poloidal magnetic fields are of similar amplitude, and the toroidal field reverses at the plasma edge.

dresses the applicability of the runaway mechanism to bulk and impurity ions; and finally, Chapter 6 summarizes the major findings and suggestions for future work.

1.1 The reversed-field pinch

The reversed-field pinch (RFP) concept was born out of analysis of the self-organized magnetic field configuration observed after the external power drive was turned off in the ZETA toroidal pinch [19]. In 1974, John Bryan Taylor developed the theoretical framework for the relaxation of the plasma into a minimum-energy state in which the toroidal field at the edge of the plasma is in the opposite direction of the core toroidal field [20]. This field reversal is one of the defining characteristics of the reversed-field pinch, the other being the relatively weak amplitude of the toroidal magnetic field ($B_\phi/B_\theta \approx 1$) compared to the tokamak ($B_\phi \gg B_\theta$). A parameter used to characterize the degree of reversal in RFP plasmas is the reversal parameter F , defined as the ratio of the toroidal field at the wall to the average toroidal field:

$$F = \frac{B_\phi(a)}{\langle B_\phi \rangle} \quad (1.1)$$

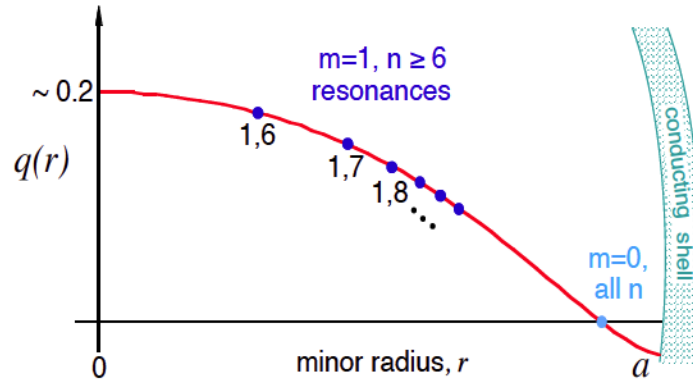


Figure 1.2: A typical q profile in the Madison Symmetric Torus. Tearing modes are resonant where the q profile is equal to a rational fraction (e.g. $1/5$, $1/6$, etc..).

The low applied toroidal field makes the RFP appealing as a reactor concept from an engineering perspective, as the magnetic field at the external magnets is very low and thus superconducting magnets are not necessary. In fact, almost all of the magnetic field in the plasma is self-generated by the current within the plasma. The low toroidal field does have some consequences, however. The plasma “safety factor,” so called because of its relation to how stable the plasma is to a class of current-driven tearing instabilities, is defined as:

$$q = \left\langle \frac{rB_\phi}{RB_\theta} \right\rangle \quad (1.2)$$

where $\langle \rangle$ denotes an average of the enclosed quantities around a surface of constant poloidal flux.

In the tokamak, where $B_\phi \gg B_\theta$, the safety factor is above 1 everywhere. However, in the RFP, $q(r)$ is less than one throughout the plasma, becoming negative at the edge of the plasma where the toroidal field flips sign. Points where the q profile is a rational number (m/n , with m and n being whole numbers) are known as “rational surfaces.” At these rational surfaces, the resonance condition $\mathbf{k} \cdot \mathbf{B} = 0$ can be met leading to the growth of tearing mode instabilities. A number of $m = 1$ rational

surfaces are resonant within a typical MST plasma, and the location where $q = 0$ (referred to as the “reversal surface”) is host to a multitude of tearing modes with $m = 0$. The dynamics of the RFP are heavily influenced by these tearing modes and will be discussed in more detail later in this chapter.

1.2 The Madison Symmetric Torus

The Madison Symmetric Torus is a reversed-field pinch device built at the University of Wisconsin–Madison in 1988 [21]. One of the defining features of MST is a close-fitting aluminum shell that serves as both the vacuum vessel and a single-turn toroidal field coil. The 5 cm thick wall is treated as an ideal boundary as the resistive wall time is longer than a typical plasma discharge (~ 40 -80 ms). Despite a carbon limiter and graphite tiles keeping the bulk of the plasma off of the wall, a significant amount of plasma-wall interaction and fuel loading/recycling occurs.

The vessel itself has a major radius of $R = 1.5$ m and a minor radius $a = 0.52$ m. Plasma currents typically range from 200–600 kA with magnetic fields averaging 0.2–0.5 T and particle densities on the order $n \sim 10^{19}$ m⁻³. Electron and ion temperatures can range from 200 - 2000 eV depending on plasma conditions. “Standard” operation entails a reversal parameter $F \sim -0.2$ with $q(0) \sim 0.2$; however, non-reversed and “deep reversal” discharges with respective reversal parameters $F = 0$ and $F \leq -0.3$ are also easily achieved. If desired, MST can even be operated at low currents as a tokamak with $q(a) > 1$.

Neutral Beam Injection

Neutral beam injection is a common technique for heating tokamak plasmas, and is used in the RFP for electron heating and a host of scientific studies [22–27]. A

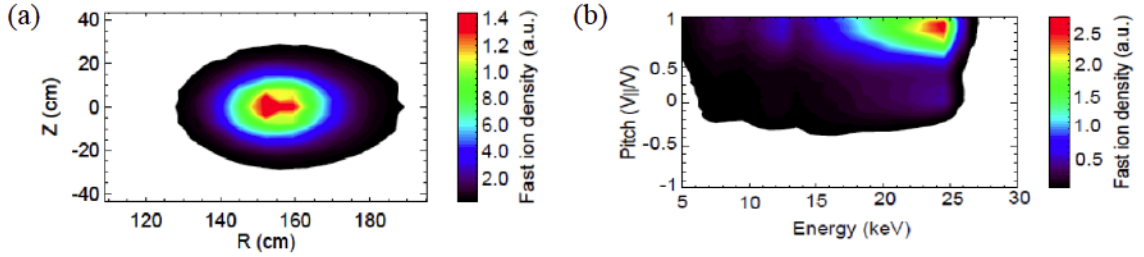


Figure 1.3: TRANSP modeling of the fast ion distribution in MST. The majority of the fast ions are core-localized (a) and have high pitch (b).

1 MW (25 keV, 40A) neutral beam injector (NBI) was designed and built by the Budker Institute of Nuclear Physics (BINP) and installed on MST in 2010. A pair of arc discharges ionize the working gas, which can be hydrogen, deuterium, or a mix of the two. A series of three high-voltage grids accelerates and focuses the ions into a beam, and the ion beam passes through a neutralizing chamber where the ions reneutralize via charge exchange with a background neutral gas. The result is a beam of high-energy neutral H or D atoms injected tangentially into MST. Most of the neutrals will be at the primary beam energy, however, some will be at lower energies due to the presence of H_2 , H_3 , and H_2O molecules in the beam fuel. At maximum beam energy, the beam is rated to have roughly 86% of the neutrals at full energy, 10% at half-energy, 2% at 1/3 energy, and 2% at 1/18 energy. Once inside the plasma, the neutrals will reionize through electron impact ionization, ion impact ionization, or neutral-ion charge exchange (the dominant process at 25 keV). Those that are not ionized are measured with a “shine-through” detector on the far wall of the machine [23].

The beam was primarily designed for heating and current drive experiments, although a number of interesting physics results have arisen from the relatively well-confined population of fast ions. The TRANSP software and NUBEAM module have been used to model the neutral beam deposition and resulting fast ion population

(Figure 1.3). The TRANSP results provide a good estimate of the fast ion distribution, but there are two known sources of error in this model. First, TRANSP uses the toroidal magnetic flux as a radial coordinate and thus cannot model outside of the reversal surface because the radial coordinate becomes multi-valued. A work-around for this problem is to model $F=0$ plasmas or simply ignore the outer portion of reversed plasmas. The second error is that TRANSP does not consider non-classical effects such as energetic particle driven modes which are known to be active during beam injection in MST [26, 28]. These modes are shown to limit the total fast ion content to as little as half [29] of the expected population at full injection current.

Before the installation of the ANPA, the primary method of measuring fast ions in MST was neutron detection. MST typically runs with deuterium as its working gas, and even in the coldest plasmas, some amount of D-D fusion occurs. Because the fusion cross section is heavily dependent on ion energy (Figure 1.4), the number of neutrons produced increases rapidly in hotter plasmas or if fast deuterium ions are being injected with NBI. Unless an experiment calls for a full hydrogen or full deuterium beam, the NBI is typically run with a fuel mix of 95-97% hydrogen and 3-5% deuterium so that neutrons can be used as rough indicator of the fast ion content in the plasma.

The neutrons are detected using a plastic scintillator coupled to a photomultiplier tube. The scintillator is placed under a pile of lead bricks so that only neutrons are able to create a signal. There is no attempt at collimation, so the measured signal is representative of the total number of fast ion - thermal ion collisions. Recent work has been done (W. Capecchi) to add additional detectors and improve the linearity of the measurement in a variety of plasma and beam conditions.

The confinement time of the NBI-sourced fast ions can be measured using the decay of the neutron flux signal after the NBI is turned off [25, 30]. Neglecting the

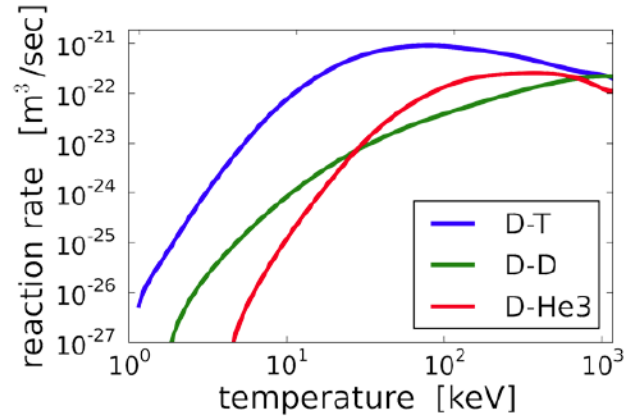


Figure 1.4: The fusion cross section (and thus the rate of neutron generation) is strongly dependent on relative ion energy. In MST, T_i is typically $\leq 10^0$ keV, whereas neutral beam injection sources ions at $\sim 2 \times 10^1$ keV.

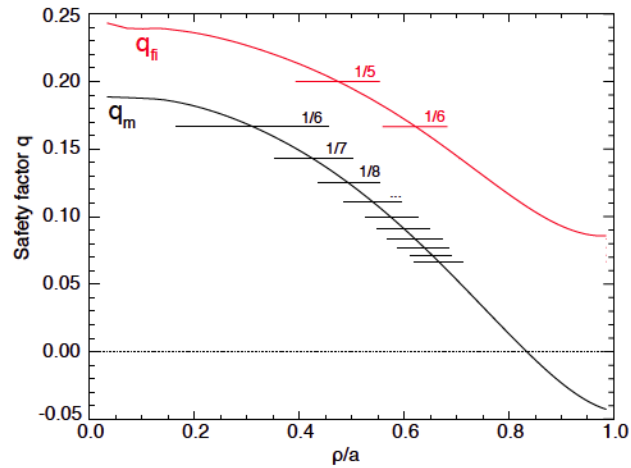


Figure 1.5: The fast ion guiding centers follow a different rotational transform (red) than the magnetic field lines (black). This leads to a spatial separation of the resonance locations.

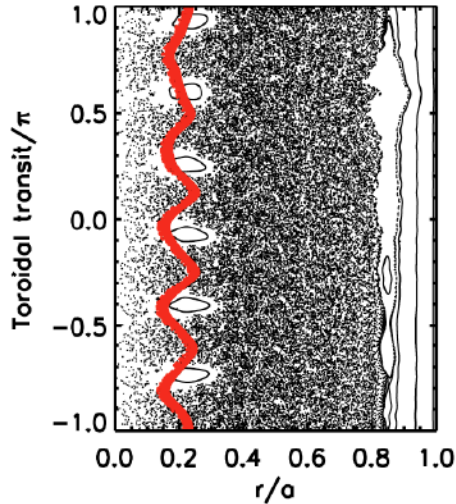


Figure 1.6: The black dots represent magnetic field lines puncturing through a stretched out radial-toroidal plane. An $n = 6$ island structure is observed near the core and a high degree of magnetic stochasticity dominates the mid-radius. The fast ion guiding center (red) follows an $n = 5$ orbit at the same location as the $n = 6$ magnetic surface.

population reduction due to the EPM-like modes, the confinement of fast ions is nearly classical, with $(\tau_{fi} \sim 20 - 30 \text{ ms}) \gg (\tau_p \sim 1 \text{ ms})$ in standard MST plasmas. The increased gyroradius and guiding center drift of the fast ions allow them to decouple from the magnetic field lines and develop a different rotational transform (i.e. $q_{fi} \neq q_{mag}$, Figure 1.5) [27, 31, 32]. This results in a spatial separation of the resonance of the guiding center motion and the peak of the magnetic perturbation (Figure 1.6). In a general sense, this allows the fast ions to “average over” or “smear out” the magnetic fluctuations that limit thermal particle confinement [31, 32].

The sawtooth cycle in MST

The plasma current in MST is driven inductively, using the plasma itself as the secondary winding of a transformer. Resistivity is lowest in the hot plasma core, resulting in a majority of the current being deposited there. This leads to an increasingly

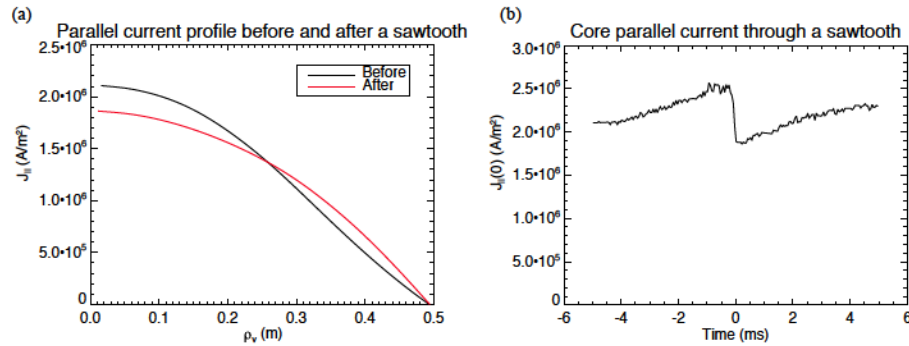


Figure 1.7: Equilibrium reconstructions show the relaxation of the peaked current profile in space (a) and time (b). Many similar sawtooth events are averaged together to reduce statistical noise, and time axis is adjusted so that $t = 0$ corresponds to the peak of the reconnection event.

peaked current profile that drives tearing instabilities. To redistribute the current and return to a lower energy state (Figure 1.7), the plasma undergoes a relaxation process in which core poloidal flux is converted to toroidal flux via magnetic reconnection. This process is facilitated by the growth of tearing modes at the numerous rational surfaces within the plasma (Figure 1.2).

The effect of this sudden relaxation is seen throughout the entire plasma. The amplitude of magnetic perturbations associated with the n and m numbers of the resonant tearing modes increase to values $\sim 5\%$ of the equilibrium magnetic field. Magnetic islands grow at the rational surfaces and eventually overlap, allowing rapid stochastic radial transport of thermal particles and a subsequent drop in the core plasma density and electron temperature. The changes in magnetic flux generate large, pulsed electric fields of the order 50-100 V/m (detailed further in Chapter 3). Many of the diagnostic signals undergo a sharp peak or drop, giving this process its colloquial name, “the sawtooth cycle.”

Magnetic reconnection

The topic of magnetic reconnection could fill an entire chapter if it were more integral to the proposed energization mechanism in this thesis. Reconnection does indeed occur during MST sawtooth crashes, but as will be described in more detail throughout the thesis, it is the global rearrangement of magnetic fields that is responsible for the acceleration of suprathermal ions rather than the local physics of the reconnection layer. However, particle acceleration during reconnection is a very active research topic; an excellent overview of reconnection physics can be found in review papers by Zweibel [16] and Yamada [17], and recent papers by Drake [33] and Egedal [34] propose new mechanisms for particle acceleration in the presence of reconnecting fields.

1.3 Previous results: anomalous ion heating during MST sawteeth

Among the many effects occurring at the sawtooth, the anomalous heating of ions is one of the most studied and least understood, and is a key part of the motivation for this thesis. During a reconnection event, the ion temperature can rise to several times its equilibrium value despite a decrease in the electron temperature. Initial observations of anomalous ion heating on MST were made by Earl Scime in 1992 using a diagnostic very similar to the one used in this thesis [35]. In this section, the results of previous ion heating studies on MST will be summarized.

Perhaps the most fundamental result is the identification of the equilibrium magnetic field as the ultimate energy source for the heating process. Figure 1.8 shows the energy stored in the magnetic field drops significantly at a reconnection event

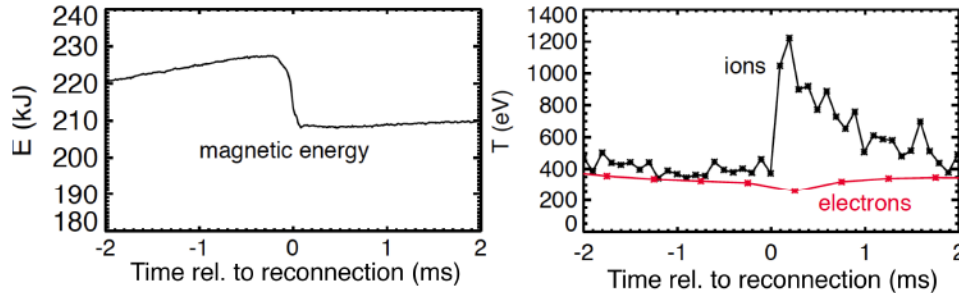


Figure 1.8: The energy stored in the equilibrium magnetic field (a) drops by $\sim 10\%$ at a sawtooth event. The C^{+6} impurity temperature (b) as well as the bulk ion temperature (not shown) rise rapidly, while the electrons lose a small amount of energy.

and is coincident with the ion heating [18]. There is a strong statistical correlation between the ion temperature gain and the magnetic energy loss across a large number of sawtooth events [36]. Furthermore, the efficiency of conversion of magnetic to thermal energy is observed to scale with the mass of the bulk ion species ($\Delta E_{ion}/\Delta E_{mag} \propto m_i^{0.52}$) [37].

The ion dynamics spectrometer (IDS) [38] and charge exchange recombination spectrometer (CHERS) [39] have been used to measure the temperatures of various impurity ion species in a number of experiments. Impurities are heated more than bulk ions [40], and further investigation reveals a charge-to-mass ratio dependence for impurity ion heating [41]. The CHERS diagnostic can measure the component of impurity temperature both parallel and perpendicular to the equilibrium magnetic field, and a heating anisotropy was found with $\Delta T_{\perp} > \Delta T_{\parallel}$ after the sawtooth [42]. The anisotropy becomes more pronounced at higher plasma density. There is also evidence that the heating is not toroidally symmetric: heating of C^{+4} ions was measured at several toroidal locations and the amount of heating is correlated with the toroidal position of the maximum radial magnetic perturbation [36].

In addition to the dependence on the energy stored in the equilibrium magnetic

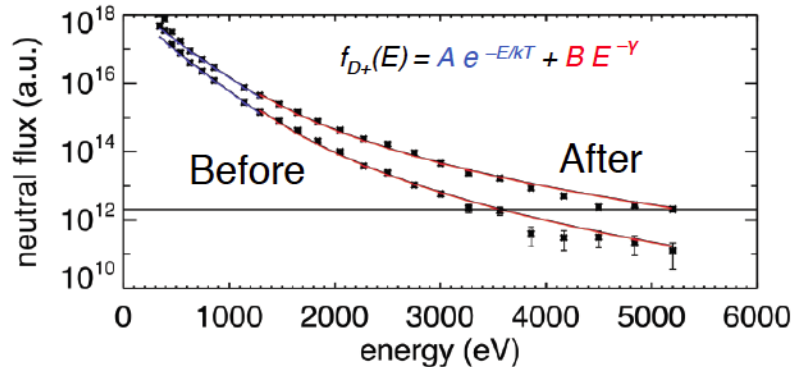


Figure 1.9: Measurements of the ion distribution before and after a sawtooth crash. The distribution is fit well by a Maxwellian plus a power law tail. The spectral index γ of the tail decreases at the crash, indicating an increase in the number of particles with energies higher than the thermal background.

field, ion heating has a unique dependence on the presence of the $m = 0$ edge-resonant tearing modes. During “typical” sawteeth, $m = 0$ and $m = 1$ modes nonlinearly couple and the amplitude of their magnetic fluctuations spike dramatically at the relaxation event; however, so-called “core events” can spontaneously occur in which only the core-resonant $m = 1$ modes are active and the edge-resonant $m = 0$ remains at relatively low amplitude. During these events, no ion heating is observed, and there is likewise no drop in the equilibrium magnetic field. In the inverse case (during “bursts” in which the $m = 0$ mode activity increases but the $m = 1$ activity does not), a small drop in the magnetic energy is observed, and impurity heating is measured only in the edge of the plasma [40]. Thus, the presence of the $m = 0$ mode is a necessary condition for ion heating, with the $m = 1$ modes greatly amplifying the effect through nonlinear coupling.

Finally, a Compact Neutral Particle Analyzer (CNPA), operated in collaboration with Florida A&M University, has been used to study the energy spectrum of the bulk ion population out to 5 keV [43,44]. Even away from sawtooth events, the bulk ion distribution is observed to have a non-Maxwellian tail. The spectral index of the

power law tail decreases at the sawtooth crash, indicating that ions are accelerated from the thermal population into the high energy tail. The spectral index is also lower in lower density plasmas, indicating a stronger energization mechanism at lower density or higher temperature. Although the diagnostic only measures up to 5 keV, modeling of the measured neutron flux during the sawtooth crash indicates that the tail should extend out to at least 20 keV [42].

Many mechanisms for anomalous ion heating in the RFP have been proposed, including:

- Stochastic heating of ions (or stochastic heating of electrons with wave coupling to ions) [37]
- Viscous damping of flows [45]
- Turbulent cascade driven cyclotron heating of impurities (with collisional coupling to bulk ions) [46]

A summary of the applicability of these models and how they match the observations listed in this section is in R.M. Magee's thesis [18]. As previously mentioned, no one theory is able to explain all of the observed phenomena.

In the next chapter, the Advanced Neutral Particle Analyzer will be described in detail. In Chapter 3, the electric field profile during sawteeth in MST is calculated from equilibrium reconstructions and the conditions necessary for ion runaway are outlined. In Chapter 4, ANPA measurements are presented and compared with the expectations from ion runaway. Chapter 5 discusses the connection between the inductive parallel electric field and the heating of thermal ions. Finally, Chapter 6 summarizes this work and identifies important questions for future work.

Chapter 2

Overview and development of the ANPA

2.1 Basics of neutral particle analysis

Neutral particle analyzers (NPAs) have been used to study plasmas since the early 1960s [47]. The objective of neutral particle analysis is to collect the products of ion-neutral charge exchange and analyze them to learn about the ions before the charge exchange event. The type of analysis performed varies from case to case and typically includes separation of particles by energy and/or mass. NPAs can be designed to study characteristics of the bulk ion population, but are more often used to measure fast ions from neutral beam injection or other heating mechanisms.

While there are many variations of NPA, the first step in most designs is reionization of the incoming neutral atom. This is generally accomplished by one of two means: a gas-filled stripping cell or a thin carbon foil [47]. Gas cells have better efficiency at lower energies (< 10 keV) but require additional gas supplies and vacuum pumping and can limit acceptance angles. The pressure in the stripping cell affects

the overall signal level and thus must also be measured and accounted for during analysis. Foils relax the vacuum and acceptance restrictions, but have poor efficiency and high scattering at low energies. Foils also slow down the incoming ions; this effect is small, but should be accounted for during calibration and analysis. After the incoming neutral atom is reionized, some combination of magnetic or electrostatic fields are applied to steer the ions into detectors (typically secondary electron multipliers (SEMs) or microchannel plates). Some designs use a single detector and vary the electric and magnetic fields so that the detector only samples the desired ions, while other designs incorporate an array of detectors with static fields to obtain simultaneous measurements of many types of particles.

Because the measured signal relies on ion-neutral charge exchange and therefore depends on the density profile of neutral atoms (which is often edge-peaked), measurements of core ions can become muddled. To avoid this, many experiments make use of a diagnostic neutral beam (DNB) to source additional neutrals in the core of the plasma. By taking the difference of data with the DNB turned off from data with it turned on, one can obtain a measurement that is localized to the intersection of the DNB and the NPA sightline. This is referred to as an “active” NPA measurement (as opposed to a “passive” measurement in which no additional source of neutrals is present).

2.2 Hardware design

The Advanced Neutral Particle Analyzer (ANPA) was designed and built in collaboration with the Budker Institute of Nuclear Physics (BINP) and installed on the Madison Symmetric Torus in 2011 [48]. A similar model was also installed on the C2 device at Tri-Alpha Energy.

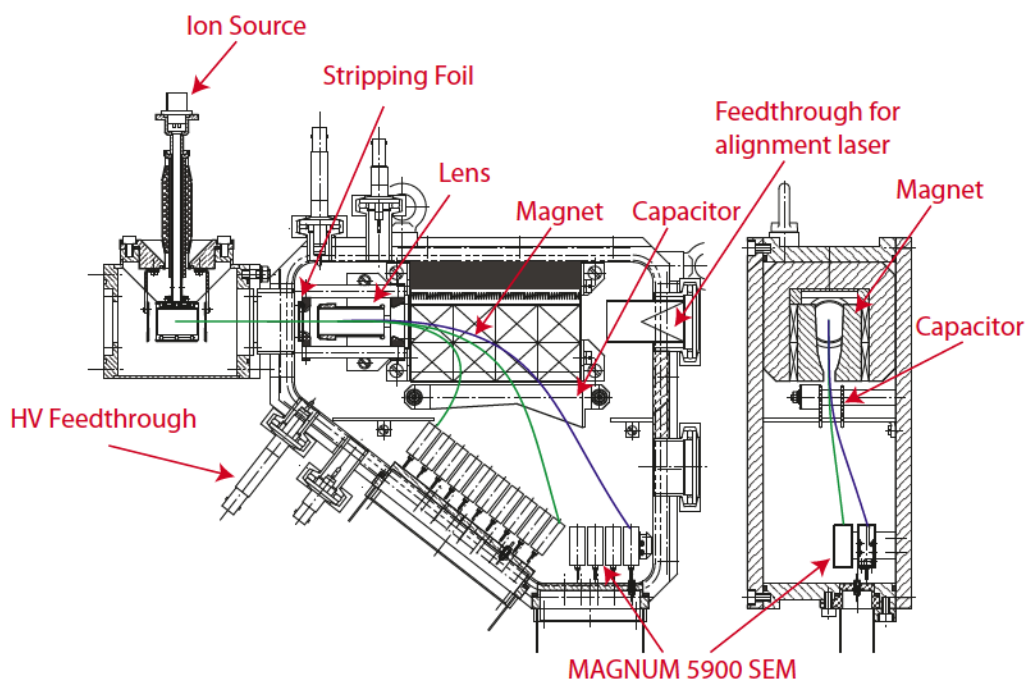


Figure 2.1: A diagram of MST's Advanced Neutral Particle Analyzer with primary components labeled. A top view (left) shows the energy separation of two hydrogen ions (green) and one deuterium ion (blue). The side view (right) shows the mass separation of the two species.

The ANPA is a tandem “E||B” design, meaning that both magnetic and electric fields are used for particle separation and the two fields are oriented parallel to each other but spatially separated. The ANPA was designed to study fast ions born from MST's 25 keV neutral beam injector (also acquired in collaboration with BINP). A diagram of the ANPA is shown in Figure 2.1. Incoming neutral particles pass through either a fixed aperture or an adjustable, vacuum-sealed aperture wheel (for run-day signal attenuation) and are then stripped by a 10nm thick carbon foil supported by a nickel mesh. The foil can optionally be biased at high voltage (up to 15 kV) to give the newly stripped ions additional energy, effectively shifting the energy range of the detectors downward. After being stripped and accelerated, the ions are focused by a 10-16kV electrostatic lens. Energy separation is performed by a 0.6 T magnet,



Figure 2.2: A photograph of the ANPA channeltron detectors. The top row is positioned to collect hydrogen ions while the bottom row is horizontally offset to collect deuterium of similar energies. Channel labels indicate progression from low to high energy.

bending ions into new trajectories based on their velocity. A 6-10 kV capacitor provides a vertical electric field that separates particles by mass; heavier particles travel slower at a given energy, meaning they spend a longer time in the electric field and are thus deflected more. Finally, the ions are collected by an array of Magnum 5900 Channeltron SEMs.

Two rows of 10 SEMs are arranged to detect hydrogen (top row) and deuterium (bottom row) ions with energies between 10-35 keV (for 0 V acceleration bias). The fronts of the detectors are negatively biased at 1.3-2.0 kV to repel free electrons and increase signal gain. Note that the difference in curvature radii between mass species means that hydrogen and deuterium detectors of the same energy must be horizontally offset as well as vertically (see Figure 2.2). One additional detector has been installed on the high-energy side of the detector bank above the hydrogen detector plane (the upper-left of Figure 2.2, though the detector is not shown). This detector is placed out of the way of any ion trajectories and is used to collect UV or other stray charged particle signals for noise analysis. More information on noise reduction can be found in Section 2.6.

The detectors output current through single-pin vacuum feedthroughs. The sig-

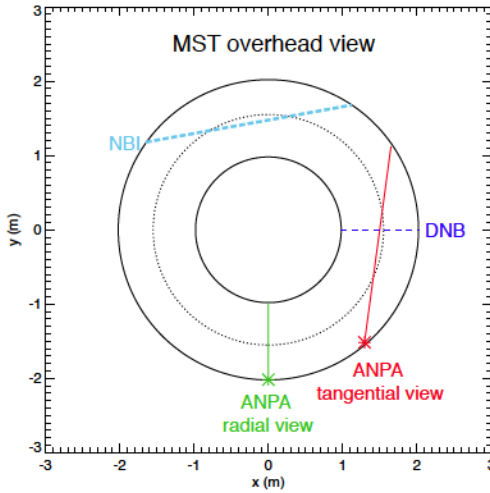


Figure 2.3: An overhead view of MST showing the locations of the NBI, DNB, and two ANPA views.

nals are amplified using in-house I-to-V amplifiers originally built for the SXR array. These amplifiers can be set via toggle switch to a gain of 10^5 , 10^6 , or 10^7 V/A. The 10^6 V/A gain is most often used for an output signal in the 0-5 V range.

One of the primary features of this model is its size. At 28 cm in its largest dimension, the ANPA is rather compact for the features it provides. This allows relatively easy movement and mounting on a variety of portholes on MST. To date, two different portholes have been utilized. The “radial view” at 270T, 15P looks straight through a poloidal cross-section of the plasma. The “tangential view” at 222T, -19P is substantially more complex in its physical rigging and viewing angle. A custom flange and mounting structure were constructed to accommodate this view, which looks tangentially at the intersection of the plasma core and the diagnostic neutral beam (Figure 2.4). If not for the ANPA’s compact size, this view would not have been feasible without even more substantial modifications to the surrounding diagnostics and support structures. The implications of these viewing angles will be discussed more in Section 2.4.

Alignment

Alignment for the radial viewport is relatively straightforward: a digital level is used to ensure the ANPA is at an angle of 15° , and a rigid flight tube connects the ANPA to the MST porthole. The alignment of the tangential view is significantly more complicated, however. A bellows is used between the ANPA and MST to accommodate the greater flexibility in positioning due to the tangential view mounting structure (Figure 2.4). Small angle deviations from “perfect” alignment can propagate into a large displacement from the intended measurement location further down the path. Rather than rely on external measurements of several different angles relating the ANPA to MST, a more direct method of alignment is used. A simple pen laser is mounted onto the spare vacuum feedthrough on the back of the ANPA (Figure 2.1) such that it shines directly through the ANPA’s stripping foil and down the flight tube, thus lighting the straight-line trajectory that a particle would need to follow. While MST is vented, the ANPA is adjusted until this laser aligns with a target probe marking the intersection of the DNB and the magnetic axis. A second, ANPA-specific target probe was constructed to mark a third point on the laser line at the far end of the machine; this probe is inserted at 300T, 15P. Because this port is behind a valve, the second target probe can be used for alignment while MST is under vacuum.

2.3 Calibration

Ion source design

A high-energy ion source for ANPA calibration was additionally designed and acquired from BINP. The original ion source was designed for *in-situ* calibration up to 25 keV. The source consists of a cylindrical metallic mesh on a high-voltage standoff,

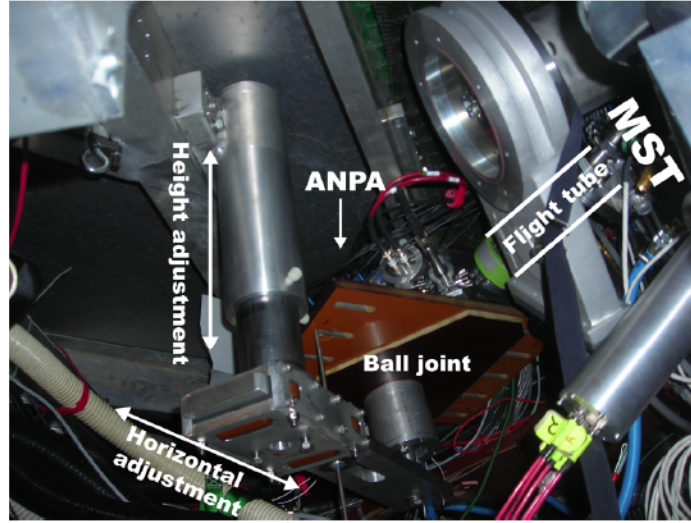


Figure 2.4: A photograph of the mounting structure for the ANPA's tangential view. There are four separate adjustments: a vertical sliding post to set the height of the mount, a horizontal slide to set the distance of the mount from the post, a swivel joint to set the angle at which the horizontal slide extends from the post, and a ball joint to provide 360° of freedom and allow connection of the ANPA to the MST flight tube.

two circular mesh endcaps, and a filament. The cylindrical mesh is brought up to the desired ion voltage, V_{cal} , while the endcaps remain grounded. The filament is set $\sim 200V$ below V_{cal} and a current on the order of 1A is run through it. The filament will thermally emit electrons which are accelerated toward the higher-potential grid. Here, hydrogen atoms will be ionized via electron impact ionization, and the newly formed ions will be accelerated from the high-voltage grid toward the grounded endcaps. Any remaining electrons will be absorbed by the grid and returned to ground through the power supply. A schematic and photograph of the source can be seen in Figures 2.5 and 2.6.

Initial tests of the ion source yielded very little ion current output. Similar issues were reported with the ANPA and source installed at Tri-Alpha Energy. After discussions with Budker and Tri-Alpha, it was discovered that a potential well could develop around the filament, preventing electrons from traveling to the grid. Model-

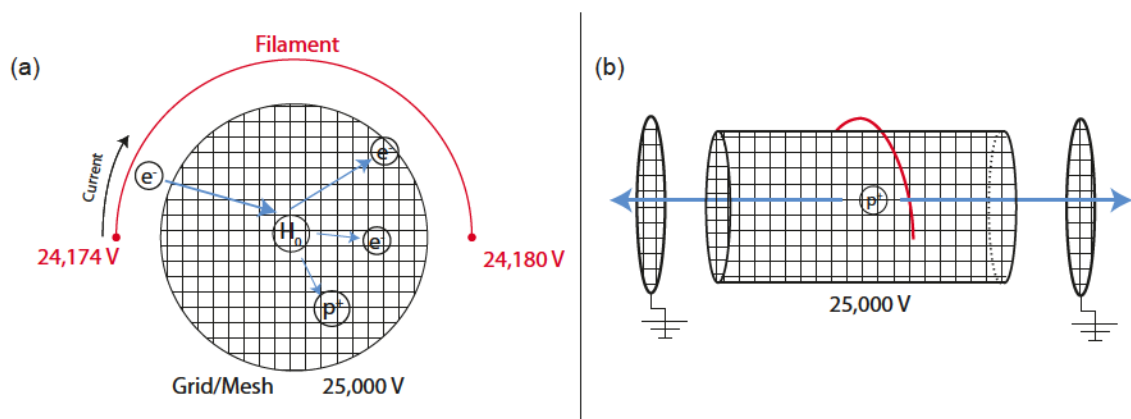


Figure 2.5: A schematic view of the calibration source from two angles: (a) looking down the flight tube, and (b) looking normal to the flight tube. In this figure, the voltages are set up to generate 25 keV ions.



Figure 2.6: A photograph of the cylindrical mesh and endcap. Connections for the filament can also be seen, though no filament is attached.

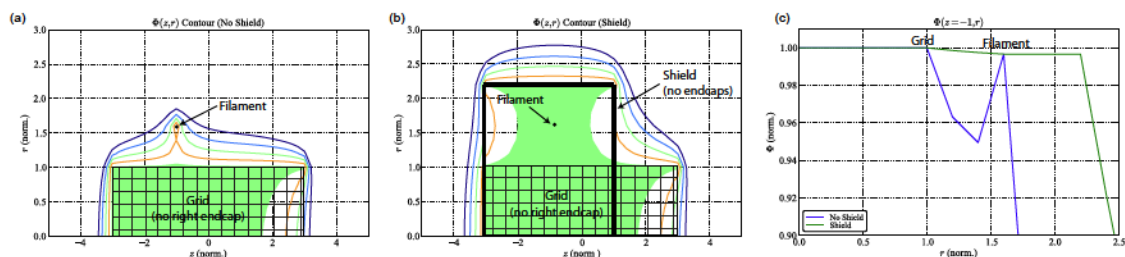


Figure 2.7: (a) Electric potential contours show a potential well around the filament. (b) A biased shield provides a potential path from the filament to the grid. (c) Electrons need an uphill potential path to the grid which is only present with the biased shield. Plots courtesy of Ryan Clary, Tri-Alpha Energy.

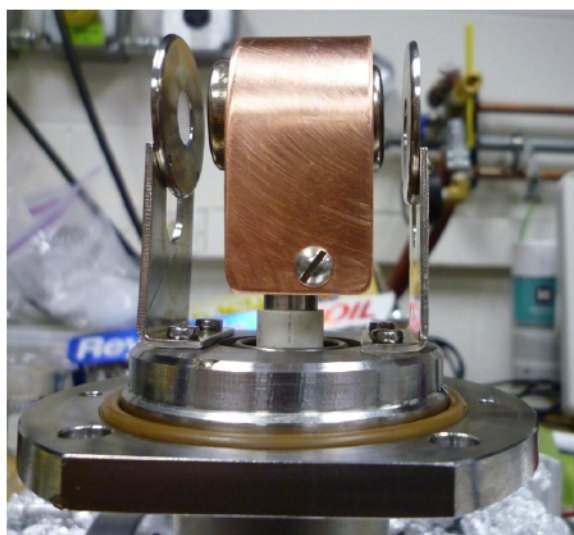


Figure 2.8: A photograph of the biased copper shield around the filament and grid.

ing by Ryan Clary at Tri-Alpha (Figure 2.7) confirmed this theory. By installing a conducting shield biased to the grid potential around the outside of the filament, the potential well is eliminated and the source functioned as intended.

Due to the issues with the unshielded filament and a desire to calibrate up to the maximum ANPA detection capability of 50 keV, a new ion source was built and installed by Budker. This new source utilizes the same basic principles, but incorporated the biased shield into the design, relocated the endcaps to make direct contact with the grid (using the vacuum chamber itself as the grounded target), and

accommodating high voltage standoffs up to 50 keV. Due to arcing hazards to nearby equipment as well as space concerns, there is no intention of using this new source *in-situ*.

Procedure

There are several goals of ANPA calibration. The first and foremost is determining the response of each channel to ions of various energy. We would also like to know the relative signal levels from channel to channel. Ideally, an absolute calibration would be obtained, translating a detector voltage into an absolute number of particles in the plasma. In practice, this is a very difficult task, and the challenges will be discussed in this section. Finally, we also wish to know the optimum settings for the various tunable ANPA parameters (the lens, accelerating potential, capacitor voltage, and detector bias) and how our signal changes as these parameters change.

Throughout the calibration procedure [49], several external quantities are measured in addition to the detector outputs. The voltage and current draw on the high-voltage power supply is monitored for any parameter that is being varied (accelerating grid, lens, capacitor, detector bias). The voltage of the ion source is monitored via the power supply output as well as a Ross high-voltage divider connected in parallel with the source. The pressure in the ion source chamber is monitored with a convectron gauge, as increased filament voltage will increase the chamber pressure and increased pressure will lead to more ion current. Finally, a Faraday cup is installed in the flight tube behind the ion source such that one side propels ions into the ANPA and, assuming symmetry of the ion source, the other side propels an equal number into the Faraday cup. The Faraday cup is typically biased to 18 V to eliminate false current from secondary electron emission by recapturing those electrons. The Faraday cup is thus used as a monitor of the output current of the ion source as

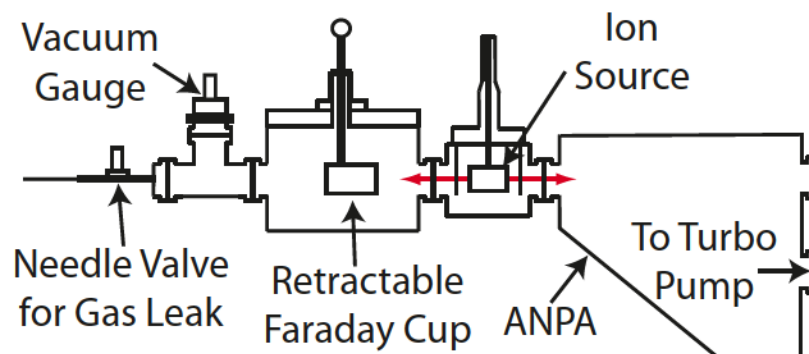


Figure 2.9: A diagram of the ANPA calibration setup showing the relative location of the ion source, ANPA, Faraday cup, and gas source.

pressure and voltage varies. A schematic of the setup can be seen in Figure 2.9.

All calibrations were performed on a workbench rather than *in-situ*. A USB multiplexing digitizer was used in conjunction with Labview to collect the data from the detectors. High voltage measurements were recorded on an oscilloscope, triggered from the Labview routine. The HV power supplies were controlled using a Galil RIO-47100 pocket PLC and the GalilTools software.

During calibration of the hydrogen channels, the residual chamber gas was used as the ion source gas. The H_2O and H_2 molecules in the residual air will lead to two species detectable by the ANPA at normal operating settings: H^+ and H_2^+ (which has the same charge-to-mass and thus same trajectory as D^+). Additionally, the Faraday cup will pick up H_2O^+ , OH^- , and any other heavy ion species. The uncertainty in the ion species mix being detected by the Faraday cup is the first challenge in obtaining an absolute calibration from this method. However, if one assumes that the species mix stays consistent throughout the calibration procedure (an assumption that may or may not be true), the Faraday cup can still be used as a relative normalization factor for the varying source output current.

While the deuterium channels could in theory be calibrated using the H_2^+ from the residual chamber gas, signal levels are often far too low to use this method.

Instead, additional gas is pumped into the chamber. Ultimately, a bottle of deuterated methane (CD_4) was purchased from Cambridge Isotope and used as the working gas for deuterium calibrations. While using pure D_2 might be a natural choice, it is more likely to produce D_2^+ (which will not hit the ANPA detectors) rather than D^+ . Evaporated heavy water (D_2O) was also considered, but the deuterated methane provided good results, so heavy water was never attempted.

Results

Energy and relative gain calibrations

For a fixed capacitor, lens, grid, and detector bias voltage, the ion source voltage can be varied to determine the response of each detector to ions of varying energy. The ion source is slowly brought to the maximum desired voltage (ideally 50kV, although due to arcing across the HV standoffs or within the HV circuitry, lower values were often used). Once there, the voltage is ramped down in a controlled fashion and the signal on each detector is recorded. This process can be repeated multiple times, and the results can then be averaged together after normalizing for changes in Faraday cup current and pressure. A sample energy calibration is shown in Figure 2.10.

Looking more closely at a single channel (Figure 2.11), three distinct signal peaks are observed during the energy scan. The largest peak near the nominal channel energy (~ 10 keV for this case) is the expected response from H^+ ions generated at the ion source. The peak to the right occurs at twice the nominal energy and is the result of 20 keV H_2^+ ions breaking apart at the ANPA stripping foil and splitting into two 10 keV H^+ ions, thus being detected at the 10 keV detector. The small peak to the left occurs when the ANPA accelerating grid is set to a finite value. Here, the grid was set to approximately 5 kV. Most of the sourced ions will lose 5 keV as they

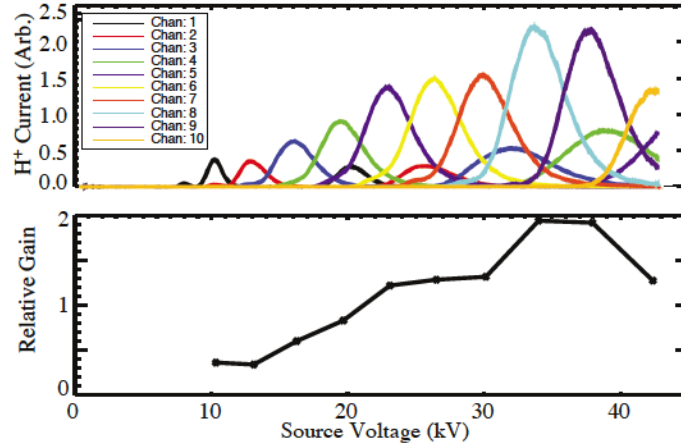


Figure 2.10: (a) Signal level on each detector throughout an ion source voltage scan. (b) The relative gain of each channel, accounting for changes in the Faraday cup current.

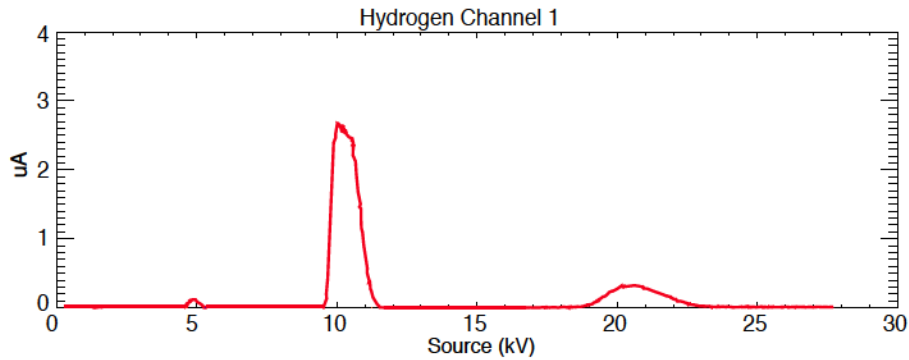


Figure 2.11: Three peaks are observed on each energy channel corresponding to H_0 , H^+ , and H_2^+ particles hitting the ANPA stripping foil.

approach the grid and then gain 5 keV after they pass through for zero net energy change. However, a small number of the ions will reneutralize in the flight tube and therefore not be slowed down as they approach the grid, but will be stripped and still gain 5 keV after passing through the foil. These ions show up in the calibration at a source voltage equal to $V_{nominal} - V_{grid}$.

The identity of these three peaks can be confirmed by adjusting the accelerating grid voltage. As the grid voltage is increased, the central H^+ peak will remain sta-

tionary as the ions continue to gain as much energy as they lose. The left-most H_0 peak will shift further left according to $V_{nominal} - V_{grid}$. The right-most H_2^+ peak will shift right by $1/2 V_{grid}$ since the lighter H^+ ions pick up twice the speed that the heavier H_2^+ lost.

Just as deuterated methane is used to obtain a higher population of D^+ ions (compared to D_2^+), regular methane can also be used to minimize the H_2^+ peak. However, the erroneous peak is easily filtered out of the calibration in post-processing, so methane was not typically used for hydrogen calibrations.

Once the calibration data has been obtained, a Gaussian is fit to the primary H^+ peak for each channel. The central energy of the Gaussian is used to define the nominal central energy of the channel, the width is used to characterize the width of the energy bin, and the height (normalized with the Faraday cup current or neutral pressure) is used to obtain a relative gain calibration between each channel. Note that this calibration is only valid for the specific capacitor, lens, and detector bias settings that were used.

Capacitor calibration

The ANPA “capacitor” creates the vertical electric field that controls the downward deflection of the ions toward the detectors and is thus responsible for mass separation. The goal of the capacitor calibration is to determine the optimum voltage setting to guide the primary beam of ions into the desired detectors and maximize signal. To determine this, the ion source voltage was fixed at the central energy of one of the ANPA channels and the capacitor was scanned from 0 to -15 kV. This was repeated for each channel energy to look at the gain of each channel as a function of capacitor voltage. The results are plotted in Figure 2.12.

The range of interest is approximately -5 to -11V. Hydrogen signals between -2 and

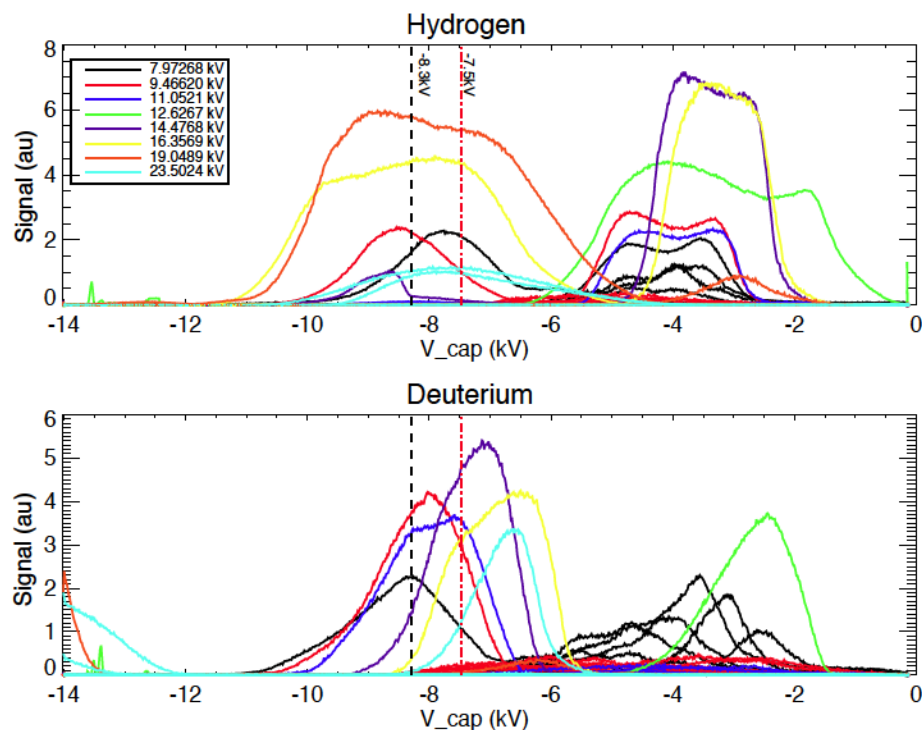


Figure 2.12: Results of the capacitor calibration. Optimal settings were determined to be -8.3 kV (black line) for hydrogen detection and -7.5 kV (red line) for deuterium.

-5 V result from deuterium (or H_2^+) ions being guided into the hydrogen detectors. In the deuterium channels, signals in the same energy range likely originate from D_2^+ ions. The beginning of signals related to hydrogen ions being steered into the deuterium channels can also be seen around -14 kV. Unfortunately, there is not a single capacitor setting that optimizes the gain in all channels at once. Two default “compromise” settings (-8.3 kV for hydrogen channels and -7.5 kV for deuterium channels) were established that maximize the gain on the channels of interest without sacrificing too much signal on the rest of the channels.

Additionally, ion source voltage scans were performed at several fixed capacitor values, and the Gaussian centers and widths were obtained for each channel to see if there was any change. The results (Figure 2.13) indicate that the central energies remain constant from -9 to -6 V (after which signals begin to drop rapidly and good

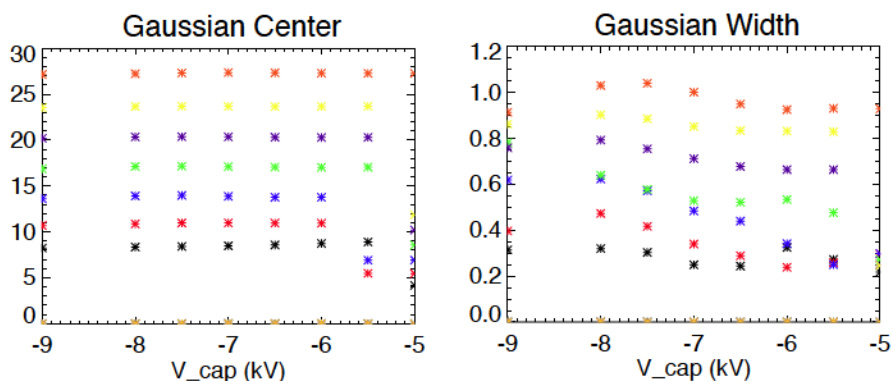


Figure 2.13: The central energy of each channel remains constant for reasonable capacitor values. The width does vary and should be accounted for. Each color represents a different energy channel. The results shown are for hydrogen channels only, and only 8 channels are shown due to unreliable performance of the ion source near its maximum voltage..

fits can no longer be obtained). The channel widths do show some variation which should be accounted for if the capacitor is used at nonstandard values.

Lens Calibration

The purpose of the electrostatic lens is to focus the incoming ion beam and eliminate any non-axial (in relation to the flight tube) velocity components. One would therefore expect the channel widths to be at a minimum and signal levels to be at a maximum for the optimal lens setting.

Similar to the second capacitor calibration experiment, an ion source voltage scan was performed at several discrete lens voltages and the Gaussians for each channel were characterized. Figure 2.14 shows the trends in Gaussian height, center, and width as the lens voltage is varied. As expected, there is little to no shift in the central energies, widths decrease as the lens voltage is increased, and signal levels increase up to a lens voltage of 12 kV, after which they drop off. There is another slight increase at 15 kV, but this is near the HV standoff maximum, so the safer value

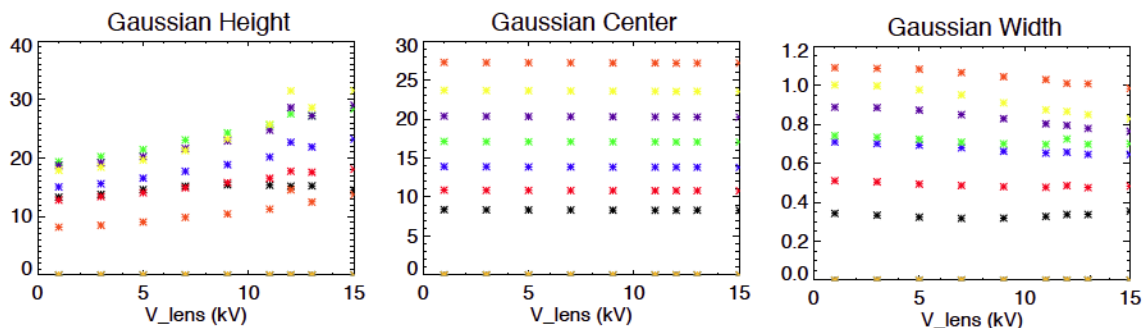


Figure 2.14: Increasing the lens voltage increases the signal gain (Gaussian height) and lowers the channel width. There is little-to-no effect on the central energy.

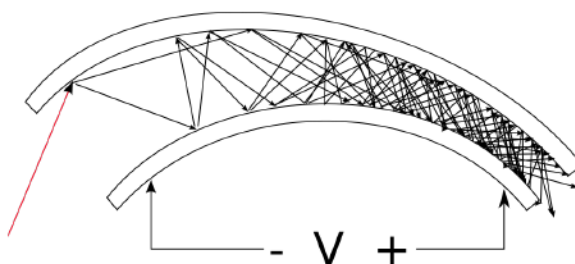


Figure 2.15: The curved interior of a Channeltron allows high-gain multiplication of secondary electron emission.

of 12 kV is used.

Detector bias calibration

In addition to deflecting free electrons near the detectors, the primary function of the detector bias is to amplify the gain of the Channeltron SEMs. When an incoming particle hits a Channeltron, it knocks off one or several electrons. These electrons see a large negative bias at the front of the detector and thus accelerate into the detector. Due to the curved interior of the Channeltron (Figure 2.15), they quickly collide with the detector wall, knocking off more electrons which then get accelerated, and so on. The amount of negative potential at the front of the detector affects the speed at which the electrons collide with the wall and thus the number of additional electrons

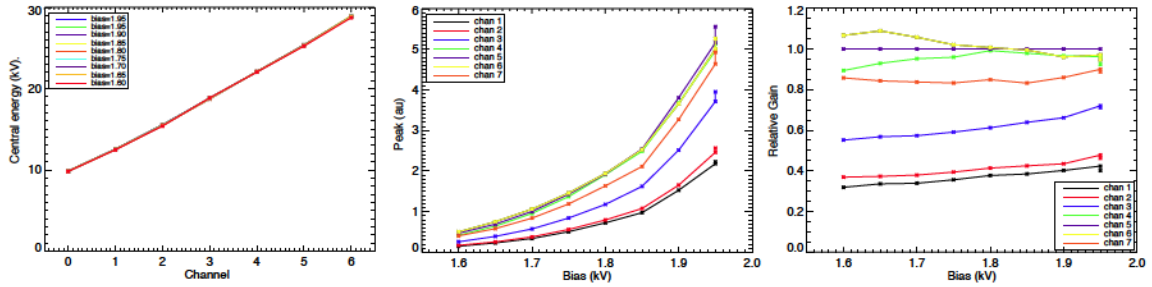


Figure 2.16: Increasing the bias voltage increases the signal gain exponentially (b) and alters the relative calibration (c). All of the lines in (a) overlap, indicating no effect on the central energy.

that will be knocked off and eventually form an output current.

The recommended operating voltage for the Magnum 5900 Channeltrons is between 1.4 to 2.2 kV which correspond to gains ranging from 10^5 to 10^7 [50]. As with the previous calibration procedures, the ion source voltage was scanned at a variety of bias settings. The channel energies remain constant throughout the scan (Figure 2.16(a)) and the heights increase exponentially as the bias is increased (b). The relative gain (normalized to channel 5) varies differently for each individual channel. This could be due to slight differences in manufacturing or the angle at which particles strike the Channeltron surface.

Unfortunately, the calibration ion source puts out a signal much weaker than the flux measured during an MST pulse with NBI. The minimum bias voltage that produced usable calibration signals was 1.6 kV, which is typically the maximum voltage used during experiments with the ANPA's default aperture. In the past, 1.3 kV was used as the default detector bias setting to avoid Channeltron saturation during NBI. Relative gain coefficients were obtained for this setting by extrapolating a linear fit to the data in Figure 2.16(c). This is far from ideal, as one can see that there is quite a bit of nonlinearity in the calibration data. To alleviate the need for this extrapolation, a smaller aperture has been used in recent runs so that the

Channeltrons can be run at 1.6 kV without saturation.

Accelerating grid calibration

The effects of the accelerating grid were briefly described earlier in this chapter. Namely, the voltage on the grid should have little to no effect on the final signal. Rather, it should simply shift ions up in energy by V_{grid} so that each channel's central energy is shifted down by V_{grid} . The channel widths are determined by geometric effects and should not be affected by the grid voltage, unless the grid caused additional scattering. This should in theory be negated by the lens.

One effect that should be mentioned when discussing the effect of the grid on the calibration is that the carbon foil, even when no voltage is applied, slows down any atoms or ions that pass through it. The amount of slowing is of the order $4.4 \times 10^{-3} d \sqrt{E}$ (keV), where d is the thickness of the foil in Å and E is the ion energy in keV [51]. For our 10 nm foil, a 25 keV ion would slow down by approximately 2.2 keV. However, because the foil is in place during calibration, any slowing is already incorporated in the measured central energies of the channels.

2.4 Modeling of signal contributions on different viewports

The ANPA measures the products of a fast ion population n_{fi} exchanging charge with a background neutral population n_0 . However, only a fraction of the neutrals generated make it to the ANPA. Ions must have the correct pitch at the location of charge exchange such that the resulting neutral's straight path leads into the ANPA collection region. This critical pitch, γ_c , varies with the magnetic field structure and the orientation of the ANPA with respect to MST. Unlike in a tokamak, the poloidal

and toroidal fields in the RFP are of comparable amplitude, with the toroidal field crossing zero and reversing near the plasma edge. Consequentially, ions near the edge with high pitch $\gamma \equiv v_{\parallel}/|v|$ are actually traveling in the poloidal direction and would not be detected by a toroidally-viewing NPA. Signal is further reduced by the chance of reionization before the neutral reaches the ANPA. The fraction that reionize, f_r , is calculated from the sums of ion impact ionization, electron impact ionization, and ion-neutral charge exchange. Taking these effects into account, the measured neutral flux is

$$\Gamma_{meas} = \int_L n_0 n_{fi} \langle \sigma v \rangle_{cx} \delta(\gamma - \gamma_c) (1 - f_r) dl \quad (2.1)$$

$$f_r(l) = e^{-\int_l^0 (n_i \langle \sigma v \rangle_{impact} + n_e \langle \sigma v \rangle_{impact} + n_i \langle \sigma v \rangle_{cx}) dl} / |v_{fi}| \quad (2.2)$$

where all quantities vary with distance along the ANPA line of sight l , and the pitch γ is defined as

$$\gamma \equiv \frac{v_{\parallel}}{|v|} = \frac{\vec{v}_{fi} \cdot \vec{B}}{|\vec{B}|} \quad (2.3)$$

TRANSP modeling of the fast ion distribution generated by NBI produces estimates of the pitch distribution and density of fast ions [25, 52]. The critical pitch γ_c and reionizing fraction f_r can be determined from equilibrium reconstructions, and the neutral density n_0 is calculated from modeling of the measured D_{α} line emission using the NENE Monte Carlo code (discussed further in Appendix 1). Due to the finite solid angle of the ANPA, the delta function in Eq. 2.1 will actually have a finite width around the critical pitch γ_c . The ANPA's solid angle has not yet been precisely characterized, but due to multiple apertures in the flight tube, it is believed to be well-collimated. For this model, ions with minor pitch deviations ($|\gamma - \gamma_c| \leq 0.04$)

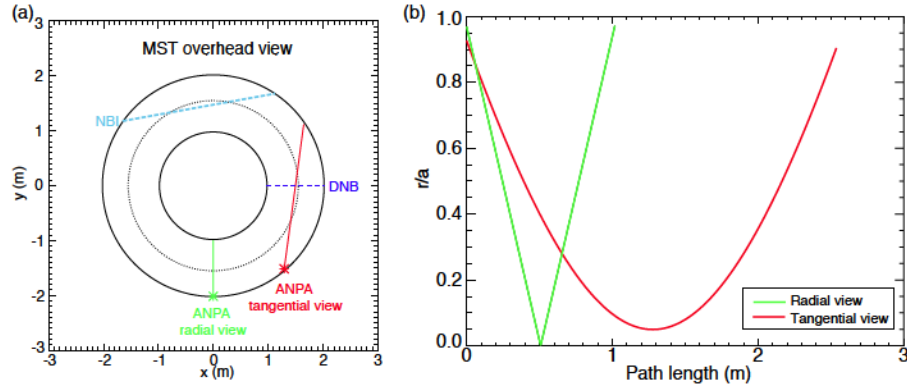


Figure 2.17: The radial view has a much shorter path length that follows a straight trajectory through the plasma core. The tangential view has a substantially longer path length and spends a larger portion of its trajectory in the plasma mid-radius and core.

are considered. By combining these calculations, analysis of the signal contribution along the ANPA's line of sight can be performed.

We first consider the simpler sightline from the ANPA's radial ("perpendicular") viewport. Figure 2.17 shows the trajectory of the sightline through MST, and Figure 2.18 shows the results of modeling Equation 2.1 for a 300 kA, $F=-0.2$, $\bar{n}_e=0.5e13$ cm^{-3} standard MST discharge. Panel (a) shows the edge-peaked neutral density (estimated by NENE) and the core-peaked fast ion density (estimated by TRANSP) as a function of the path length along the ANPA sightline. Panel (b) shows that the required fast ion pitch to make it into the detector is 0 along the entire path length - this makes sense because the ANPA is viewing radially and $B_r = 0$. In red, the fraction of ions with $\gamma \approx 0$ is seen to be highest in the edge of the plasma, particularly the outboard edge (closer to the ANPA). In green, the fraction of CX neutrals that will be lost to reionization is plotted - those born closest to the ANPA have the greatest chance to make it into the detector. Panel (c) shows the results of combining panels (a) and (b): in black, the total number of generated charge exchange neutrals is plotted ($n_0 n_{fi} \langle \sigma v \rangle$), and in red, the number detected after accounting for pitch

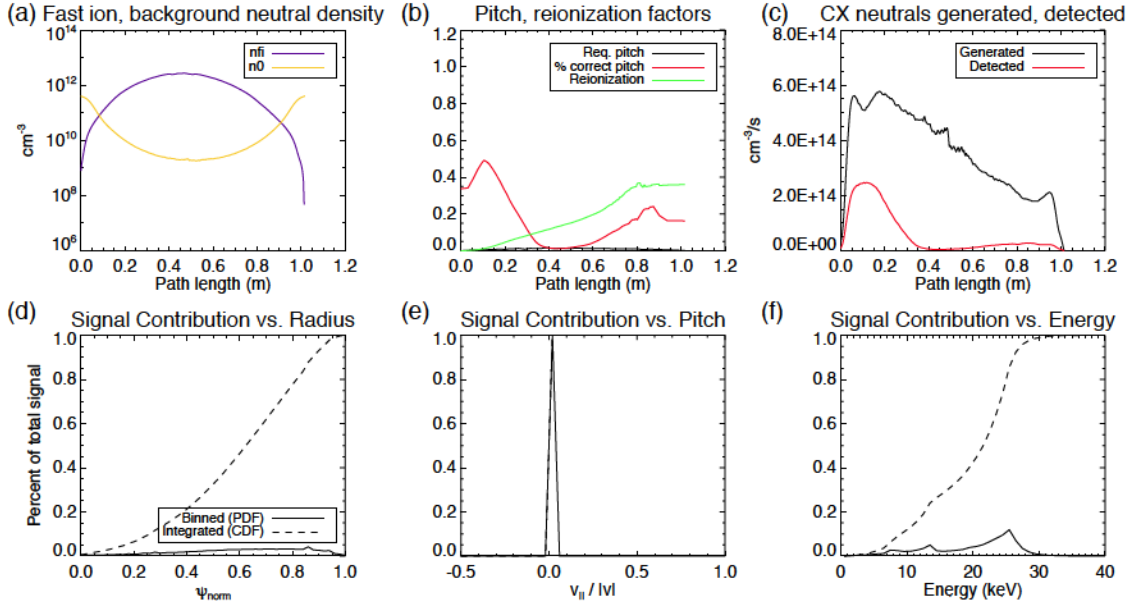


Figure 2.18: ANPA signal modeling for the radial view. Panels (a)-(c) show properties of the neutral and fast ion populations along the ANPA line of sight. Panels (d)-(f) show how much of the total measured signal originates from ions of varying location, pitch, and energy.

and reionization is plotted. We see that on this view, most of our signal comes from the outboard side of the machine, closest to the ANPA.

In panels (d) - (f) we look at the total measured signal as a function of radius, pitch, and energy. In (d) we see that the measured signal is fairly evenly distributed throughout the mid-radius and edge of the plasma, $\psi_{norm} \sim 0.4-0.9$. As one might expect from the required pitch plotted in (b), (e) shows the all of our signal comes from the lowest pitch bin. Finally, in (f) we see that about 25% of our signal comes from the beam's half-energy component and a significant portion comes from ions that have already slowed down below the 25 keV injection energy. From these results, we conclude that the radial view is a very poor representation of the majority of the beam-injected ions which are estimated to be very core-localized and high pitch. However, it can tell us a fair amount about the half-energy component and about

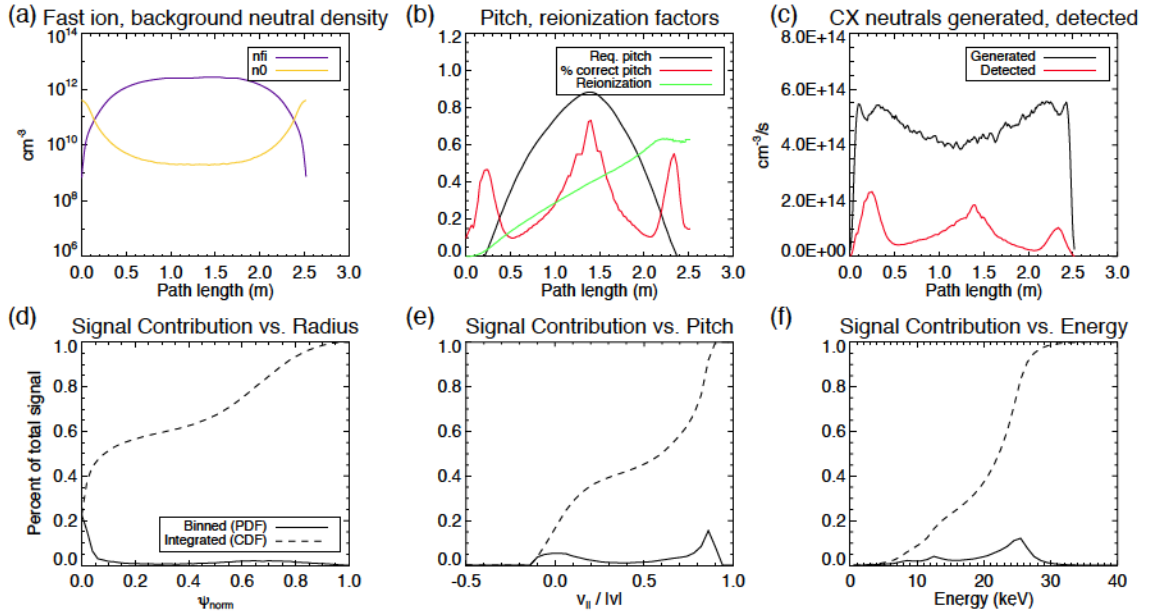


Figure 2.19: ANPA signal modeling for the tangential view. Panels (a)-(c) show properties of the neutral and fast ion populations along the ANPA line of sight. Panels (d)-(f) show how much of the total measured signal originates from ions of varying location, pitch, and energy.

low-pitch fast ions that have begun to slow down and wander radially outward.

The tangential or “parallel” view tells a very different story. In Figure 2.17 and 2.19(a) we see that this view has a much larger portion of its path length in the high- n_{fi} , low- n_0 core of the plasma. The pitch required for detection varies substantially along the path, with a negative pitch required at the plasma edge and a high pitch (~ 0.85) in the core. The fast ion pitch is most in line with the required pitch in the edge and core, dropping off in the mid-radius. As before, the chance for reionization grows with distance from the ANPA. Since the path length is much longer than the radial view, the attenuation is as large as 60% at the far edge of the machine. In (c), the generated neutral flux is fairly flat along the sightline as the increase in n_{fi} is balanced by the decrease in n_0 . However, the pitch selection restricts the measured signal to the edge and core regions.

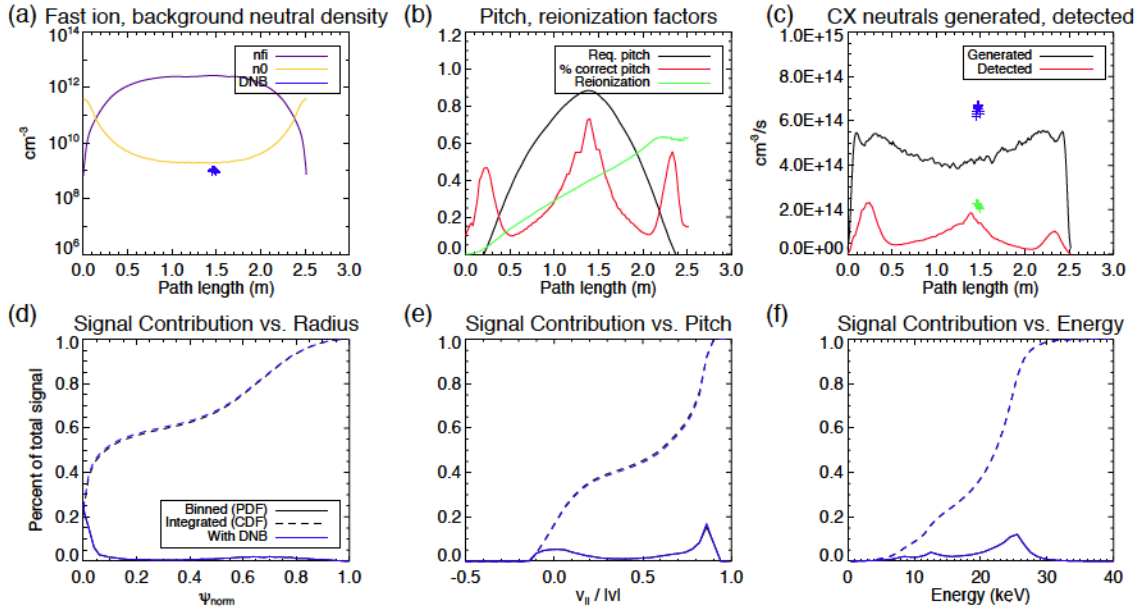


Figure 2.20: ANPA signal modeling for the tangential view with DNB in standard plasmas.

Looking at the overall signal contribution, roughly 55% of the measured signal originates from core-localized, high-pitch, maximum-energy ions, roughly 40% comes from edge-localized, low-pitch ions, and the remaining 15% is spread across the mid-radius at a variety of pitch angles.

One of the original intents of the tangential view was use of the DNB for an active neutral source in the core. Figure 2.20 shows the modeled results of the additional DNB neutral population in a standard $F=-0.2$ plasma. Here, a very basic model of the DNB is used with $I=4$ A, $E=42$ keV, and a non-diverging Gaussian beam width of 3.5 cm. While the DNB does increase the neutral density and number of CX products by a factor of ~ 2 (blue symbols in (a) and (c)), the amount of the total path length spent intersecting with the enhanced neutral density is low. In panels (d)-(f), the signal contributions with and without the DNB are nearly indistinguishable.

In PPCD discharges (described in more detail later in this chapter), the back-

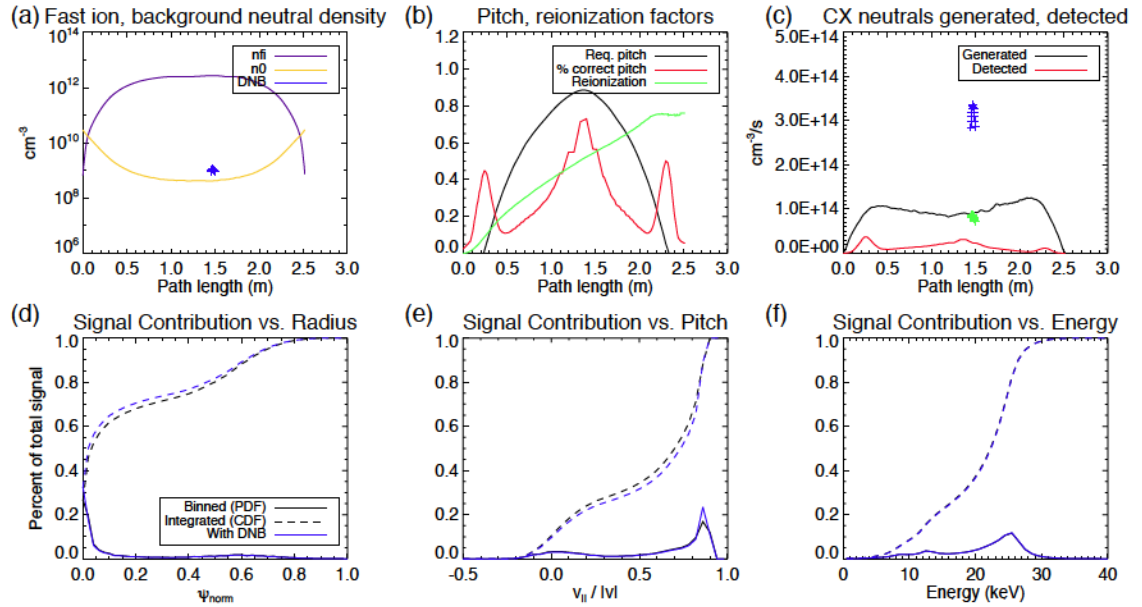


Figure 2.21: ANPA signal modeling for the tangential view with DNB in standard plasmas.

ground neutral density is substantially lower, so the addition of the DNB neutrals should have an even larger effect. Figure 2.21 shows the modeling results. We now see a factor of $\sim 4\text{-}5$ increase in the neutral density and CX products, and a small but noticeable shift in the number of core-localized, high-pitch ions (from roughly $\sim 65\%$ without DNB to $\sim 70\%$ with).

Despite the difference observed in modeling, no measurable differences have been seen in experiments with and without the DNB in PPCD. There are a number of possible explanations. First, alignment of the ANPA is difficult. The ANPA is aligned by pointing a pen laser through the center of the ANPA input aperture and aligning that laser point to the DNB alignment probe. In theory, this should guarantee good alignment, but in practice, small errors in the alignment of the laser to the ANPA body or the insertion depth of the alignment probe could result in only a partial intersection between the ANPA sightline and the edge of the DNB. Second, NENE estimates of

the neutral density in PPCD are believed to be inaccurate. Although most alternative estimates indicate the true core neutral density is lower than the NENE estimate (thus leading to a larger expected effect from the DNB), the inaccuracy in the edge profile is unknown and could muddle the signal. Additionally, the TRANSP distributions in PPCD could be highly inaccurate due to TRANSPs inability to model portions of the plasma with $q < 0$, which is nearly half the plasma in PPCD. Finally, it may be possible to see a difference using multi-shot averaging and subtraction of data from non-DNB shots, but the repeatability of plasmas with good PPCD, NBI, and DNB is low, and substantial run time has not been dedicated to this pursuit.

Since most of the data in this thesis is from standard, reversed plasmas, no attempt is made to utilize the DNB for an active view. However, the assumption that the passive tangential view provides a good measure of the core-localized, high-pitch NBI population has been justified in other experimental results.

First, during a helical distortion of the plasma core known as QSH or SHAx (described in more detail in the next section), the measured ANPA signal drops to less than half its pre-SHAx value. This drop in signal is attributed to a loss in confinement of the core-localized, high-pitch fast ions in the presence of the helical perturbation [27]. However, the helical distortion only affects the core of the plasma; the outer flux surfaces remain axisymmetric. Thus, the edge-localized, low-pitch ions are not affected, accounting for the small amount of signal measured during the SHAx state.

Second, the NBI drives a number of energetic-particle-driven modes (EPMs) that cause non-classical fast ion transport [26, 28]. A reduction in ANPA signal is correlated with bursts of EPM activity, and the spatial location of these modes is identified using the FIR interferometer. A fast ion loss rate can be defined as the negative time derivative of the normalized ANPA signal, $\nu = -\frac{1}{I_{ANPA}} \frac{\partial I_{ANPA}}{\partial t}$. When only a sin-

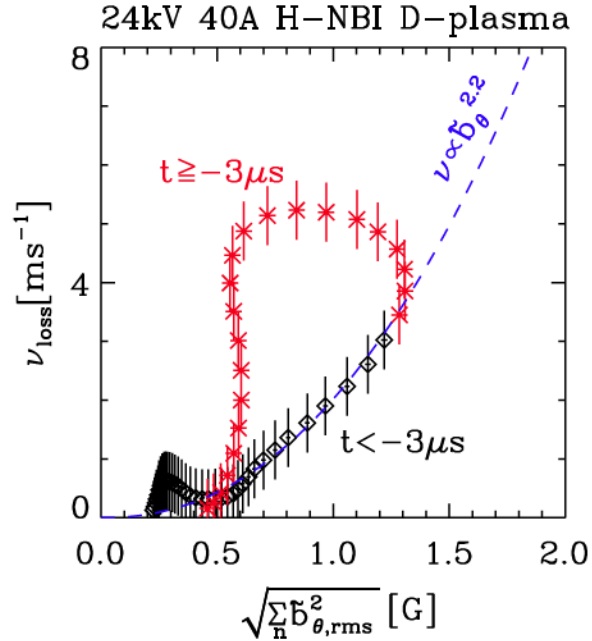


Figure 2.22: Before multiple EPMS nonlinearly interact (black points), the fast ion loss rate determined from the slope of the ANPA channel closest to the primary beam energy scales with $\tilde{b}_{n=5}^{2.2}$, suggesting strong interaction between the core-localized $n=5$ mode and the fast ions. After the growth and nonlinear interaction of other EPMS (red points), the loss rate is higher.

gle mode ($n=5$) is active, the loss rate scales with $\tilde{b}_{n=5}^{2.2}$ (Figure 2.22). After the other EPMS become unstable and interact nonlinearly, the loss rate is even greater; however, the strong correlation between the ANPA signal and the single-mode fluctuations supports the notion that the measured fast ions originate in the core (where the $n=5$ mode is resonant).

A third experiment lends support to the modeled edge localization of the radial ANPA view. In low current, non-reversed ($F=0$) plasmas, ANPA signal corresponding to the primary energy beam ions is dramatically reduced when the current is lowered below approximately 220 kA. The gyroradius scales as $|B|^{-1}$, so as the plasma current gets lower (and therefore the poloidal field magnetic field near the edge of the plasma gets lower), the gyroradius will increase. In fields this low, the gyroradius can be

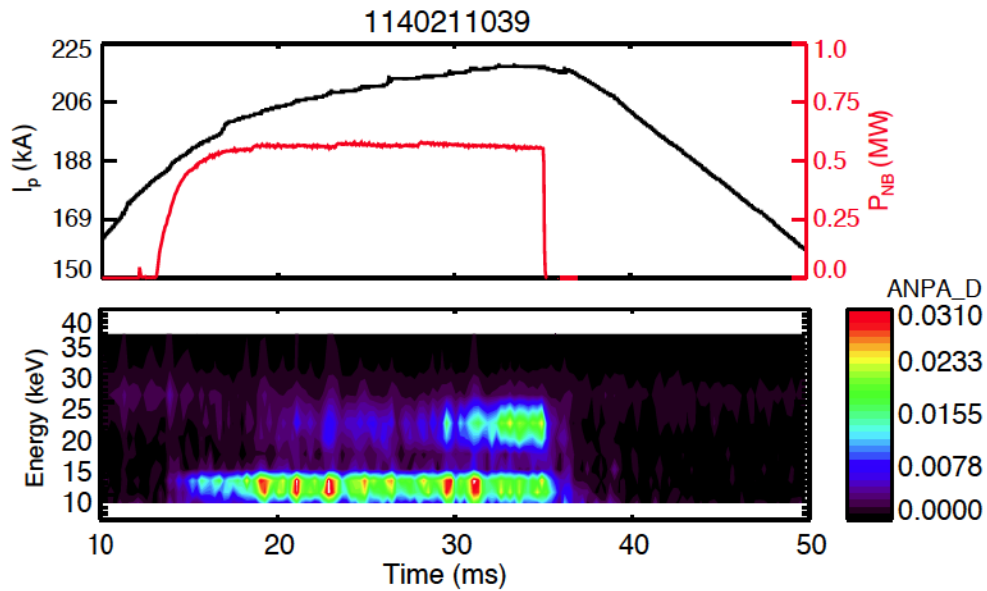


Figure 2.23: As the plasma current increases slowly throughout the discharge, the full-energy beam component becomes more prominent. It is theorized that particle orbits in the edge are transitioning from a scrape-off orbit to a confined orbit as their gyroradius decreases.

as big as 20 cm or more. At some point, the gyroradius will become so large that orbits will transition from confined to lost. The particles comprising the half-energy component of the beam have a smaller gyroradius and are therefore not lost. A careful study has not yet been performed, but Figure 2.23 shows an example in which the plasma current rises throughout the plasma “flat-top” and the ANPA-measured beam signal grows stronger throughout that rise. Although this does not directly support the claim that the tangential view measures core ions, it supports the modeling procedure by validating that the radial view indeed measures ions from the edge.

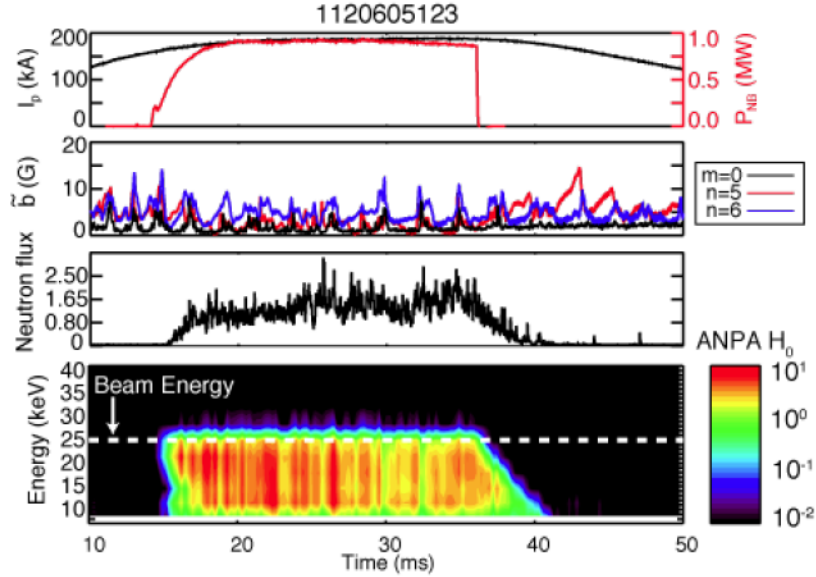


Figure 2.24: Sample ANPA data from an F=0 discharge.

2.5 Initial survey data and analysis techniques

In this section, sample ANPA data is presented in a variety of plasma conditions. Unless otherwise noted, this data is from the tangential viewport and minimally processed, with only the relative calibration applied; that is, the quantity plotted is still the full convolution of effects discussed in the previous section, $\Gamma_{meas} = \int_L n_0 n_{fi} \langle \sigma v \rangle_{cx} \delta(\gamma - \gamma_c) (1 - f_r) dl$. Throughout this section, additional analysis techniques will be introduced to better illustrate the n_{fi} contribution of the signal.

F=0 plasmas

Non-reversed or “F=0” plasmas are formed by pinning the safety factor at the wall $q(a)$ to zero. Because the $m=0$ surface is removed from the plasma, these discharges do not experience large sawtooth crashes and therefore provide a good target discharge for studying basic diagnostic behavior.

In Figure 2.24, tangential ANPA data from a sample 200 kA F=0 discharge with

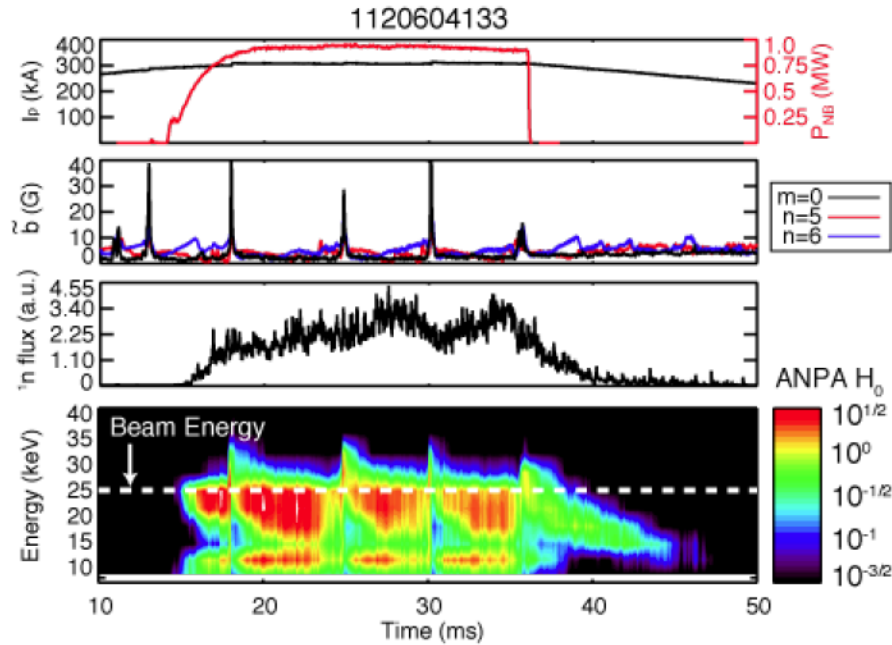


Figure 2.25: Sample ANPA data from an $F=-0.2$ discharge.

NBI is shown. As NBI turns on at 12 ms, ANPA signal is observed in the channels corresponding to the injected beam energy. The signal quickly spreads to channels below the beam energy as a slowing-down distribution is formed in the plasma. Additionally, signal from the half-energy component of the beam is observed in the appropriate channel, although in this case the slowing of the primary beam energy is dramatic enough to overlap with it. After the beam turns off, the slowing of the remaining ion population is observed. The 95% H 5% D beam fuel drives beam-target fusion and produces a measurable neutron flux that tracks well with the ANPA signal.

“Standard” ($F=-0.2$) plasmas

In reversed (or so-called “standard” RFP) discharges, sawtooth relaxation events play a major role in the dynamics of the plasma. In Figure 2.25, tangential ANPA data is plotted for NBI into a standard discharge with $F=-0.2$. The classical slowing time

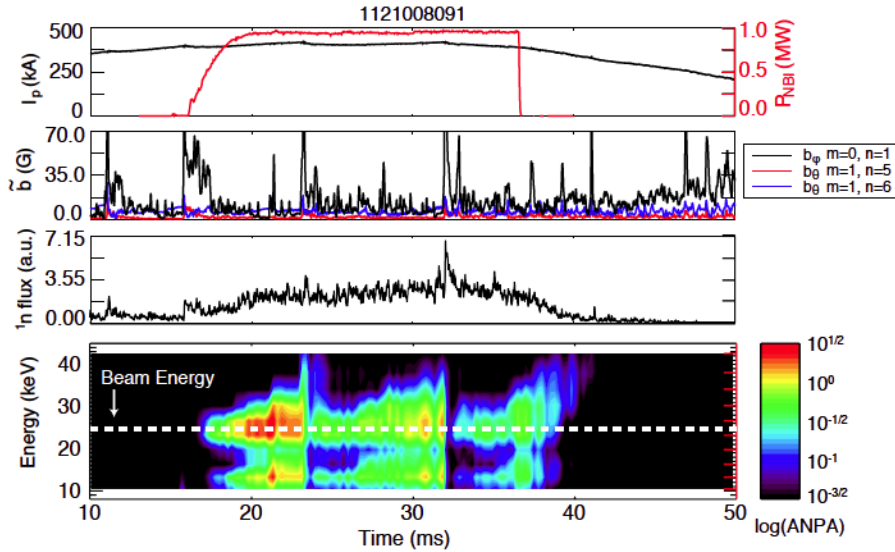


Figure 2.26: Sample ANPA data from an $F=-0.3$ “EC” discharge.

for fast ions is much longer in this 400 kA plasma compared to the cool 200 kA $F=0$ plasma from Figure 2.24, allowing a much clearer delineation between the full- and half-energy beam components. In addition to the features observed in the 200 kA $F=0$ discharge, ion acceleration is observed at the sawtooth crash. The details of this acceleration will be discussed in detail in Chapter 4.

Enhanced confinement (“EC”) plasmas

“EC” or “enhanced confinement” discharges occur at low density ($n_e \leq 0.5$) and deep reversal ($F \leq -0.3$). These conditions can spontaneously lead to relatively long quiescent periods between sawteeth, punctuated by small bursts (~ 10 G) of $m=0$ activity. The resulting sawtooth crash after an EC period is generally much stronger than typical sawteeth in “standard” plasmas.

In Figure 2.26, tangential ANPA data is plotted during an EC discharge. Fluctuations in signal amplitude and some energization is observed during the $m=0$ bursts during the EC period, and a large amount of energization occurs at the violent saw-

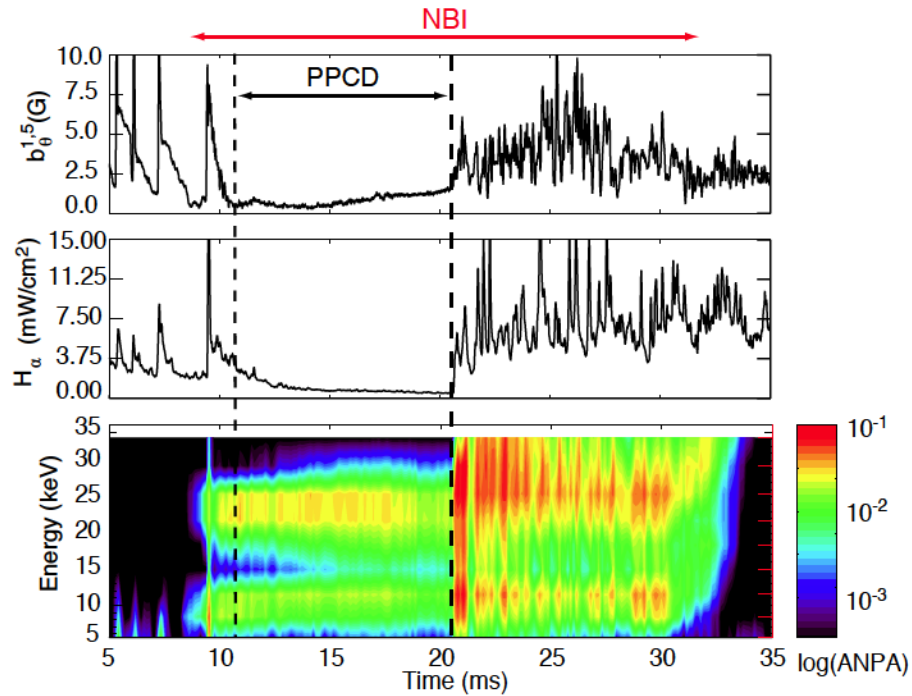


Figure 2.27: Sample ANPA data from a PPCD discharge.

tooth crashes before and after the quiescent period. The energization due to the $m=0$ bursts has not yet been closely studied or characterized.

PPCD

Pulsed poloidal current drive [53] is a technique for suppressing magnetic fluctuations by driving current in the plasma edge, leading to improved plasma confinement and performance. Fast ion confinement is also enhanced during PPCD [25] which, in theory, makes PPCD a good target condition for fast ions studies and ANPA measurements.

Figure 2.27 shows tangential ANPA data into a sample PPCD discharge. A steady signal is observed during the PPCD period, followed by what appears to be a large increase in the fast ion density and energy. However, it is important to remember

that the ANPA signal is not a direct measure of the fast ion population, but rather of the charge exchange products of fast ions and background neutrals (Equation 2.1). Because of the enhanced confinement, plasma-wall interactions are reduced leading to a much lower background neutral density during the PPCD period (D_α emission is plotted in Figure 2.27 as a proxy for the neutral density). As the PPCD period comes to an end, the large outflux of hot particles results in significant wall interaction leading to a quick increase in the neutral density up to an order of magnitude higher than during the PPCD period. These discharges are the most striking example of the need to correct for background neutral density in ANPA analysis.

Deconvolving contributions from changes in neutral density

This change in neutral density becomes problematic when trying to use ANPA data as a measure of the fast ion population. With perfect knowledge of the fast ion profile and the neutral density profile, one could simply deconvolve the neutral effects from Equation 2.1 and obtain the underlying n_{fi} distribution. Attempts have been made to reconstruct the neutral density profile using an array of D_α detectors and the NENE Monte Carlo code [54, 55]. These efforts are covered in detail in Appendix A. While improvements have been made compared to previous measurements, the accuracy of these reconstructions is often called into question, particularly for PPCD discharges.

Additionally, TRANSP modeling of the fast ion density is troublesome in PPCD due to the deep reversal. Because TRANSP uses the toroidal flux as a radial coordinate, modeling can only be performed out to the reversal surface before that parameter becomes non-monotonic. Thus, TRANSP modeling in PPCD forces the user to ignore a large portion of the plasma volume.

Because of these difficulties, a rigorous accounting of the neutral density is not currently feasible. However, some simple adjustments can be made to make an approxi-

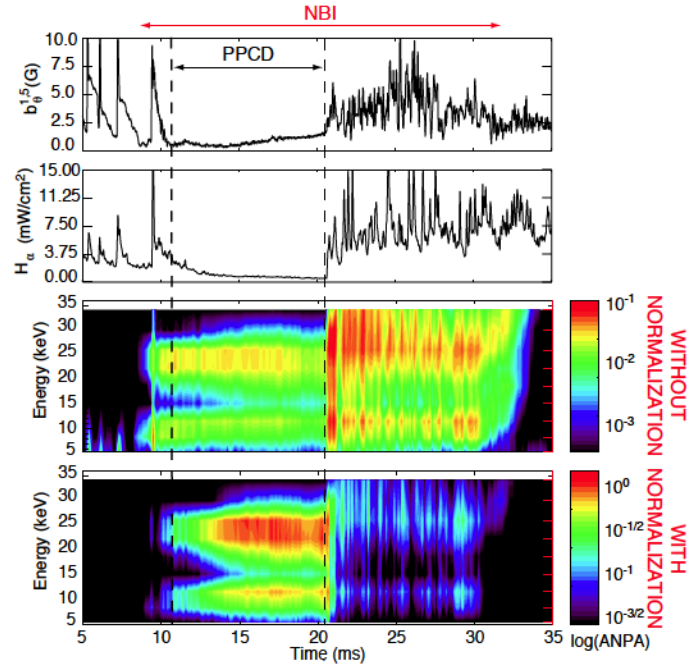


Figure 2.28: Sample PPCD data with D_α normalization.

mate correction. The line-integrated D_α emission is proportional to the background neutral density according to

$$\Gamma_{D\alpha} = \int_L n_0 n_e \langle \sigma v \rangle_{excitation} dl \quad (2.4)$$

Although the D_α emission detectors are not colinear with the ANPA sightline, an approximate cancellation of the effect of background neutral density can be made by dividing the ANPA signals by the D_α emission and multiplying by the line-averaged electron density (cross sections, pitch effects, and other constants have been omitted for clarity):

$$\begin{aligned}
\Gamma_{ANPA}^{corrected} &= \Gamma_{ANPA} \cdot \frac{n_e}{D_\alpha} \\
&\simeq n_0 n_{fi} \cdot \frac{n_e}{n_0 n_e} \\
&\simeq n_{fi}
\end{aligned}
\tag{2.5}$$

After making this correction, the character of the ANPA during the transition after PPCD is greatly altered (Figure 2.28). Instead of an apparent increase in signal level and ion energy, we now see a much more believable reduction in signal as the fast ion population experiences a sudden degradation in confinement.

QSH/SHAx

At high plasma current and low density, the core-most tearing mode (for MST, the $n=5$) can grow to very high amplitudes and cause a spontaneous transition from the typical axisymmetric RFP equilibria to one with a helical core [56]. This state is commonly referred to as the Single Helical Axis (SHAx) or Quasi-Single Helicity (QSH) state, depending on how much larger the dominant tearing mode is compared to the secondary modes.

Two observations about the interaction of fast ions with the QSH mode can be made from examining the ANPA data in Figure 2.29. First, as the $n=5$ mode ramps up to high amplitude, a slight acceleration of the fast ion population above the beam injection energy is observed. Second, as the secondary modes ($n=6,7,$ etc.) decrease and the SHAx state establishes, the ANPA signal decreases significantly. After the SHAx state relaxes back into a multiple-helicity state, the ANPA signal returns to previous levels. Although it was first suspected that the fast ions were simply undergoing a spatial or pitch redistribution and no longer being measured by the ANPA, recent studies using a beam blip technique and analysis of the neutron flux have shown

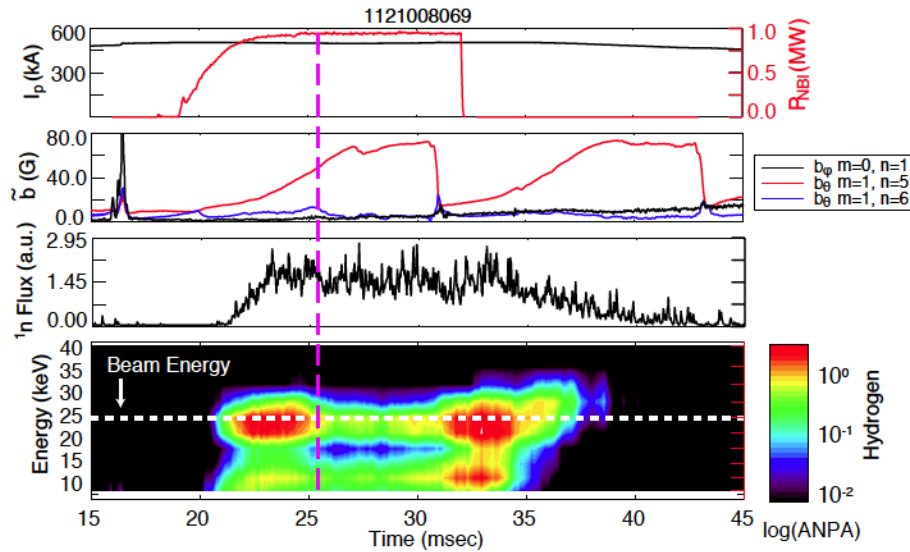


Figure 2.29: Sample ANPA data from a QSH discharge. The purple vertical line denotes the time when the $n=6$ and other secondary modes decrease and the SHAX state is established.

that, although fast ions are well-confined in the standard multiple-helicity RFP, their confinement time decreases significantly in the single-helicity regime [27].

Bulk plasma measurements

Although the ANPA is typically used to study NBI-sourced fast ions, large reconnection events can generate a substantial fast ion tail in the bulk plasma [42]. The upper end of this fast tail is within the energy range of the ANPA, and some attempts have been made to measure it. For exceptionally strong reconnection events (such as those following a quiescent period in EC plasmas), a measurable signal is present in the lower ANPA channels (Figure 5.5). Some attempts have been made to characterize the upper end of the tail, but analysis is complicated by several factors.

First, the background neutral density changes dramatically at a sawtooth crash, and without the consistent NBI fast ion population, it is difficult to tell how much

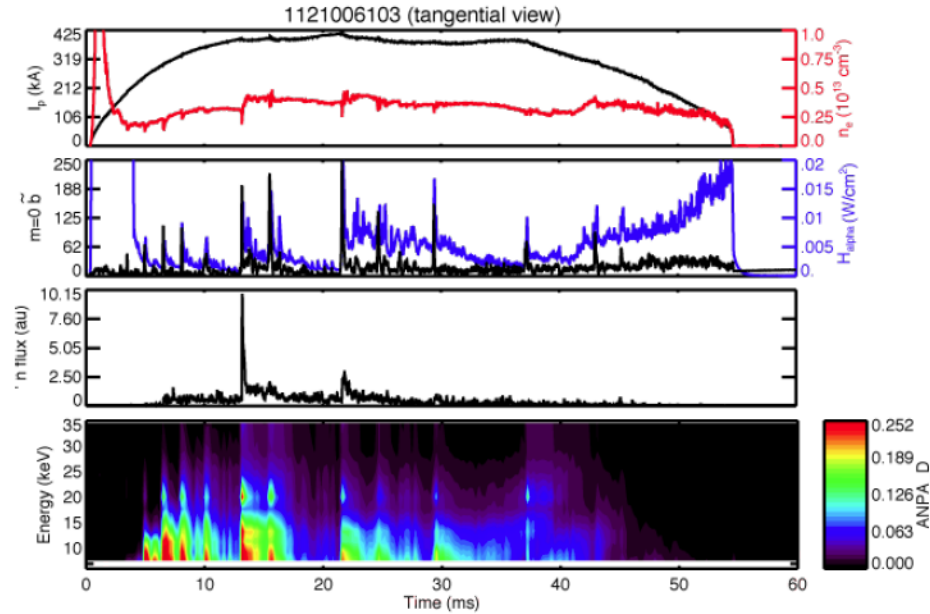


Figure 2.30: Sample ANPA data from an EC discharge with no NBI. Signal corresponding to the fast tail of the bulk deuterium population is observed at sawteeth, coincident with sharp increases in neutron flux. This data is not normalized to changes in H_{α} , so some of the signal increase can be attributed to neutral density changes. The gap in signal around 18 kV is due to poor calibration of the deuterium channels at the time this data was taken.

signal comes from newly-generated fast ions and how much comes from an increase in background neutral density. One can use the D_{α} normalization procedure outlined earlier in this chapter, but the profile effects that are not accounted for in that method are likely important.

Second, the signal levels for these events are much smaller than the levels obtained during NBI, and thus UV and other noise becomes an issue, particularly at the sawtooth crash. On the radial view especially, large signals corresponding to UV noise are observed on all ANPA channels and do not exhibit the typical slowing time behavior of a real particle signal. Techniques for noise reduction and subtraction are discussed in the next section, but have not been refined enough to make conclusive statements about the real fast ion signal. This is an area that would benefit from

further development in the future.

2.6 Noise analysis and subtraction

Several methods have been developed to monitor noise on the ANPA signals from ultraviolet light, stray charged particles, and electromagnetic pickup. First, a coaxial cable has been run from the digitizer crates to the ANPA along the same path as the real signal cables. This allows monitoring of any electromagnetic pickup by the cables themselves. Additionally, plasma shots can be taken with the gate valve between the ANPA and MST closed, blocking all particles and light from entering the ANPA chamber. Both of these methods indicate negligible levels of electromagnetic noise.

Noise from charged particles and UV light are harder to measure and diagnose. A large permanent magnet can be placed along the ANPA flight tube such that it bends the trajectories of any stray charged particles into the grounded flight tube wall. Thorough analysis and testing with and without the magnet has not been performed, but cursory attempts at using the magnet to reduce noise when present did not seem to have any effect.

Two primary methods are used to characterize the UV noise picked up by detectors. First, the steering capacitor can be turned off such that no real charged particle signal is incident on the detectors. UV should be unaffected, and thus whatever signal is present is the UV contribution to the real signals. While this method should work in theory, there are additional complications in practice. Although not bent into the detectors, the charged particle flux does still enter the ANPA and will impact the chamber wall, possibly creating secondary electron emission or light emission that may be picked up by the detectors. Indeed, some of the detectors measure higher signals with the steering capacitor off than with it on (Figure 2.31). By attempting to

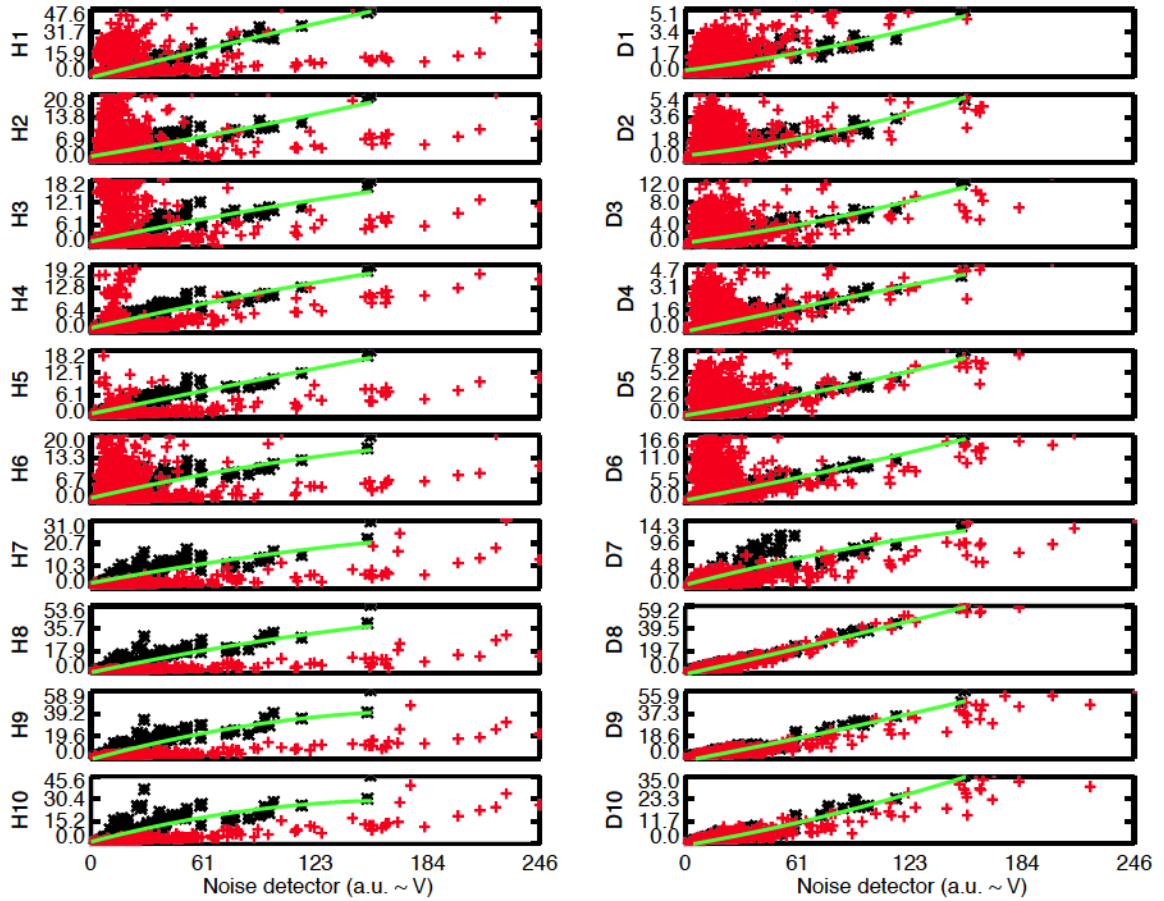


Figure 2.31: Scatterplots show the relationship between each ANPA channel and the noise detector. Black points correspond to signal at a particular time snapshot for a number of "noise shots" in which the steering capacitor is set to 0. Higher signal on the noise detector (x-axis) corresponds to higher signals on each individual detector (y-axis). The highest signals are seen during sawteeth. In green, a second-degree polynomial is fit to the black points - this is the value that will get subtracted from real data depending on the noise detector signal at each time point. In red, data from a particular shot with NBI is shown, with the steering capacitor set to its normal value. The bulk of the NBI signal lies above the noise in the first several channels. However, for the higher-energy channels, more signal is observed in the noise shot than the real shot, suggesting that an additional noise source is present when the capacitor is set to zero.

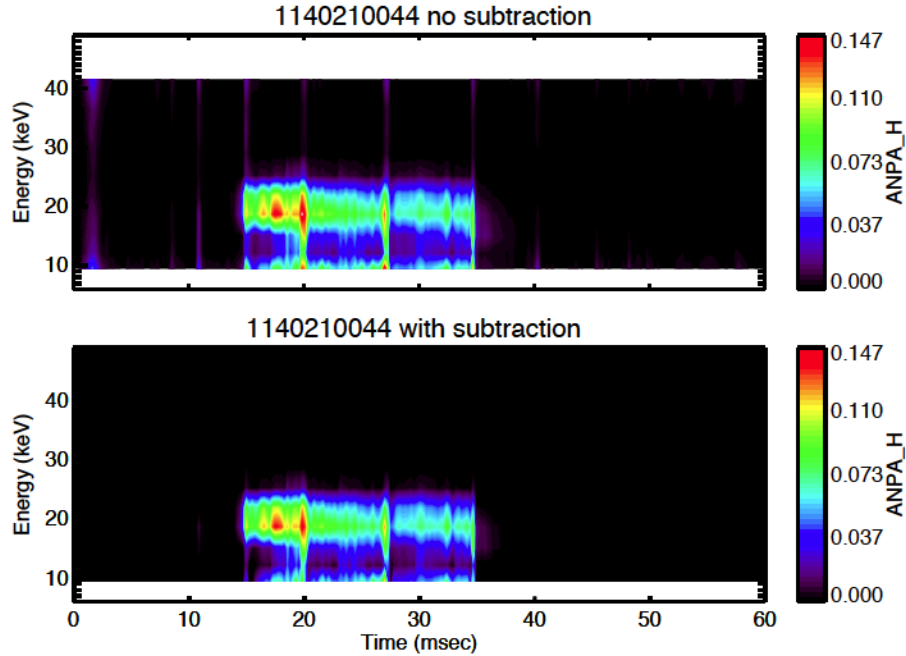


Figure 2.32: Radial ANPA data in an $F=-0.2$ discharge. Noise is seen in purple at the beginning of the shot, and in the high-energy channels at each sawtooth crash. A cleaner signal is obtained after subtracting signal proportional to each channel’s correlation with the noise detector (seen in Figure 2.31).

isolate the UV noise, an additional noise source is created that is not present during normal operation.

Because of the complications in the previous technique, a second and more reliable method of UV noise measurement was implemented. A UV-transparent window was installed in the ANPA aperture wheel that allows UV to pass through while blocking charged particles. This allows for a measure of the UV as it will be picked up during real measurements, without an additional noise source being generated.

Using the additional SEM that was installed outside of the charged particle path, a relationship can be calculated between the signal on the “noise detector” and each other detector during discharges with the UV window in place. Then, during normal operation without the window, the signal on the noise detector can be scaled and

subtracted from each signal (Figure 2.32).

UV noise can also be mitigated to some degree by designing light traps and minimizing the number of reflective surfaces inside the ANPA chamber, but this would require substantial modification to the interior of the ANPA and has not been deemed necessary thus far.

2.7 Summary

This chapter covers the development of a powerful new diagnostic for measuring fast ions on MST. Numerous hardware controls are investigated, calibrated, and optimized. Modeling of radial and tangential sightlines is performed to identify the key contributions to the measured signal, accounting for background neutral particle density, geometric effects, and reionization. Noise sources are characterized and subtraction techniques have been developed and utilized when signal-to-noise levels are insufficient. All of these preparations are crucial for the accurate interpretation of ion acceleration measurements in upcoming chapters.

Chapter 3

Modeling of the sawtooth-induced electric field

3.1 Ion runaway physics

In 1958, Harry Dreicer presented work on the effects of a static electric field on electrons in a plasma [57]. If the electric field is greater than the drag due to collisions, the electrons accelerate. The drag for a test electron on other electrons and ions decreases as $mvv \sim 1/v^2$, meaning that the motion of slower electrons will be dominated by drag while faster electrons have low enough drag that they can be accelerated by the electric field. As these electrons are accelerated, the drag on them continues to drop, and they “run away” to speeds much higher than the thermal distribution. The critical electric field at which the electron thermal velocity is sufficient to runaway is known as the Dreicer field and is defined as:

$$E_D = \frac{2\pi n_e e^3 \ln \Lambda}{T_e} \quad (3.1)$$

In a followup paper in 1960, Dreicer outlined the conditions for ion runaway

[58]. In order for ions to enter a collision-free regime and run away, they must have a speed much greater than the electron thermal speed, requiring $T_i \gg T_e$. These conditions are not typically relevant in laboratory plasmas. However, in 1972, Furth and Rutherford refined the calculations and showed that in the presence of enhanced resistivity from high- Z impurities and/or magnetic trapping of electrons, ion runaway can be achieved in tokamak-relevant conditions [59]. A brief summary of the derivation in Furth and Rutherford follows.

Consider a plasma with uniform magnetic and electric fields \vec{B} and \vec{E} . To simplify notation throughout this chapter, let the electric field be parallel to \vec{B} (i.e. $\vec{E} = E \hat{b} = E_{\parallel}$). The primary ion species has mass m_i , charge $Z_i e$ and density n_i . Due to high- Z impurities, the plasma can be considered to have an effective charge $Z_{eff} e$ such that this effective charge can be invoked in the overall quasineutrality of the plasma, $Z_{eff} n_i = n_e$.

Now, consider a test ion with mass m_{α} , charge q_{α} , and velocity v_{α} . The parallel equation of motion for this test ion is

$$m_{\alpha} \frac{dv_{\alpha}}{dt} = q_{\alpha} E - \mathcal{F}^{\alpha e} - \mathcal{F}^{\alpha i} \quad (3.2)$$

where $\mathcal{F}^{\alpha e}$ and $\mathcal{F}^{\alpha i}$ are the frictional drag terms for the test particle on electrons and ions, respectively. Each friction term can be separated into drift and rest terms:

$$\mathcal{F}^{\alpha e} = \mathcal{F}_0^{\alpha e} + \mathcal{F}_d^{\alpha e} \quad (3.3)$$

$$\mathcal{F}^{\alpha i} = \mathcal{F}_0^{\alpha i} + \mathcal{F}_d^{\alpha i} \quad (3.4)$$

$\mathcal{F}_0^{\alpha e}$ is the friction the test particle would feel if the electrons were at rest and $\mathcal{F}_d^{\alpha e}$ is the contribution due to the electron drift (and similar for ions). A frame of reference is chosen such that the bulk ions are at rest ($\mathcal{F}_d^{\alpha i} = 0$).

To calculate the friction due to electron drift, consider the force balance for the bulk electron and ion populations. For the electrons to be in equilibrium, the electric force on electrons must be exactly canceled by their drag on background ions. Thus, the electron drift friction felt by ions is:

$$n_i \mathcal{F}_d^{ie} = n_e e E \quad (3.5)$$

The functional dependence of the collisional friction on ion charge is Z^2 , so using Equation 3.5, the electron drift friction for the test ion can be written as:

$$\mathcal{F}_d^{\alpha e} = \frac{Z_\alpha^2}{Z_{eff}^2} \mathcal{F}_d^{ie} = \frac{Z_\alpha^2}{Z_{eff}^2} \frac{n_e e}{n_i} E \quad (3.6)$$

From quasineutrality ($Z_{eff} n_i = n_e$), this can be simplified to:

$$\mathcal{F}_d^{\alpha e} = \frac{Z_\alpha^2}{Z_{eff}} e E \quad (3.7)$$

Using Equations 3.3, 3.4, 3.7, and the ion rest frame condition, the equation of motion for the test particle becomes

$$\begin{aligned} m_\alpha \frac{dv_\alpha}{dt} &= q_\alpha E - \frac{Z_\alpha^2}{Z_{eff}} e E - \mathcal{F}_0^{\alpha e} - \mathcal{F}_0^{\alpha i} \\ &= q_\alpha E \left(1 - \frac{Z_\alpha}{Z_{eff}} \right) - \mathcal{F}_0^{\alpha e} - \mathcal{F}_0^{\alpha i} \end{aligned} \quad (3.8)$$

Furth and Rutherford define an “effective” electric field $E^* \equiv E \left(1 - \frac{Z_\alpha}{Z_{eff}} \right)$ so the expression can be simplified further to:

$$m_\alpha \frac{dv_\alpha}{dt} = q_\alpha E^* - \mathcal{F}_0^{\alpha e} - \mathcal{F}_0^{\alpha i} \quad (3.9)$$

Considering only the effects of impurities (and not the trapped electrons, which will be considered further below), a few features can be readily identified. First,

runaway can occur if the force from the effective electric field overcomes the friction from the bulk electrons and ions. Second, if the test particle charge is equal to the bulk plasma charge (for example, a hydrogen test particle in a hydrogen plasma with no impurities), the effective electric field becomes zero and the test particle can never run away.

In this thesis, hydrogen test particles injected with the neutral beam will be considered in a background deuterium plasma with impurities. Z_{eff} is a notoriously difficult parameter to quantify, but estimates typically range from 2 to 6. In any case, some amount of the electric field will be felt by the NBI-born test particles.

The effect of trapped electrons is considered by reexamining the force balance in Equation 3.5. Because current is carried by the passing electrons, those electrons will be in force balance with the ions and trapped electrons such that

$$n_e^{untr} eE = n_i \mathcal{F}_d^{ie} + n_e^{tr} \mathcal{F}_d^{ee,tr} \quad (3.10)$$

Carrying this through the rest of the above derivation, E^* becomes:

$$E^* = \left(1 - \frac{Z_\alpha n_e^{untr}}{Z_{eff} n_e} \right) \frac{1}{1 + \frac{n_e^{tr} \mathcal{F}_d^{ee,tr}}{n_e \mathcal{F}_d^{\alpha e}}} \quad (3.11)$$

P. Helander et al. have examined the ion runaway process in MAST [60] and have rewritten the effective electric field in a more usable (though even less visually comprehensible) form using dimensionless parameters depending on only Z_{eff} and the trapped electron fraction f_t :

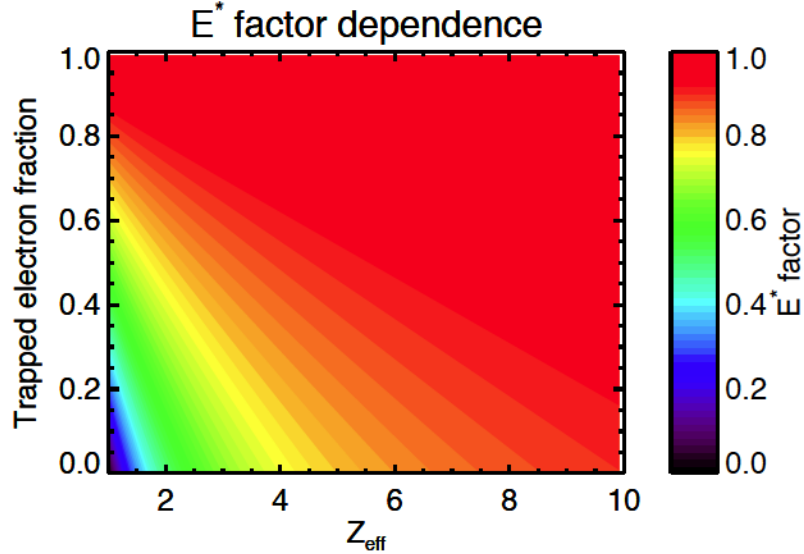


Figure 3.1: Contours of the amount of electric field felt by a test ion are plotted vs. Z_{eff} and trapped electron fraction. For the lower bound of estimates in MST ($Z_{eff} = 2$, $f_t = 0$), the test ion will still feel over 50% of the electric field.

$$\zeta = Z_{eff} - 1 \quad (3.12)$$

$$x = f_t / (1 - f_t) \quad (3.13)$$

$$\frac{E^*}{E} = \frac{\zeta}{1 + \zeta} + \frac{3.96 + 2.59x + \zeta(4.21 + 3.24x) + \zeta^2(1 + x)}{2.59(0.65 + x)(1.44 + x) + \zeta(3.24 + \zeta)(1 + x)^2} \frac{x}{1 + \zeta} \quad (3.14)$$

Equation 3.14 has been plotted in Figure 3.1 to better illustrate the dependence of the effective electric field factor on Z_{eff} and the trapped electron fraction. Note that for standard MST plasmas, the trapped electron fraction can range from 10-60% from the core to the edge (Figure 3.2(a)) and estimates for Z_{eff} range from 2-6. For $Z_{eff} = 4$, a slice of the E^* contour is plotted in Figure 3.2(b) and shows that the ions should feel roughly 75-85% for any applied electric field.

Armed with Equations 3.9 and 3.14, the motion of a test particle can be predicted if the electric field profile, collisional friction, Z_{eff} , and trapped electron fraction are known. The electric field profile and collisional friction will be discussed in the

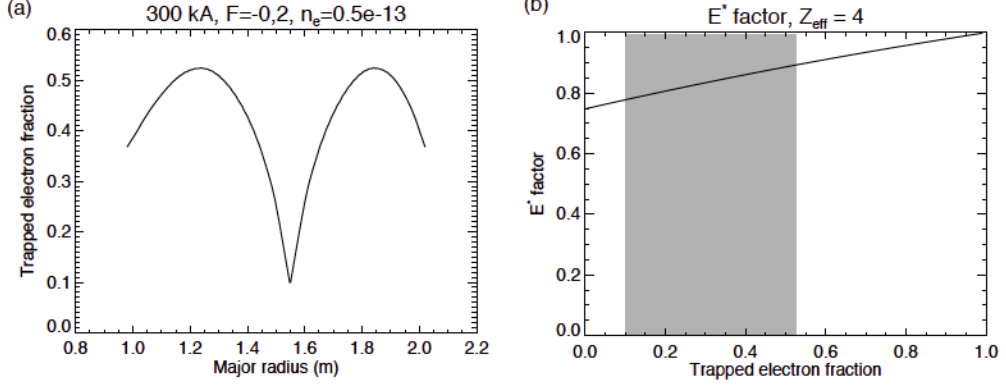


Figure 3.2: (a) The trapped fraction (as calculated by MSTFIT) can range from 10-50% in standard MST plasmas. (b) For Z_{eff} and the trapped fraction in (a), a test ion should feel 75-85% of the electric field.

following sections.

3.2 Calculation of plasma friction

The total friction a test particle encounters (after rearranging the drifting components into the effective electric field, as derived above) is given by:

$$\begin{aligned}
 \mathcal{F} &= \mathcal{F}_0^{\alpha e} + \mathcal{F}_0^{\alpha i} \\
 &= m_\alpha v_\alpha \nu_s^{\alpha e} + m_\alpha v_\alpha \nu_s^{\alpha i} \\
 &= m_\alpha v_\alpha \left\{ \left[\left(1 + \frac{m_\alpha}{m_e} \right) \psi \left(\frac{m_e v_\alpha^2}{2kT_e} \right) \frac{4\pi e^4 Z_\alpha^2 \lambda^{\alpha e} n_e}{m_\alpha^2 v_\alpha^3} \right] + \right. \\
 &\quad \left. \left[\left(1 + \frac{m_\alpha}{m_i} \right) \psi \left(\frac{m_i v_\alpha^2}{2kT_i} \right) \frac{4\pi e^4 Z_\alpha^2 Z_{eff}^2 \lambda^{\alpha i} n_i}{m_\alpha^2 v_\alpha^3} \right] \right\} \\
 &= \frac{4\pi e^4 Z_\alpha^2}{m_\alpha v_\alpha^2} \left[\lambda^{\alpha e} n_e \left(1 + \frac{m_\alpha}{m_e} \right) \psi \left(\frac{m_e v_\alpha^2}{2kT_e} \right) + Z_{eff}^2 \lambda^{\alpha i} n_i \left(1 + \frac{m_\alpha}{m_i} \right) \psi \left(\frac{m_i v_\alpha^2}{2kT_i} \right) \right]
 \end{aligned} \tag{3.15}$$

where $\lambda^{\alpha\beta} = \ln \Lambda^{\alpha\beta}$ is the Coulomb logarithm and the function $\psi(x)$ is the normalized integral of a Maxwellian speed distribution, defined as:

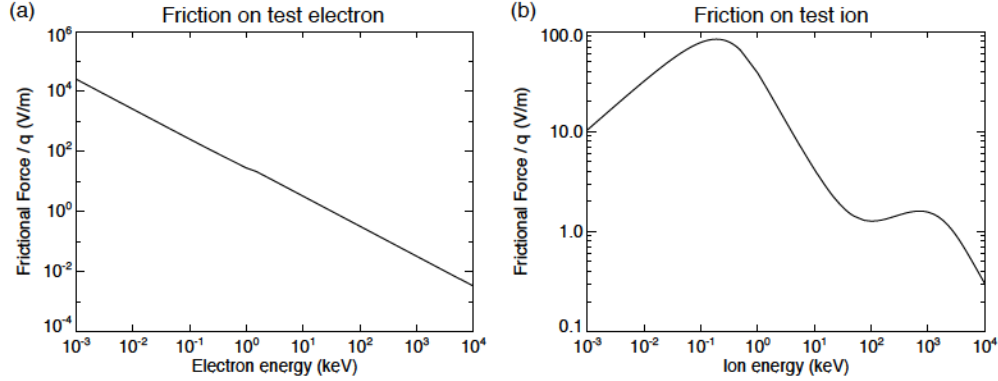


Figure 3.3: The frictional force for a test electron (a) and a test ion (b) is plotted for a typical MST plasma. Test electron slowing is always dominated by electron-electron collisions, while test ions transition from primarily ion drag at low energies to primarily electron drag at high energies.

$$\psi(x) = \frac{2}{\sqrt{\pi}} \int_0^x t^{1/2} e^{-t} dt \quad (3.16)$$

The friction is thus functionally dependent on the electron density and temperature, the ion density and temperature, Z_{eff} , and the mass and velocity of the test ion. The frictional force for a test electron and a test ion in a 300 kA, F=-0.2 plasma with $n_e = n_i = 0.7 \times 10^{13} \text{ cm}^{-3}$, $T_e = 450 \text{ eV}$, and $T_i = 400 \text{ eV}$ is shown in Figure 3.3. The friction profile for electrons is monotonic as the high speed of electrons with respect to the thermal ion speed means that the argument for $\psi(x)$ is greater than 1 for electrons and ions. However, thermal ions have a speed much less than the thermal electron speed, meaning that the argument of $\psi(x)$ transitions from much less than 1 to much greater than 1 as ion energy increases. This leads to the double-hump structure seen in Figure 3.3(b). The effects of Z_{eff} , density, and temperature are illustrated in Figure 3.4.

To imagine the effects of an applied electric field to the test particles, one can draw a horizontal line on the plots in Figure 3.3 or 3.4 at the appropriate effective electric field strength. In regions where the electric field is greater than the friction, the test

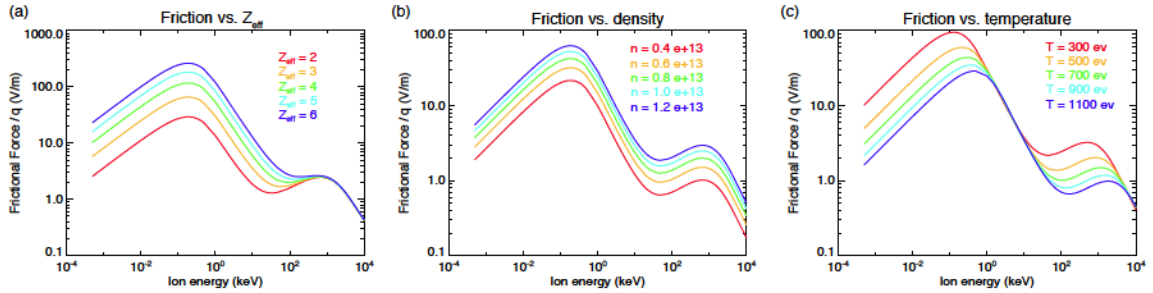


Figure 3.4: The friction on a test ion is plotted in varying plasma parameters. In (a), Z_{eff} is varied for constant density and temperature. In (b) and (c), the density and temperature are varied respectively, with $n_e = n_i$ and $T_e = T_i$. Varying the electron and ion parameters individually would shift one of the two humps, but not the other.

particle will accelerate; in regions where it is less, the test particle will slow down. If the electric field strength lies above the local minimum in the test ion friction curve but below the second local maximum, ions will accelerate up to a point where the friction balances the force from the electric field. If the electric field strength is higher than the local maximum, the ion can accelerate without bound and “run away.”

3.3 Calculation of the electric field profile

As discussed in Section 1.2, the changing magnetic fields during a sawtooth event generate inductive electric fields through Faraday’s Law. While the voltages at the toroidal and poloidal gaps give an indication of the total flux change, a measurement of the local electric field in the plasma core is needed to calculate its effects on the core-localized fast ion population.

With no direct measurement available, equilibrium reconstructions are performed using the MSTFit Grad-Shafranov solver [61]. A time series of equilibria can be constructed throughout the sawtooth cycle, and the local electric fields can be calculated from the finite differences in the magnetic field profiles. The density and magnetic field are constrained with internal measurements from the FIR polarime-

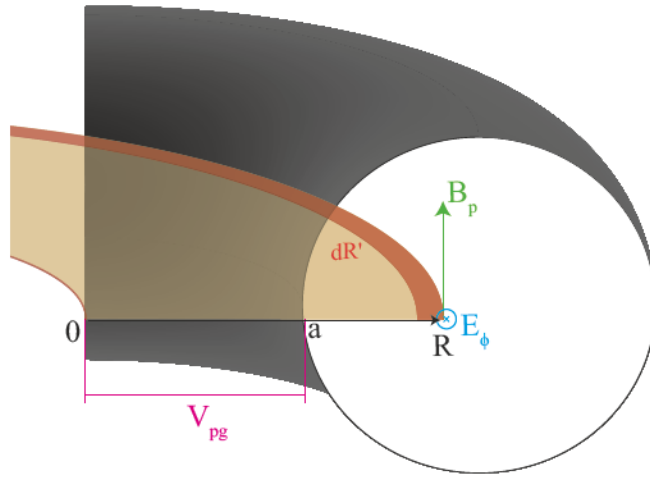


Figure 3.5: The toroidal electric field is calculated from the change in poloidal magnetic flux through a circular disc in the $R - \phi$ plane.

ter/interferometer [62–64] and edge magnetic coils, and the electron temperature is constrained with data from the Thomson scattering system.

To calculate the electric field from the changing magnetic fields, we begin with Faraday’s Law in its integral form:

$$\oint \vec{E} \cdot d\vec{l} = -\frac{d}{dt} \int \vec{B} \cdot d\vec{A} \quad (3.17)$$

If we wish to calculate the electric field in the toroidal direction E_ϕ at major radius R (and for simplicity, $Z=0$), we can consider the poloidal magnetic field B_p crossing through a disc of radius R :

$$\int_0^{2\pi} E_\phi R d\phi = -\int_0^R \int_0^{2\pi} \frac{\partial B_p}{\partial t} R' dR' d\phi \quad (3.18)$$

Here, we have brought the time derivative inside the integral by assuming that the surface of integration does not change in time. In reality, each discrete MSTFit reconstruction will have slightly varying flux surface locations. To justify moving

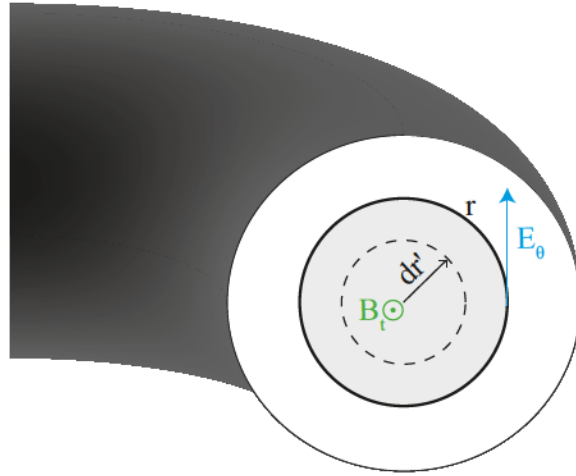


Figure 3.6: The poloidal electric field is calculated from the change in toroidal magnetic flux through a circular surface in the $r - \theta$ plane.

the time derivative inside the integral, a single set of flux surfaces is chosen, and all relevant quantities for each reconstruction are interpolated from their respective flux surfaces onto the fixed set.

By assuming toroidal symmetry and noting that $-V_{pg}$ is the voltage produced by the flux change between $R = 0$ and $R = R_0 - a$, Equation 3.18 becomes:

$$E_\phi(R, t) = \frac{1}{2\pi R} \left(V_{pg}(t) - 2\pi \int_{R_0-a}^R \frac{\partial B_p(R', t)}{\partial t} R' dR' \right) \quad (3.19)$$

Note that great care must be taken with the signs of V_{pg} and B_p , as the sign conventions are often inconsistent between the MDSPlus database and various subroutines inside MSTFit. For a more detailed handling of the signs and alternate derivations of the electric field, see Appendix B.

The poloidal electric field can be calculated in a similar manner from the change in the toroidal magnetic field. Beginning again with Faraday's Law, the change in toroidal magnetic field through a circle in the poloidal plane (Figure 3.6) is:

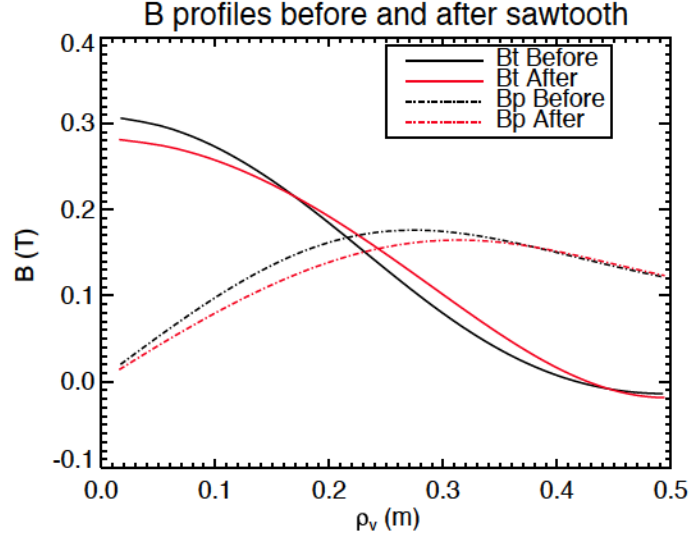


Figure 3.7: The toroidal magnetic field decreases in the core and edge, but increases throughout the mid-radius for a net increase in toroidal flux. The poloidal magnetic field decreases throughout the core and mid-radius, but increases at the edge.

$$\int_0^{2\pi} E_\theta r d\theta = - \int_0^r \int_0^{2\pi} \frac{\partial B_t}{\partial t} r' dr' d\theta \quad (3.20)$$

The assumption of poloidal symmetry cannot be made due to $1/R$ effects in the toroidal field, so we are left with:

$$E_\theta(r, t) = -\frac{1}{2\pi r} \int_0^r \int_0^{2\pi} \frac{\partial B_t(r', \theta', t)}{\partial t} r' dr' d\theta' \quad (3.21)$$

For purposes of calculating the effect of the electric field on a test particle, the component of the electric field parallel to the background magnetic field is calculated:

$$E_{\parallel} = \frac{\vec{E} \cdot \vec{B}}{|B|} \quad (3.22)$$

Results are plotted in Figures 3.7-3.9 for an ensemble of 318 sawteeth in 300 kA, $F=-0.2$ plasmas with $n_e=0.5 \times 10^{13} \text{ cm}^{-3}$. The MSTFit equilibria were constrained with FIR interferometry and polarimetry data [62–64] and Thomson scattering measurements [65], and the solver was run with the MSTFit alpha model. Unfortunately,

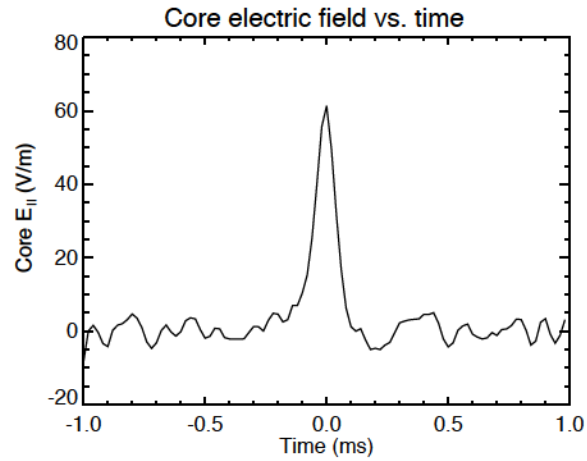


Figure 3.8: The core electric field spikes dramatically at the sawtooth crash. Peak values can range from 40-100 V/m in various plasma conditions.

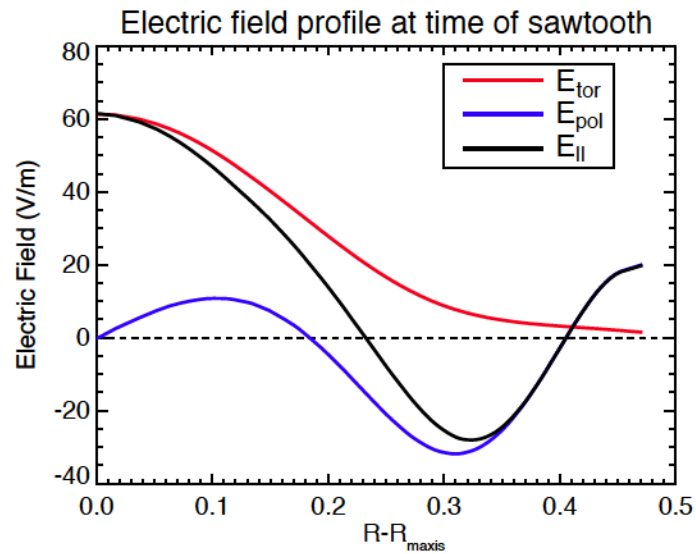


Figure 3.9: Toroidal, poloidal, and parallel components of the electric field at its peak.

the MSE measurement of $B(0)$ and Rutherford Scattering diagnostics were not available for this dataset [39, 66].

3.4 Expected energization of fast ions

With the plasma friction and full electric field profile calculated in radius and time throughout a sawtooth, the motion of a fast test ion can be predicted from Equation 3.9. First, a few assumptions are made:

- Because the TRANSP-predicted fast ion population is core-localized [25], the value of the electric field will be taken to be the average electric field within $r/a < 0.15 \pm 0.05$. Estimations of the friction, trapped electron fraction, and all other relevant quantities are averaged over the same spatial area.
- Because the typical TRANSP-predicted pitch for the core fast ions is ~ 0.8 , the effective electric field is multiplied by 0.8 ± 0.05 to estimate the component parallel to the fast ion motion. This also serves as an error bar on the calculated electric field magnitude.
- Z_{eff} is estimated to be 4 ± 1.5 .
- Because the background ions are heated at the sawtooth crash and no ion temperature measurement was available, the ion temperature is approximated as $T_i = 1.75T_e$.
- Because no ion density measurement is available, the ion density is approximated as $n_i = 0.8n_e$.

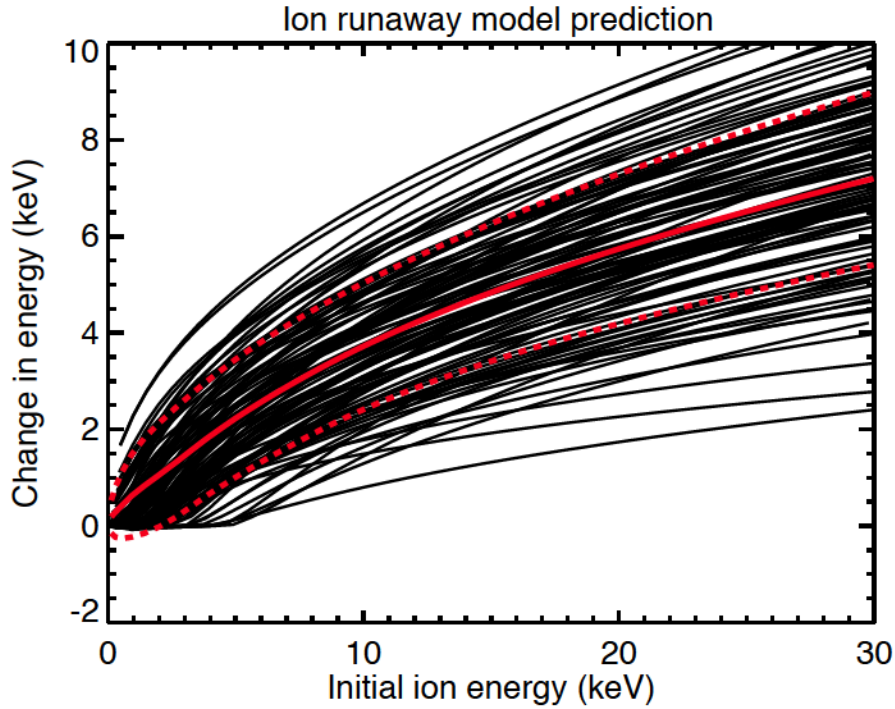


Figure 3.10: 100 predictions of ion energization with Monte Carlo variation in assumptions. The mean and standard deviation of the results are plotted in red.

- The MSTFit-calculated n_i , T_e , and T_i profiles (after the above assumptions are made) are given error bars of 20%. Due to the high time resolution internal measurements from the FIR, the n_e profile is given error bars of 10%.

Test ion motion was evolved through a sawtooth using Equation 3.9. Relevant quantities and the above assumptions were varied within their error bars using a Monte Carlo technique to determine the uncertainty in the model prediction. The results for the expected gain in energy of a fast test H^+ ion in a 300 kA, $F=-0.2$, $n_e=0.5 \times 10^{13} \text{ cm}^{-3}$ plasma are plotted in Figure 3.10. The mean and standard deviation of the collection of Monte Carlo results are plotted in red. These predictions will be compared to experimental data in the next chapter.

Chapter 4

Measurements and analysis of fast ion energization during reconnection events

In Chapter 2, initial data from the ANPA in sawtoothing discharges was shown, and energization of the NBI-born fast ion distribution was clearly observed. In Chapter 3, the electric field throughout a sawtooth was calculated and a theory proposed for how that electric field might accelerate fast ions. In this chapter, several experiments are performed to characterize that energization process and compare with predictions from the ion runaway model.

4.1 Analysis techniques

Sawtooth ensembling

Although the macroscopic characteristics of MST plasmas are very repeatable, the precise dynamics surrounding each sawtooth can vary substantially from event to

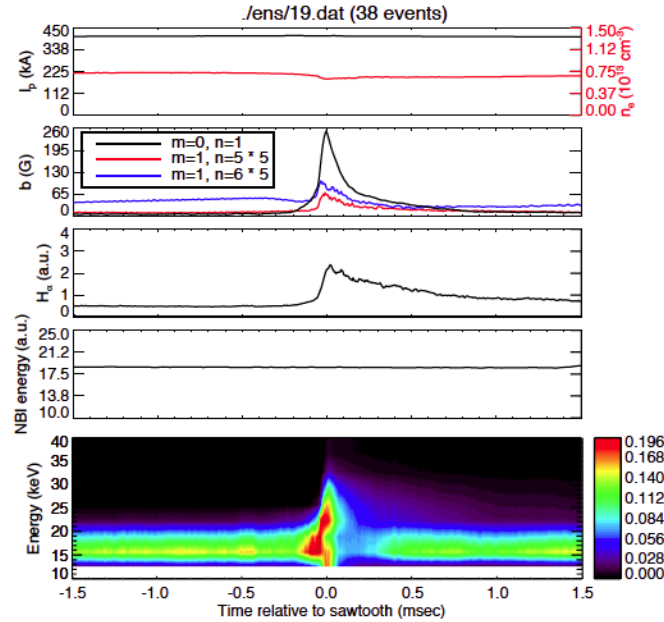


Figure 4.1: A collection of signals are collected for each sawtooth event and averaged together to reduce statistical noise.

event. It is therefore common practice to collect an “ensemble” of sawtooth events for more careful study. A number of MST plasmas are generated with similar density, current, and reversal parameter. A time marker is then chosen to identify each sawtooth event. Typically, a threshold is set on the toroidal gap voltage V_{tg} , as its value spikes dramatically at each sawtooth. The time at which V_{tg} crosses the specified threshold is designated as “ $t = 0$,” and data is collected from diagnostics of interest before and after this time. Individual events can be excluded based on deviation from the desired plasma density or other parameters. When an acceptable set of sawteeth have been collected, the measurements from each diagnostic are averaged together so that a “typical” sawtooth for the target conditions can be studied with minimal statistical error.

Sawtooth-enssembled data illustrating the gain in fast ion energy at a sawtooth event is shown in Figure 4.1. At the sawtooth crash, the plasma current and density

have small deviations upward and downward, respectively, but are otherwise held steady. The magnetic fluctuations corresponding to various tearing modes spike dramatically. Prior to the crash, ANPA signals hold at a steady amplitude around the beam injection energy (19 kV for this case). At the crash, a strong signal is seen in higher energy channels, indicating acceleration of the beam ions. Note that the H_α emission, a proxy for the background neutral density, also increases at the sawtooth. This has the effect of increasing the number of charge exchange collisions and thus the total neutral flux entering the ANPA, which would result in increased signal even for a fixed fast ion population.

Average energy formulation

By simply looking at the changes in the ANPA signals in Figure 4.1, it is hard to specify exactly how much energy was gained by the ANPA-sampled portion of the fast ion distribution. The time variation in the background neutral density further complicates the problem. In order to study how the fast ion acceleration scales with sawtooth strength and various plasma parameters, a reproducible method of quantizing the amount of acceleration is desired.

For a given normalized distribution of particles $f(U)$, the average energy of the distribution can be defined as:

$$\langle U \rangle = \int f(U) U dU \quad (4.1)$$

Translating the ANPA detector outputs into a normalized distribution function requires application of the energy response of each detector obtained during calibration. At each point in time, the ANPA records 10 hydrogen measurements and 10 deuterium measurements. Considering only one set of detectors (say, the hydrogen detectors), an ANPA measurement can be represented as a 10×1 matrix M . This

measurement is a product of the ANPA “instrument function” I and the true distribution function being measured, f . f can be discretized into an arbitrary number of energy bins n such that the instrument function I will be a $10 \times n$ matrix describing the response of each detector to an ion with energy in bin n_i of the $n \times 1$ distribution f . The measurement can then be written as the matrix equation:

$$\underset{10 \times 1}{M} = \underset{10 \times n}{I} \underset{n \times 1}{f} \quad (4.2)$$

To obtain the distribution function from the measurement, we can solve the inverse problem:

$$f = I^{-1}M \quad (4.3)$$

Because I is a non-square matrix with $n > m$, we must calculate the right one-sided inverse. The right inverse is the matrix that will satisfy $II_{right}^{-1} = \mathbf{I}_m$ where \mathbf{I}_m is the identity matrix with m rows and columns. The right inverse of a generic matrix I can be calculated as:

$$I_{right}^{-1} = I^T (II^T)^{-1} \quad (4.4)$$

By calculating the inverse of the instrument function in this manner, we can then obtain the distribution function f from a set of measurements using Equation 4.3. It is important to note that the distribution function returned will not be a unique solution; there are a number of distributions that could produce any given set of measurements M . However, the returned distribution will yield a more accurate approximation for the average energy $\langle U \rangle$ than using the measurement alone. Figure 4.2 illustrates the increase in accuracy by calculating $\langle U \rangle$ for three sample distribution functions from the raw measurement versus the approximated distribution function.

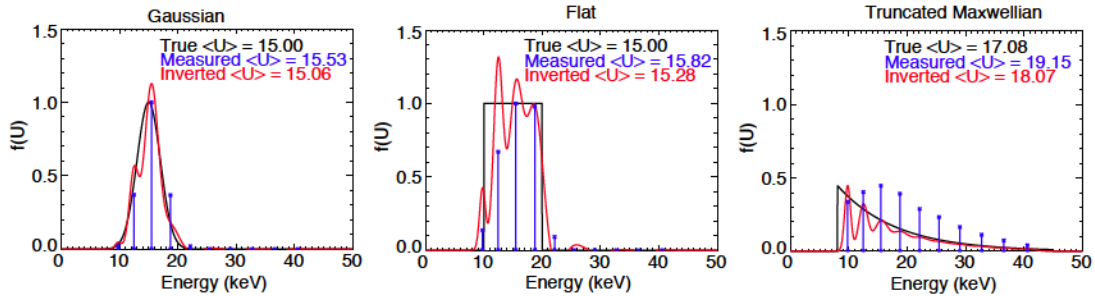


Figure 4.2: Three sample distribution functions (a Gaussian, a flat distribution, and a Maxwellian truncated to the ANPA energy range) are used to illustrate the average energy estimation from a raw 10-point measurement compared to a distribution function obtained from inverting the ANPA instrument function. For each case, the average energy of the approximated distribution is closer to the true average energy than the 10-point measurement.

The distribution function $f(U)$ could be more rigorously calculated as a linear combination of basis functions with no more than 10 free parameters; however, since the desired result of this process is the scalar $\langle U \rangle$, this method is an effective and efficient alternative.

To illustrate this technique in practice, two time slices have been chosen from the data in Figure 4.1: one well before the sawtooth at $t=-0.8$ ms, and another right after the sawtooth at $t=0.17$ ms. The approximate distribution function f has been calculated at each time and plotted in Figure 4.3. By calculating f at every time point within the ensemble window, the average energy $\langle U \rangle$ of the fast ion distribution can be plotted versus time. The overall change in energy $\Delta \langle U \rangle$ is calculated by taking the difference between the maximum energy $\langle U \rangle_{max}$ and a baseline $\langle U \rangle_{initial}$ calculated as the average $\langle U \rangle$ prior to the sawtooth (Figure 4.4).

Because the distribution function used to calculate $\langle U \rangle$ is normalized, this formulation has the added benefit of eliminating first-order effects from the change in

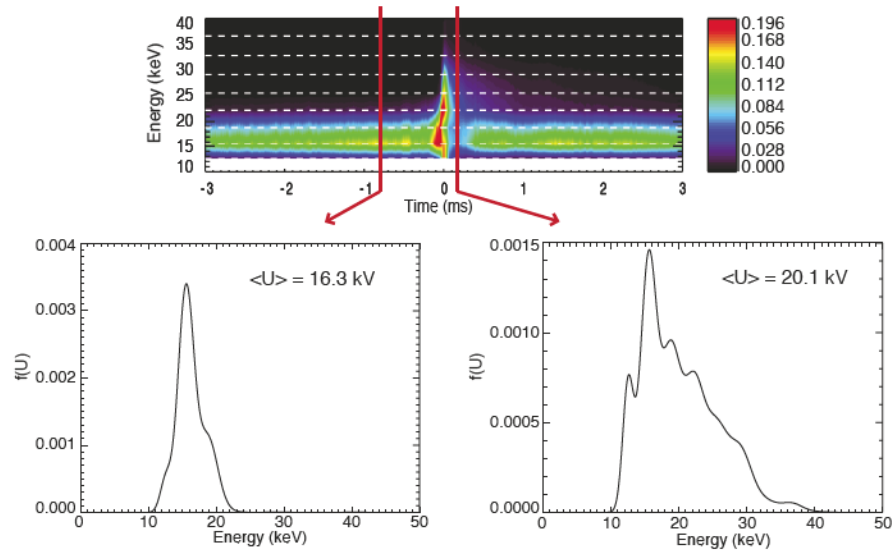


Figure 4.3: Approximate distribution functions are calculated before and after a sawtooth event for a sawtooth ensemble with 19 kV beam injection. Before the sawtooth, the distribution is approximately Gaussian and centered just below the beam injection energy of 19 kV due to slowing of the beam distribution. After the sawtooth, a high energy tail has been generated and a substantial portion of the distribution is above the injected energy.

neutral density at the sawtooth crash. More subtle changes to the neutral density radial profile could still have an impact on the measured signal, but our knowledge of the full fast ion and neutral density profiles are not accurate enough to make further corrections.

Sawtooth-triggered beam turn-off

Looking at the time trace of average energy in Figure 4.4, one might mistakenly think that the energized fast ions slow back down dramatically within 1 ms and reach their pre-sawtooth value within ~ 3 ms. However, previous work indicates the slowing time for ions of this speed should be on the order of ~ 20 - 30 ms [25]. By looking back to the full contour plot, one quickly realizes that this “slowing” is just the effect of many

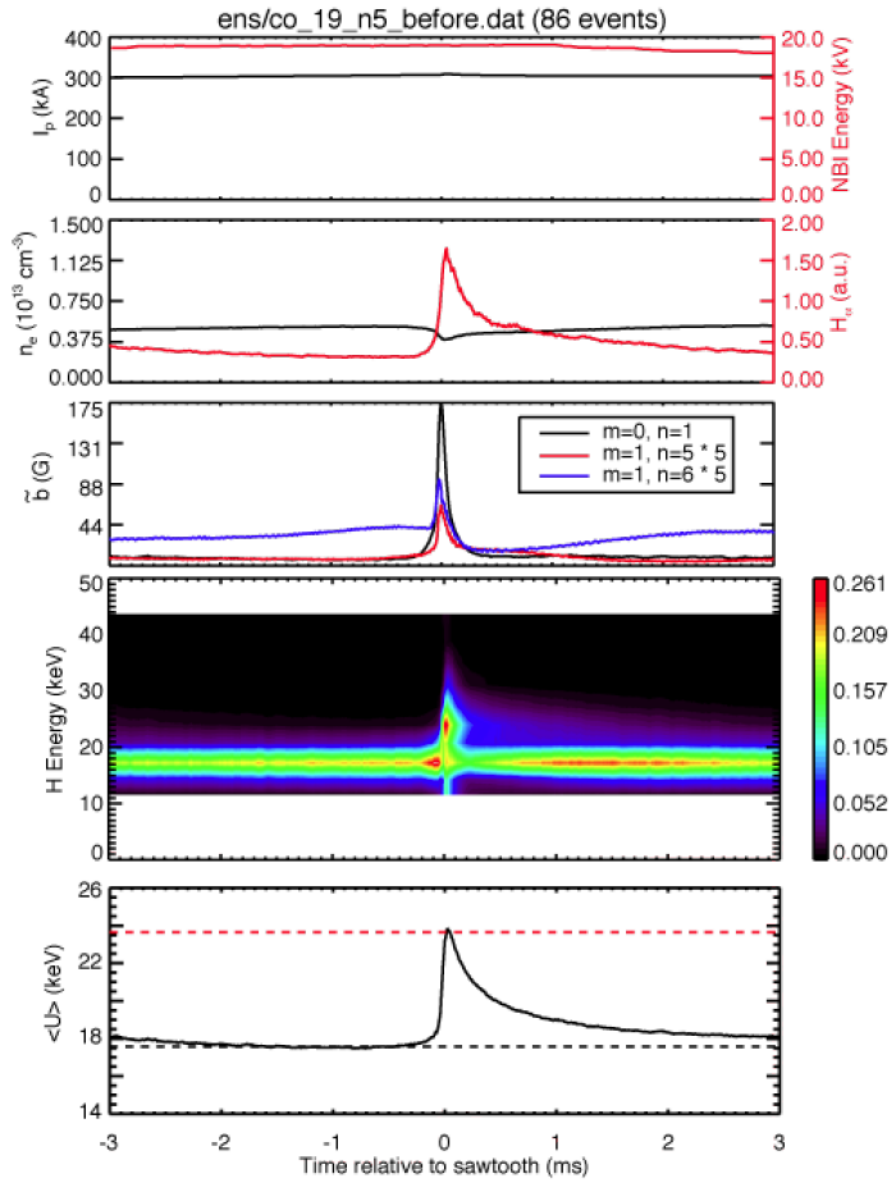


Figure 4.4: The average energy provides a much clearer picture of the ion acceleration. The change in average energy $\Delta \langle U \rangle$ can be determined from the maximum (red dotted line) minus the baseline value (black dotted line).

new, NBI-born fast ions being measured at the injection energy.

To obtain a clearer measurement of the evolution of the average fast ion energy without this false “slowing,” a system was devised to turn off the NBI at the moment a sawtooth occurs. A “sawtooth detector” circuit, previously implemented by J. Sarff [67], monitors the toroidal gap voltage V_{tg} in real-time and outputs a 5 V pulse on a trigger line when V_{tg} exceeds an user-specified threshold. A blocking time can also be set to ignore sawteeth until after a specified time in the discharge. The sawtooth detector trigger cable was wired to the NBI interlock circuit that monitors the plasma current in real time and turns off the beam if the shot misfires or terminates early. Using this setup, the beam can be turned off on the first sawtooth of a prescribed strength after a prescribed time in the plasma. For the 300 kA $F=-0.2$ plasmas used for much of the data in this thesis, the circuit was typically set up to shut off on the first sawtooth after 30 ms exceeding $V_{tg} \sim 20$ V (0.9 V on the uncalibrated V_{tg} signal). With the beam set to fire from 12-35 ms, this often resulted in 2-3 sawteeth during the beam pulse, with the beam shutting off on what would usually be the last sawtooth during its ~ 20 ms pulse time.

Figure 4.5 shows results from an ensemble of 300 kA, $F=-0.2$, $n_e = 0.5$ discharges in which the beam was turned off at a sawtooth event. Rather than being dragged down by the sourcing of additional 19 keV beam ions, the average energy increases at the crash and slows very gradually. With this technique, it is even easier to characterize the amount of energy gained at the sawtooth crash. Note that for higher densities ($n_e = 1.2$ in Figure 4.6), the colder plasma has a much faster slowing time, resulting in a quicker decrease in average energy even though the beam is off.

Using this method, if another sawtooth occurs soon after the beam turns off, the already-accelerated fast ion population can be energized to even higher levels (Figure 4.7). While this could be used to study the effects of the acceleration mechanism

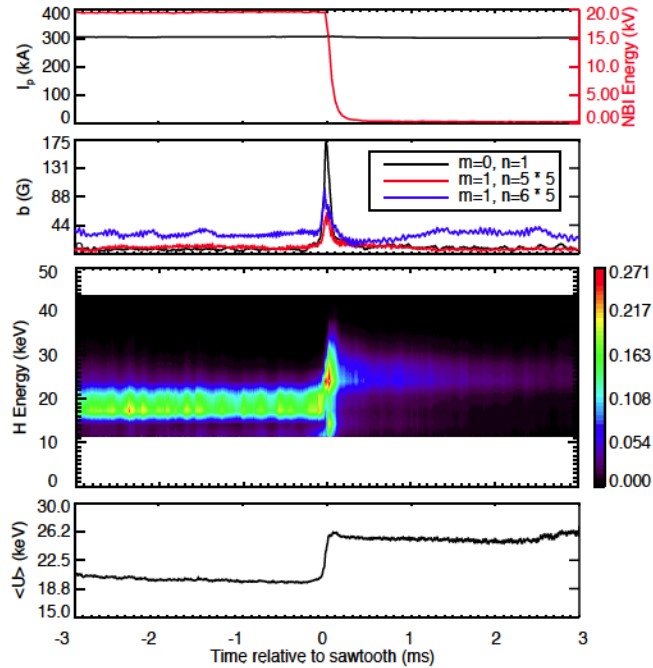


Figure 4.5: Another sawtooth ensemble using the sawtooth NBI turn-off. A clearer picture of the average energy $\langle U \rangle$ is obtained. Note that small increase in energy at the end of the time window is due to the very low signal levels after the beam has turned off. Analysis in this thesis only uses data within the first 1 ms after turn-off.

on ions at energies higher than the maximum NBI energy (25 keV), these events are uncommon and inconsistent enough that this was not attempted.

Removing contributions from the half-energy beam component

One final adjustment is necessarily to consistently calculate an accurate average energy $\langle U \rangle$. For beam energies above 20 keV, the half-energy beam component (generated from H_2 molecules in the NBI fuel) will be visible in the lower ANPA energy channels. When calculating the average energy, the presence of half-energy ions will artificially lower the average energy for these ensembles compared to cases below 20 keV where the half-energy component is not measured. To eliminate this unwanted

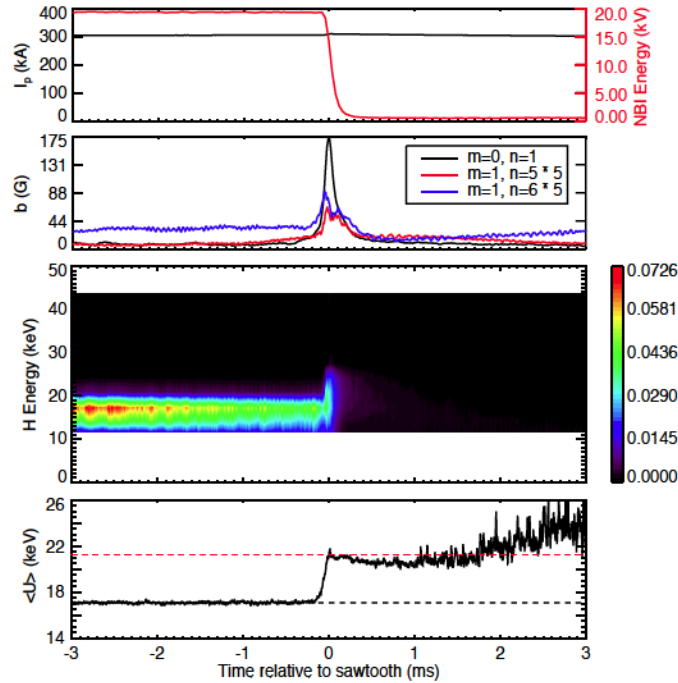


Figure 4.6: In a colder, higher density discharge, the average energy slows quicker, and the signal reaches low, unusable levels much quicker than the low density case. $\Delta \langle U \rangle$ can still be accurately calculate using the first 100-300 μs after the sawtooth.

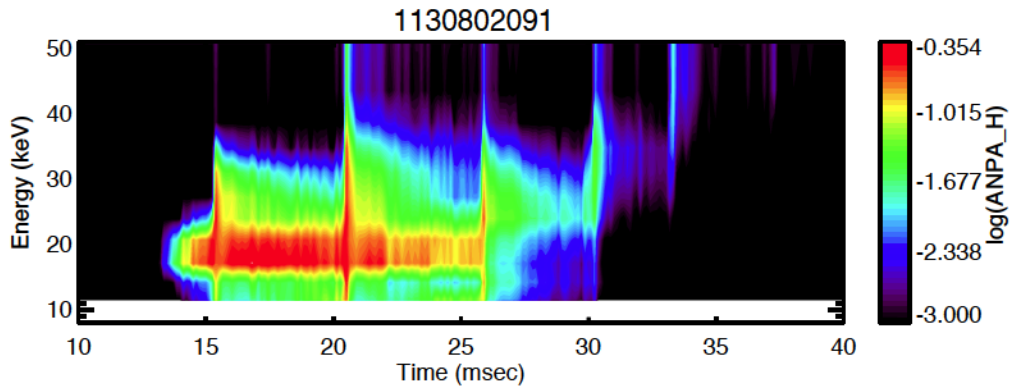


Figure 4.7: The beam is turned off at the sawtooth occurring at 26 ms. Subsequent sawteeth at 31 and 33 ms continue to ratchet up the energy of the remaining fast ion distribution.

low-energy contribution, each ensemble has its approximated distribution function f truncated at a user-selected value such that the half-energy component will not contribute to the average energy. For uniformity, the same methodology is used to truncate the ensembles in which the half-energy component is not present. This has a systematic effect on both the base $\langle U \rangle$ and the $\Delta \langle U \rangle$.

Several methodologies for choosing the truncation energy were evaluated. Success was found in most cases by automatically truncating the distribution function at values below 0.8 times the injected beam energy. However, as beam energy decreases, the amount of truncation decreases, potentially skewing the results. Additionally, in colder plasmas with more substantial slowing of the fast ions, more of the “real” distribution is truncated for a given beam energy. Instead, the truncation energies were handpicked to lie wherever the maximum signal originating from the primary beam energy begins to trail off (for example, at the bottom of the green “beam” of signal in Figures 4.5 and 4.6). This allows the truncation to remain relatively consistent when varying any number of parameters.

Error estimation

The two primary quantities of interest for each ensemble are the average energy baseline $\langle U \rangle_{initial}$ and the average energy change $\Delta \langle U \rangle$. Each is calculated as a result of the analysis procedure outlined above (including matrix multiplication, truncation, and noise subtraction if necessary). This procedure makes direct propagation of the measurement error difficult. Instead, to estimate the error for each quantity, the average energy is calculated for each individual sawtooth event. There is a moderate amount of variability from sawtooth to sawtooth, and failures in the average energy calculation for individual events are more likely due to fluctuating signal levels. However, for each ensemble, the quantities $\langle U \rangle_{initial}$ and $\Delta \langle U \rangle$ are individually plotted to

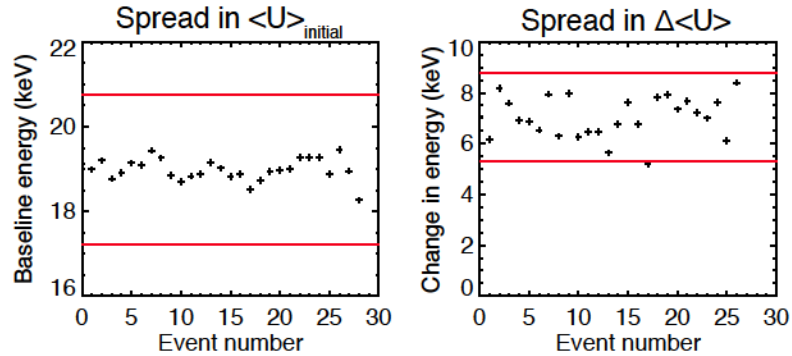


Figure 4.8: Results for $\langle U \rangle_{initial}$ and $\Delta \langle U \rangle$ for each sawtooth in a given ensemble. Red lines indicate the outlier threshold from the Grubbs' outlier test. The baseline energy calculation typically has much less spread than the change in energy because it is not affected by the individual sawtooth variability.

check that they form a rough Gaussian distribution. Outliers are detected using the Grubbs' test for outliers [68], verified by hand, and removed from the dataset. At the conclusion of this process, a standard deviation can be determined from the spread in individual sawtooth events. A sample of the typical spread is show in Figure 4.8.

4.2 Experiments to characterize fast ion energization

Scaling with electric field strength

The most obvious experiment to determine whether the observed acceleration of the NBI ions is due to the runaway mechanism described in Chapter 3 is to see if the amount of energy gain is dependent on the strength of the electric field during the sawtooth crash. The electric field was varied by adjusting the plasma current and reversal parameter. For each case, polarimetry measurements were used in conjunction with MSTFit to calculate the electric field from a time series of equilibria as

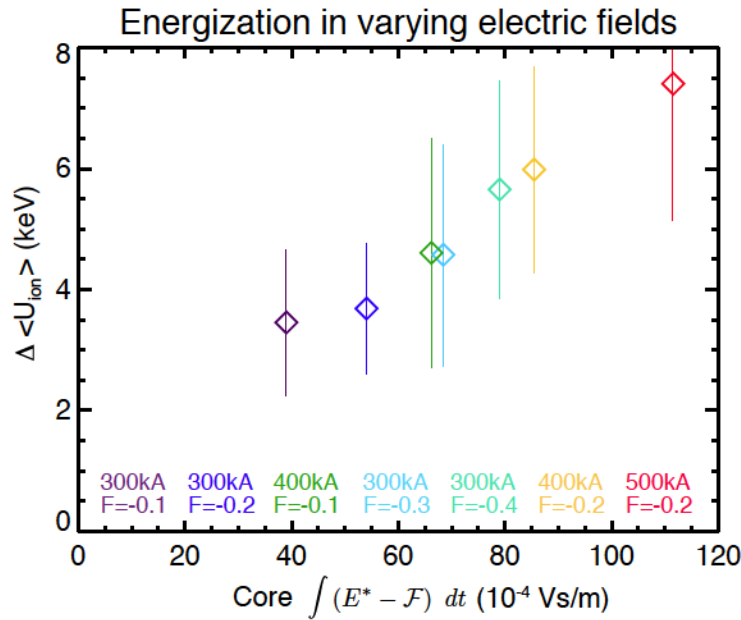


Figure 4.9: The electric field is scanned by varying the plasma current and reversal parameter. Friction is subtracted so that energization can be studied as a function of the electric field only. A positive correlation is observed.

described in Chapter 3.

Figure 4.9 shows the results of the electric field scan. The y-axis is the familiar change in measured ion energy, while the x-axis is the time integral of electric field minus the friction (one can imagine the area under the curve of a time plot of net force). A positive trend is observed between the electric field force and the ion energization. However, the electric field strength is one of many parameters that scales with the overall “strength” of the sawtooth as one moves to higher current and deeper reversal. A scatter plot of each sawtooth in the ensembles depicted in Figure 4.9 shows that the amount of energization also scales with the decrease in stored magnetic energy, a typical indicator of the sawtooth strength that is also obviously tied to the electric field strength (Figure 4.10).

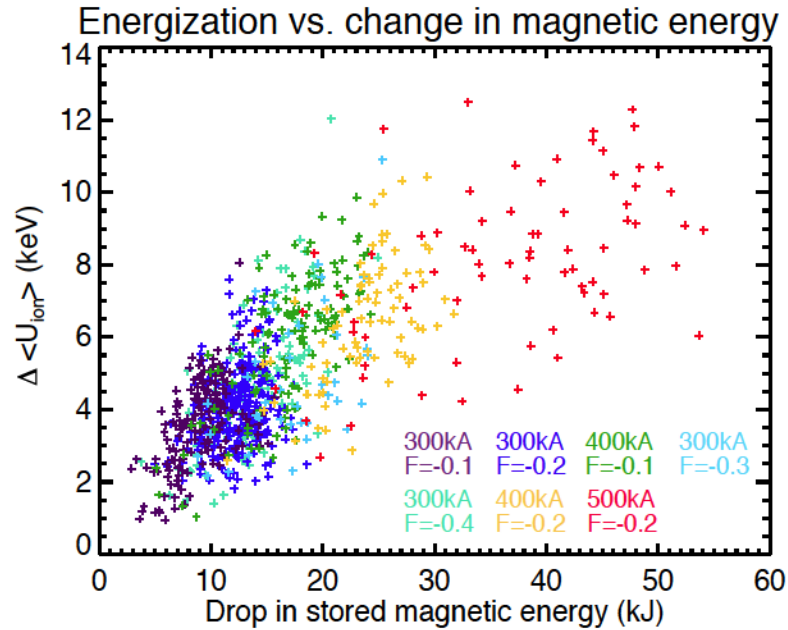


Figure 4.10: Ion energy gain is correlated with the drop in equilibrium stored magnetic energy. The colors correspond to the various plasma conditions listed in Figure 4.9.

Scaling with initial ion energy

Another testable prediction from the ion runaway theory is that the amount of energy gain at a reconnection event should scale with the initial ion energy. Other theories, such as a first-order Fermi process from a multi-island reconnection process [33], predict a similar scaling. A careful study of the relationship between initial energy and energy gain is necessary to support or disqualify these theories.

To test this, the injection energy of the neutral beam was varied from its maximum energy of 25 keV down to 10 keV, at which point beam operation becomes unreliable. Initially, the beam current was lowered proportionally with the beam energy such that a constant injected number density of fast ions was maintained; however, the results had no dependence on the beam current, so in the final data sets, the maximum beam current at each energy setting was used to maximize ANPA signal.

The results of the beam energy scan are presented in Figure 4.11. A positive

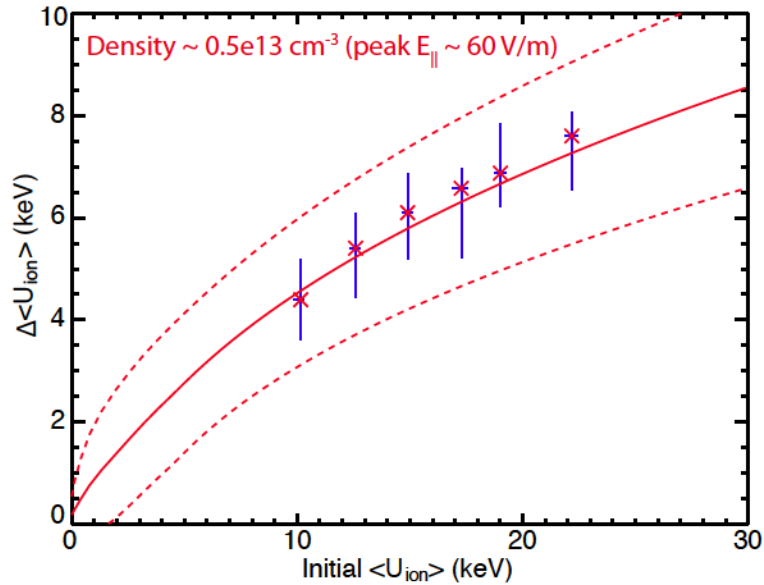


Figure 4.11: Ion energy gain has a positive dependence on the initial ion energy and agrees well with quantitative predictions from the ion runaway model. Note that the error bars are centered around the mean of the distribution of $\Delta \langle U \rangle$'s calculated for each sawtooth, and are thus not necessarily symmetric around the $\Delta \langle U \rangle$ of the ensemble-averaged data.

dependence is observed, roughly scaling as $E^{1/2}$. The solid line is the prediction from the ion runaway theory using the electric field calculated for these plasmas (300 kA, $F=-0.2$, $n_e = 0.5 \times 10^{19} \text{ m}^{-3}$). The dotted lines represent uncertainty in the ion runaway modeling, calculated by varying the assumptions about Z_{eff} , core-localization and pitch of the measured fast ions, and T_e/T_i ratio within reasonable ranges. The value assumed for Z_{eff} for the solid lines is 4, which provided the best agreement between the data and the model.

To further explore the dependence of both the initial ion energy and the electric field strength on the observed ion acceleration, a full beam energy scan was performed in two different plasma conditions. After a survey of many target conditions (e.g. various plasma currents, densities, and reversal parameters), the single MST

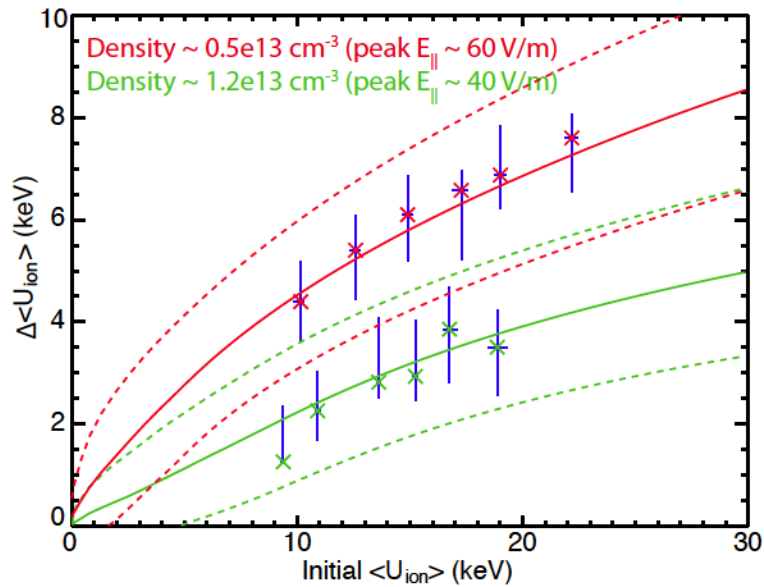


Figure 4.12: Beam energy scans performed at low and high densities both scale with initial ion energy. Less acceleration is observed at higher density due to increased resistivity (leading to a lower electric field) and increased friction. All measurements agree with ion runaway model predictions.

operational parameter that caused the largest change in measured ion energization was the plasma density. Higher plasma density results in lower temperature and therefore higher resistivity (for a given plasma current). Additionally, the friction is higher creating a larger drag force that must be overcome by the energization process. Figure 4.12 shows the result of the energy scans in 300 kA, $F=-0.2$ plasmas with line-averaged electron densities of $0.5 \times 10^{13} \text{ cm}^{-3}$ and $1.2 \times 10^{13} \text{ cm}^{-3}$.

Deceleration in counter- I_p beam injection

The direction of the toroidal electric field is such that it reinforces the core plasma current (it is inductively fighting the decrease in core current due to the flattening of the current density profile). By flipping the direction of the plasma current with respect to the MST vacuum vessel, we can then flip the direction of the electric

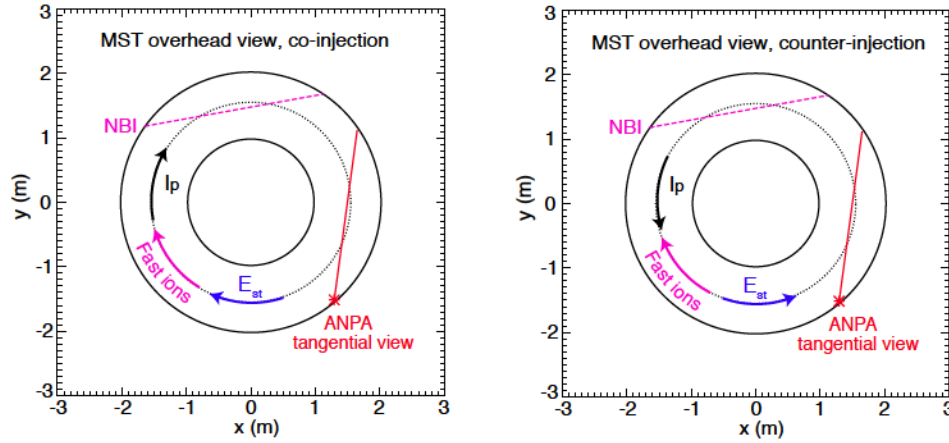


Figure 4.13: By flipping the direction of the plasma current, the orientation of the sawtooth electric field and the fast ion velocity can be reversed.

field with respect to the fast ions, which are always injected in the $+\hat{\phi}$ direction (Figure 4.13). The current is flipped by simply reversing the direction of the current flowing through the poloidal field windings. Because the poloidal magnetic field is generated by the plasma current, it is also flipped in this configuration. Using the NBI with the current in the reversed direction is commonly referred to as “counter-injection.”

Figure 4.14 shows ANPA data during a single, standard MST discharge with the current direction flipped. Rather than the spike in signal levels in the higher energy channels, a rapid deceleration of the ion population is observed at each sawtooth event. Upon varying the beam energy and ensembling many similar events (Figure 4.15), the amount of deceleration observed is proportional to the initial ion energy and plasma parameters, mirroring the effect seen in Figure 4.11.

The ion runaway prediction for deceleration in Figure 4.15 does not match the data as well as the co-injection prediction. The electric field was calculated from the same equilibrium reconstructions as the co-injection case with the assumption that $B_p^{counter}(R, t) = -B_p^{co}(R, t)$. The discrepancy between the data and model is not

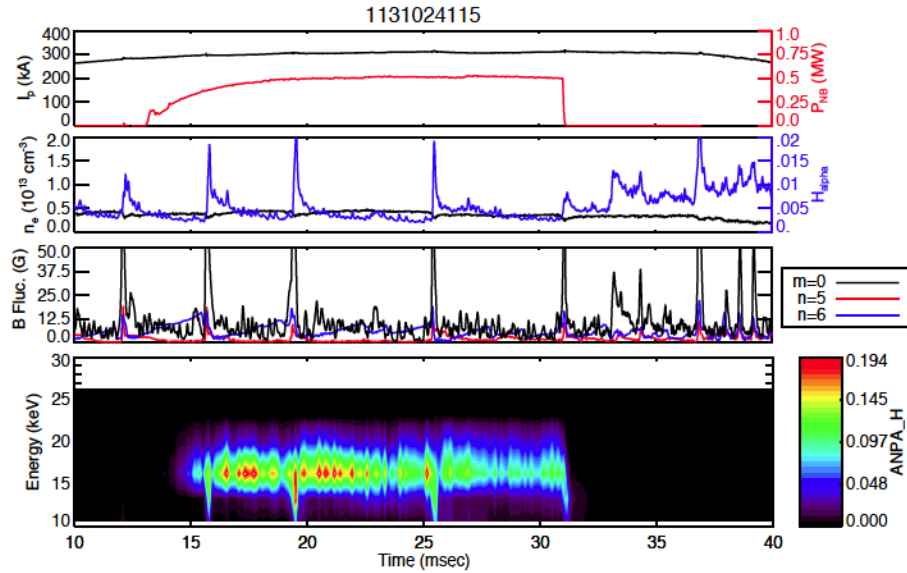


Figure 4.14: Deceleration of the fast ions is observed at sawteeth during counter-current beam injection

yet fully understood, but several diagnostic effects could cause error in the data that is not accounted for. First, because of high prompt losses and lower confinement, signal levels are lower in counter-injection, making the analysis more susceptible to noise (particularly at low beam energies and higher densities). Second, the spatial and pitch distribution of NBI-born fast ions is likely different in counter-injection, but has not been extensively modeled. Such changes, if significant, would affect the ANPA measurement space as well as the assumptions used to predict the particle behavior in the runaway model. Third, the constant slowing due to drag and the increased losses at the sawtooth get mixed in with the decelerating ions. In co-injection, truncation is used to get rid of the half-energy beam component and also to mask these effects from the analysis; however, in counter-injection, the distribution is not truncated since the ions of interest are those below the beam distribution. In the high density cases, the slowing due to drag is very significant and perhaps greater than the deceleration due to the electric field (which is weaker in the high density

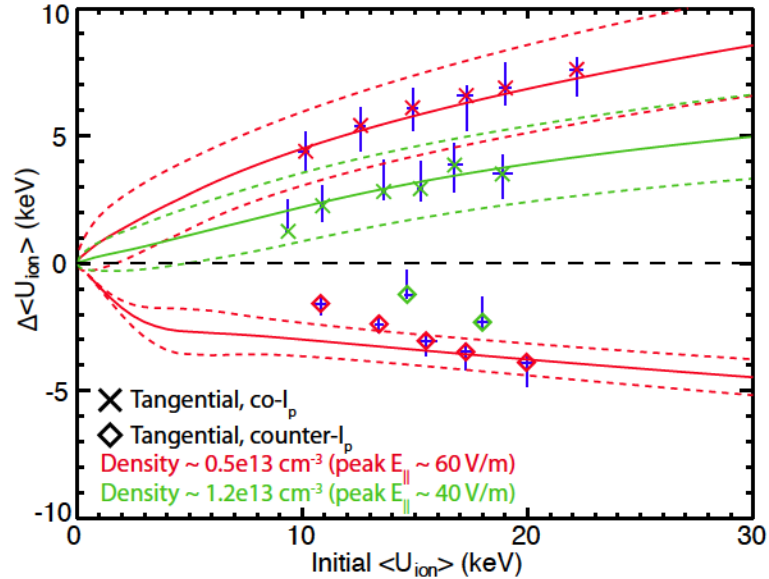


Figure 4.15: The amount of deceleration in counter-injection scales with the initial ion energy and the electric field strength. The data does not match the model as closely in counter-injection; this could be due to a number of diagnostic effects.

plasmas). Because of extensive uncertainty due to these complications, no model is presented for the high-density counter-injection data.

Changes to the distribution during deceleration could also affect the ANPA’s ability to measure the decelerated ions. For the lowest energy ensembles, the ANPA accelerating grid is used to lower the ANPA’s energy range and capture as much of the deceleration as possible, but the ions likely continue to decelerate below the range of the ANPA. This effect would be less significant in the high-energy injection ensembles, as the ions have more “room” to decelerate within the ANPA measurement range. This would result in a true deceleration that is greater than the measurable deceleration for the low-energy cases (possibly bringing those data points in line with the model). Additionally, the pitch of the ions will be lowered as they lose parallel energy, and they may also begin to move outward in radius [31]; both effects could cause them to no longer be within the ANPA measurement space. This effect would

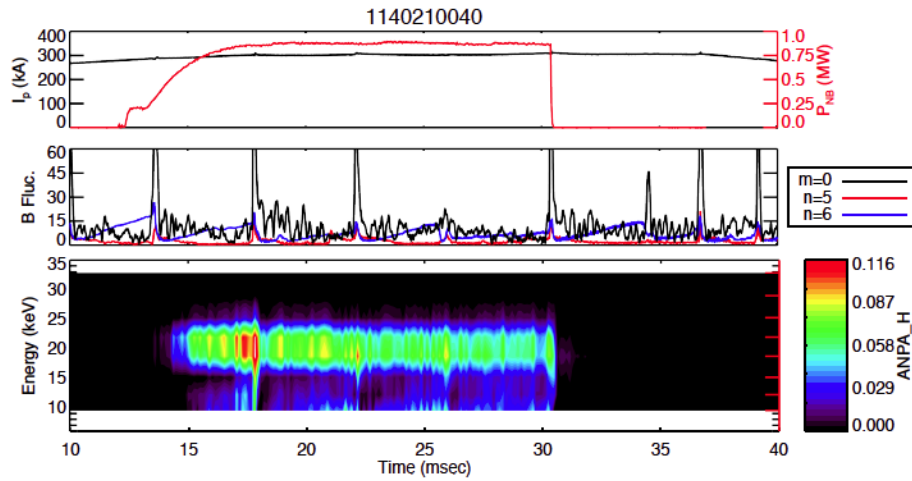


Figure 4.16: No significant acceleration is observed when the ion population is viewed from the radial ANPA port.

also disproportionately affect the low-energy data points.

Any or all of these factors could be at play and cause the discrepancy between the data and the model. However, despite the disagreement, the measurements clearly show that the ions decelerate rather than accelerate in counter-injection. These measurements prove that the fast ion acceleration is directly tied to the parallel inductive electric field. None of the other theories considered for anomalous ion heating (ion-cyclotron heating, stochastic heating, multi-island or x-point reconnection) would exhibit such a dependence.

Dependence on ANPA viewing angle

A final test to determine the relationship between the parallel electric field and the observed increase in ion energy is to use the radial ANPA viewport to sample the perpendicular component of the fast ion energy throughout the sawtooth crash. Since the electric field will primarily influence the parallel component of the ion velocity, little or no acceleration should be seen on the perpendicular measurement.

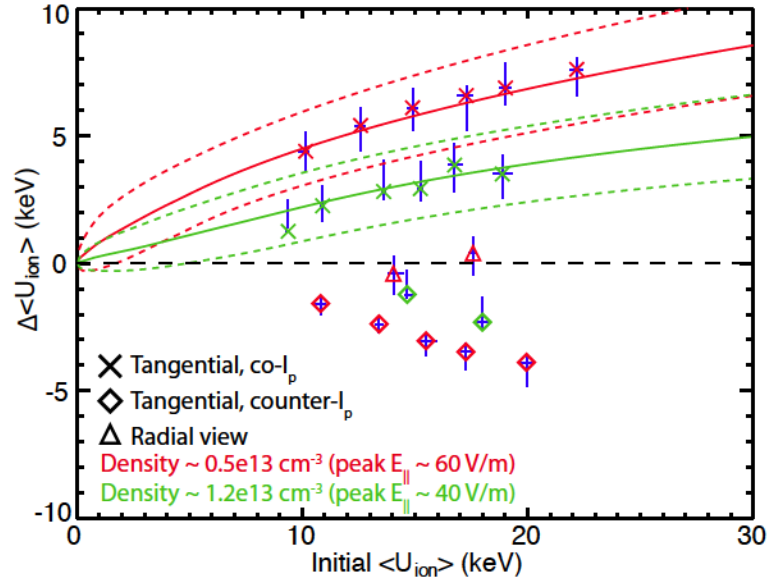


Figure 4.17: Data ensembled from many sawteeth indicate no perpendicular acceleration of the fast ion population across several beam energies.

Figure 4.16 shows radial ANPA data from a single discharge, and indeed, no obvious acceleration is observed. Note that UV and particle noise is much worse on the radial view, so the noise subtraction methods detailed in Section 2.6 are used (noise subtraction was not necessary for the tangential view data). At some sawteeth, it appears as if the population is decelerating as in counter-injection. This is likely a combination of particle loss, imperfect noise subtraction, and an increase in neutral density resulting in higher flux at all measured energies.

Performing an ensemble analysis of many events at two different injection energies (triangles in Figure 4.17) confirms that the average ion energy does not change within the error of the measurement.

4.3 Summary of results

The behavior of NBI-born fast ions during MST sawteeth was studied in a variety of plasma conditions. In all cases, the magnitude of acceleration or deceleration was dependent on the inductive electric field generated from the magnetic flux change during reconnection as well as the initial ion energy. In co-injection, ions are accelerated and agree well with predictions from the ion runaway model. In counter-injection, ions are decelerated. Other ion heating models are symmetric and would not predict such a dependence on the plasma current or electric field direction. In addition, when the ANPA samples the perpendicular component of the fast ion distribution from a radial viewport, no significant acceleration or deceleration is observed, further supporting the theory that the source of energization is the parallel inductive electric field.

Chapter 5

Bulk ion heating and other implications

In the previous chapter, evidence was presented that the inductive electric field generated from global changes in the magnetic flux during reconnection events in the RFP is responsible for the observed acceleration of suprathermal particles. The next logical question is: can this mechanism explain previous measurements of bulk and impurity ion heating?

By revisiting plots of the expected friction (Figure 3.3) and runaway acceleration (Figure 3.10), one might guess that thermal ions will be overwhelmed by the large frictional force at low energies and therefore experience little or no acceleration from the electric field. The problem with this interpretation is that the ion runaway formulation in Chapter 3 centers around the forces on a *test particle*. When considering thermal particles, the drag on our low-energy test ion comes from other ions of similar energies, so the energy lost to drag will largely remain in the ion population. To properly model the effect of the sawtooth electric field on the entire ion distribution function, a more complex physical model is necessary. In this thesis, the CQL3D

Fokker-Planck code [69] is used to perform these calculations.

5.1 Modeling with the CQL3D code

The CQL3D code was designed to study the evolution of particle distributions in a number of toroidal applications, including RF heating, neutral beam injection, and electron runaway studies. In this section, the Fokker-Planck equation and CQL3D code are described, and results from the code are presented to show the effects of a large, pulsed electric field on fast and thermal particle distributions in MST.

The Fokker-Planck equation

The general form of the Fokker-Planck equation in a magnetized plasma is:

$$\frac{df}{dt} = \frac{\partial f}{\partial t} + \mathbf{v} \cdot \frac{\partial f}{\partial \mathbf{x}} + \frac{q}{m} [\mathbf{E} + \mathbf{v} \times \mathbf{B}] \cdot \frac{\partial f}{\partial \mathbf{v}} = \mathcal{C}(f) + \dots \quad (5.1)$$

Simply put, it describes the time evolution of a particle distribution function f in the presence of electric and magnetic fields. The term $\mathcal{C}(f)$ is the collision operator, and other terms can be added to represent particle sources, sinks, diffusion, and other modifiers to the distribution function. The equation is six-dimensional (three velocity and three spatial dimensions), which can be computationally burdensome. As one might predict from the name, CQL3D reduces the dimensionality down to three independent variables (the CQL portion stands for Collisional Quasi-Linear). Only a brief description of the modeling procedure is given here; for the full derivation, please see the CQL3D User's Manual [70].

Three assumptions are invoked to reduce the dimensionality: first, the typical assumption of spatial symmetry in the toroidal direction; second, the gyroperiod is small compared to a collision time ($\omega_c^{-1} \ll \tau_{coll}$); and third, the toroidal tran-

sit/bounce time is smaller than the collision time ($\tau_b \ll \tau_{coll}$). In general, the last two assumptions are valid if the plasma is considered to be in a low-collisionality regime. At a given radius, these three assumptions ensure an equal distribution of particles toroidally along a field line and azimuthally around a field line. With knowledge of the field line geometry, the velocity vector \vec{v} can be broken down into the components $[v_{\parallel}, v_{\perp}]$, or alternatively a speed and pitch. Thus, the three dimensions considered in CQL3D are the radial coordinate ρ , the momentum per rest mass u , and the pitch angle with respect to the field line θ_0 .

The code also makes an assumption of zero banana width. Let ρ_L^{pol} be the Larmor radius calculated using the poloidal magnetic field (in other words, the effective banana width); then, $\delta = \rho_L^{pol}/a$ will be a small parameter. With these assumptions in place, the left-hand side of Equation 5.1 becomes:

$$\frac{df}{dt} = \frac{\partial f}{\partial t} + v_{\parallel} \hat{b} \cdot \frac{\partial f}{\partial \mathbf{x}} + qE_{\parallel} v_{\parallel} \frac{\partial f}{\partial \epsilon} + \mathcal{O}(\delta) \quad (5.2)$$

where $\epsilon = (\gamma - 1)mc^2$ is the kinetic energy of the particle. The $\mathbf{v} \times \mathbf{B}$ term from Equation 5.1 is included in the $\mathcal{O}(\delta)$ term because $v_{\perp} \sim v_D \sim \delta$. By invoking the low collisionality assumption and ordering terms according to a second small parameter $\zeta = \tau_b/\tau_{coll}$ (such that $f = f_0 + f_1(\zeta) + f_2(\zeta^2) + \dots$), the first-order component of the distribution function can be solved as:

$$\frac{\partial f_0}{\partial t} + \left\langle \left\langle \frac{qE_{\parallel}}{m} \frac{\partial f_0}{\partial u_{\parallel}} \right\rangle \right\rangle = \langle \langle \mathcal{C}(f) + \dots \rangle \rangle \quad (5.3)$$

Here, $\langle \langle \alpha \rangle \rangle$ denotes the *bounce average* of quantity α :

$$\langle \langle \alpha \rangle \rangle \equiv \frac{\oint \alpha d\tau}{\oint d\tau} ; \quad \tau \equiv \frac{d\ell_B}{|v_{\parallel}|} \quad (5.4)$$

and the integral is taken along the particle orbit from the point of minimum B to either the turning point (for trapped particles) or point of maximum B (for passing particles).

The right-hand side of Equation 5.3 can contain a number of optional terms based on what the user is modeling. In general, the right-hand side can be represented as:

$$\langle\langle \mathcal{C}(f) + Q(f) + H(f) + S(f) + R(f) + S \rangle\rangle \quad (5.5)$$

where $\mathcal{C}(f)$ is the Coulomb collision operator, $Q(f)$ is an RF quasilinear diffusion operator, $H(f)$ is a synchrotron radiation term, $R(f)$ is a radial diffusion operator, and S is a particle source/sink term. For the modeling in this thesis, only $\mathcal{C}(f)$ is used.

Modeling the fast ion tail

Before checking whether CQL3D predicts the previously measured ion heating, a test was run to see if it can accurately reproduce the results for fast ion runaway. While CQL3D does couple to the neutral beam injection modeling code NFREYA [71] and also has a virtual NPA diagnostic, a simpler approach was used to make use of existing modeling efforts. The approach taken is to define the total ion distribution as $f = f_M + f_{fi}$ where f_M is a Maxwellian at the bulk ion temperature and f_{fi} is the fast ion distribution output from the TRANSP code [52]. This distribution is evolved via the Fokker-Planck equation and interacts with simple static Maxwellian distributions for the electrons and impurities. Impurities included are C^{+6} , C^{+5} , C^{+4} , B^{+5} , and O^{+5} with densities and temperatures approximated from past CHERS measurements. The electric field profile, equilibrium magnetic field profile, and bulk particle density and temperature profiles are obtained from MSTFit reconstructions of the 300 kA, $F=-0.2$, $n_e = 0.5 \times 10^{13} \text{ cm}^{-3}$ discharges presented in Chapters 3 and 4. For the

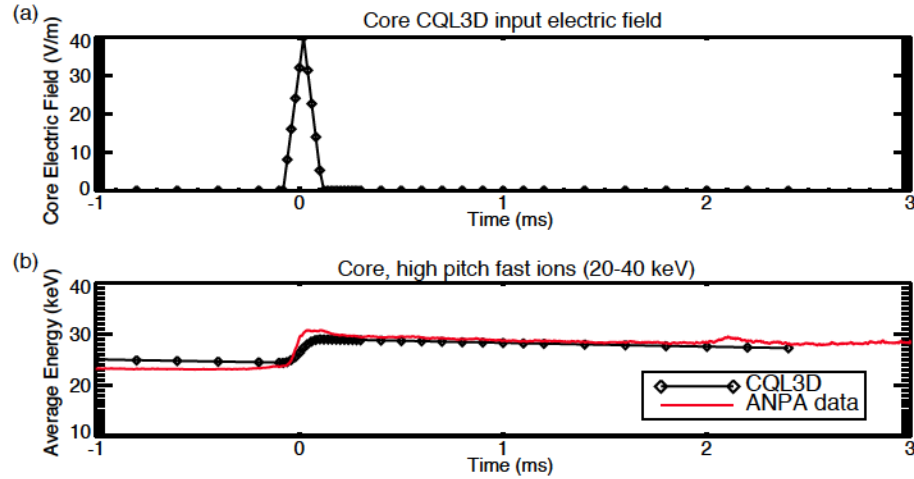


Figure 5.1: (a) The core electric field ramps up to 40 V/m over 100 μ s and decays back to zero. (b) The average energy of ions in the ANPA measurement space matches the actual ANPA measurement.

CQL3D simulation, only the electric field profile and ion distribution are evolved through time; all other quantities are held static.

The results of the run are plotted in Figure 5.1. To obtain a virtual ANPA measurement from the CQL3D distribution function, the full ion distribution is truncated to the pitches and energies measured by the ANPA (as modeled in Chapter 2) and then renormalized. Thus, the CQL3D curve in Figure 5.1(b) is the average energy of the core-localized, high-pitch ions between 20-40 keV (representing the energy range of the ANPA after the half-energy truncation procedure used in Chapter 4). The ANPA measurement plotted in red is the average energy $\langle U \rangle$ from the 24 keV NBI data point in the corresponding $n_e = 0.5 \times 10^{13} \text{ cm}^{-3}$ dataset. The CQL3D model matches the measurement well, providing further confirmation that the acceleration mechanism for these ions is the pulsed inductive electric field.

Seeing that the ANPA-measured portion of the distribution matches, the rest of the CQL3D distribution function can be examined to gain a better understanding of how the electric field affects the fast ion population. In Figure 5.2, the distribution

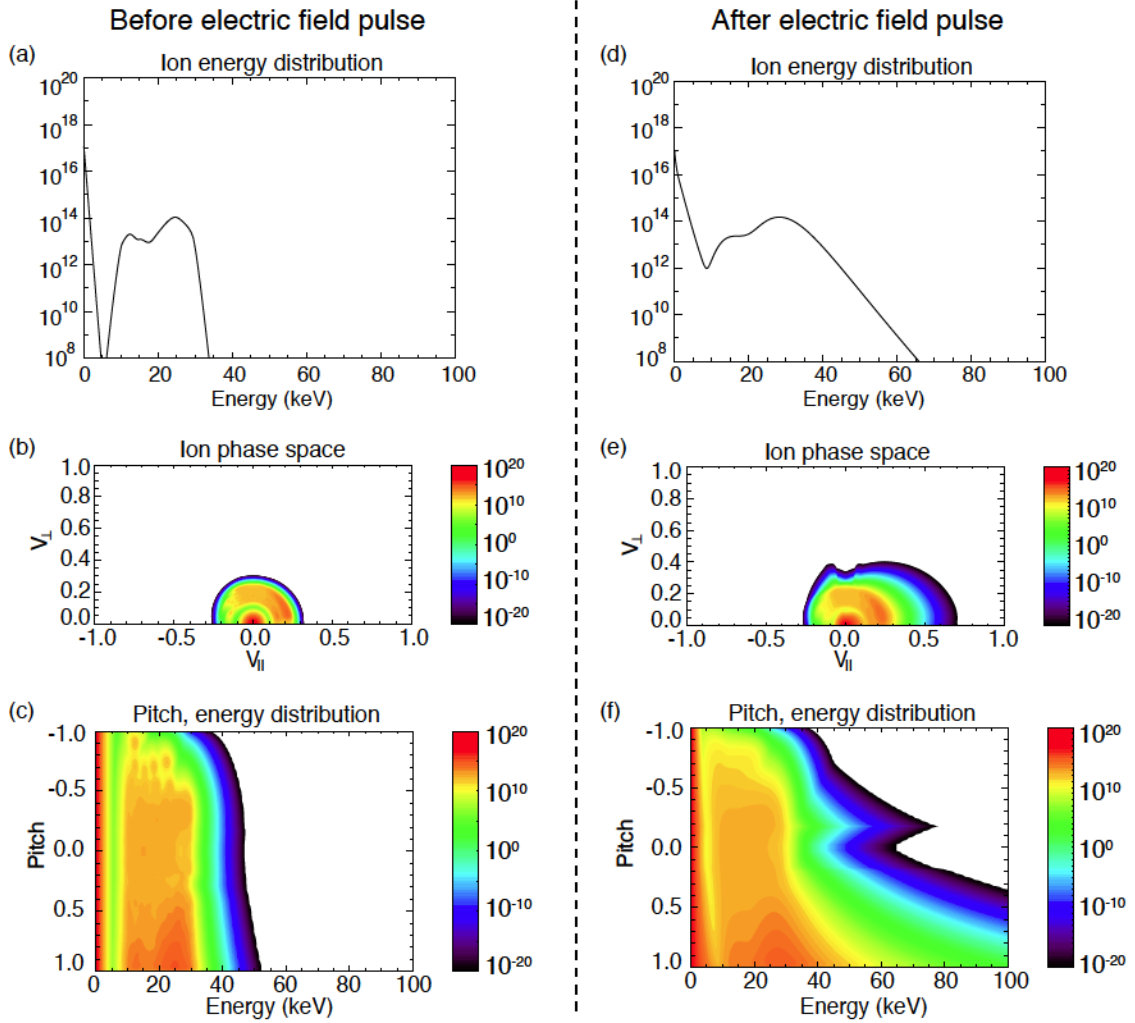


Figure 5.2: The ion distribution function (bulk + NBI contributions) is modeled in CQL3D. Plots (a), (b), and (c) depict the energy, velocity space, and pitch distributions before the sawtooth electric field is applied; (d), (e), and (f) depict the same distributions after. All distributions are taken from the core-most flux surface ($r/a = 0.05$). Note the logarithmic color scales for particle density; the high-energy, low-pitch feature in (f) is a low-significance artifact from the bounce-averaged collision operator that enforces symmetry across the trapped-passing boundary. Given enough time, pitch-angle scattering will fill in the trapped region.

function is plotted in three different ways before and after the electric field pulse. Before the sawtooth, the input ion distribution can clearly be broken up into the high-energy, high-pitch NBI distribution on top of the isotropic background Maxwellian. After the electric field pulse, the fast ions are accelerated to even higher energies, and the acceleration occurs at high pitch (i.e. the acceleration is parallel). Some acceleration of the bulk component is also observed.

Modeling bulk and impurity ions

Due to troubles with the corresponding neutral beams, neither the Rutherford Scattering [66] or CHERS [39] diagnostics were available to take data for this thesis. Instead, the comparison for bulk and impurity ion heating is made using a set of well-diagnosed MSTFit equilibria in J.A Reusch's thesis [72]. These equilibria come from an ensemble of sawteeth in 400 kA, $F=-0.2$, $n_e = 1.0 \times 10^{13} \text{ cm}^{-3}$ discharges and include Rutherford Scattering data. CHERS measurements of the C^{+6} temperature evolution are taken from work done by R. M. Magee [18, 42] in similar discharges.

CQL3D was set up to track both the D^+ (with no added NBI distribution) and C^{+6} ion distributions through time using static Maxwellian populations for the electrons and other impurities. Results are shown in Figure 5.3. Direct quantitative comparison with the Rutherford Scattering and CHERS data is discouraged due to a large range of potential input error (e.g. density and temperature profiles for every impurity is not well known, diffusion and loss terms may not be properly configured). Additionally, it should be pointed out that the CQL3D output is the *energy* of the (non-Maxwellian) distribution function rather than the Maxwellian *temperature* measured by the diagnostics. However, several important qualitative differences can still be identified.

First, the time history of the Rutherford Scattering measurement (a measurement

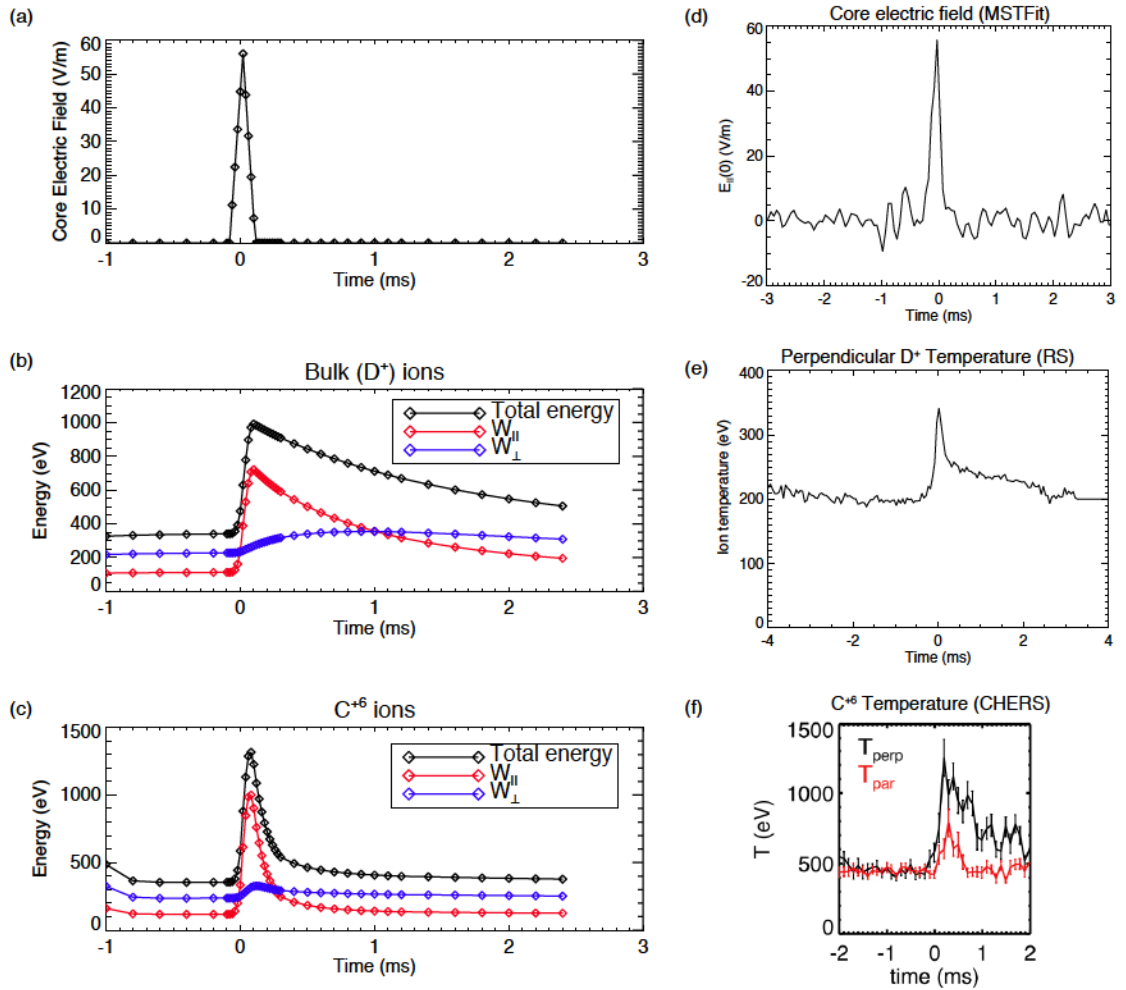


Figure 5.3: CQL3D modeling of bulk and impurity energy evolution. The pulsed electric field in (a) is based on the MSTFit results in (d). The CQL3D-predicted time behavior of the D⁺ energy in (b) does not match the Rutherford Scattering measurement of the perpendicular D⁺ temperature (e). CQL3D predicts anisotropy for C⁺⁶ ($T_{\parallel} > T_{\perp}$, panel (c)) opposite of the CHERS-measured anisotropy ($T_{\perp} > T_{\parallel}$, panel (f)).

of T_{\perp}) does not match the CQL3D model. As might be expected, the parallel electric field in CQL3D primarily drives acceleration in the parallel direction, and this energy couples into the perpendicular direction on a much slower time scale. With additional diffusion, it may be possible to sharpen the CQL3D W_{\parallel} decay time, but the true comparison with the W_{\perp} curve shows no similarities. Unfortunately, no T_{\parallel} measurement currently exists for the bulk ions.

The C^{+6} temperature tells a more intriguing story. Here, measurements do exist for both parallel and perpendicular components of the temperature, and an important previous result is an anisotropy in the heating, with $T_{\perp} > T_{\parallel}$. In CQL3D, the opposite is true. While the ion runaway model was able to closely match the measurements of fast ion acceleration in both the test particle and Fokker-Planck modeling, it is clearly not able to capture all of the dynamics of the bulk and impurity heating. Potential consequences and reasons for the disagreement will be discussed in the last section of this chapter.

Effects on thermal electrons

One might wonder, if the sawtooth electric field can accelerate ions so readily, what happens to the electrons? In the absence of collisions or other forces, a 50 V/m electric field would accelerate a thermal electron to relativistic speeds within a few microseconds. However, no significant hard x-ray flux (indicative of runaway electrons) is measured at a sawtooth crash; in fact, the Thomson scattering measurement of T_e typically goes down.

The answer is two-fold. The first explanation is tied into the discussion of why the ion temperature does not agree with the runaway model, and will be discussed in the next section. The other reason involves the greatly enhanced stochasticity of the magnetic field lines at the sawtooth crash. The Rechester-Rosenbluth model

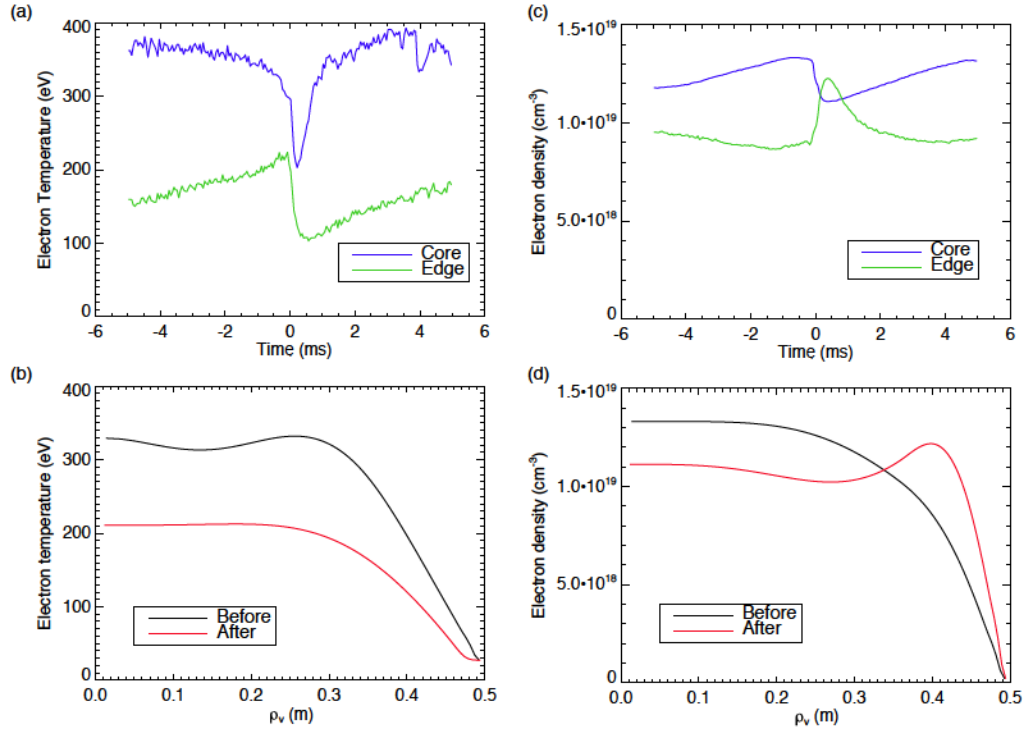


Figure 5.4: Electron temperature and density behavior throughout a time-series of MSTFit equilibria (constrained by Thomson scattering and FIR interferometer measurements). The electron temperature ((a) and (b)) decreases throughout the entire profile, while the electron density ((c) and (d)) decreases in the core and increases at the edge.

for electron heat transport and field line diffusion in a stochastic field states that $D_M \propto \tilde{b}^2$, and measurements have shown that in MST, heat diffusion indeed scales as $\chi \sim v_{\parallel} D_M \sim v_{\parallel} \tilde{b}^2$ [73, 74]. Not only does \tilde{b}^2 increase dramatically at the sawtooth crash, but if the electron parallel velocity is increasing due to the electric field, the transport of heat from the plasma core will be that much faster.

If this were the whole picture, one would then expect a corresponding decrease in the electron density. While there is some loss, it is balanced by the large influx of neutral gas and impurities from the edge of the plasma, providing an increase in the electron source term. Radial profiles of electron density from the FIR interferometer indeed show a decrease in the core electron density and an increase in the edge

(Figure 5.4).

These dynamics could in practice be modeled with CQL3D; however, greater precision is needed in our current estimates of electron diffusion and loss parameters. Trial runs (not presented here) indicate the modeling is very sensitive to these inputs and often predicts extreme degrees of electron runaway if not properly balanced by diffusion and loss. Moreover, as discussed in the next section, additional forces are likely at play that reduce the effective electric field felt by the electrons.

5.2 Discussion

Ion runaway in a pulsed, parallel electric field can fully describe the measured acceleration of fast ions, but fails to match observations of the bulk ions, impurities, and electrons. What differs between the fast ions and the thermal particles?

As mentioned back in Chapter 1, a large gyro-orbit combined with ∇B and curvature drifts allow fast ions to decouple from the magnetic field lines and develop a different rotational transform, q_{fi} . This improves their confinement compared to thermal particles, as the fast ion motion is not in resonance with the tearing mode magnetic fluctuations. This has a secondary effect when considering the parallel force balance of the particles. Mean-field Ohm's Law states:

$$\langle E \rangle_{\parallel} + \left\langle \tilde{\mathbf{v}} \times \tilde{\mathbf{B}} \right\rangle_{\parallel} - \frac{1}{en} \left\langle \tilde{\mathbf{J}} \times \tilde{\mathbf{B}} \right\rangle_{\parallel} = \eta \langle J \rangle_{\parallel} \quad (5.6)$$

If $\langle E \rangle_{\parallel} \simeq 50$ V/m and $\eta \langle J \rangle_{\parallel} \simeq 1$ V/m, the importance of the fluctuation-driven terms immediately becomes apparent. Modeling and measurements indeed show that the dynamo and Hall terms are extremely important to the overall force and momentum balance [75–77]. CQL3D does not include a fluctuating \tilde{b} term and thus does not include the physics necessary to self-consistently generate these forces. Because the fast, magnetically decoupled ions ignore the fluctuations, they can be modeled

accurately by both CQL3D and the test particle model using only the large-scale $\langle E \rangle_{\parallel}$. However, any attempt to model the thermal particles must include the interplay between the electric field and the other fluctuation-driven electromotive forces.

Ion runaway has also been observed in the MAST spherical tokamak [60], and differences between their observations and those made on MST further illustrate the importance of the correlated fluctuations in the RFP. In MAST, the ion distribution develops a high-energy tail after an internal reconnection event (a current driven instability similar to the RFP sawtooth). The electric field associated with these events lasts about 1 ms and peaks around 40 V/m. Hard x-rays with energies greater than 80 keV are also measured. Unlike in MST, all of the observed changes to the ion distribution function in MAST are explained by the ion runaway model. Although magnetic fluctuations are present during MAST reconnection events, the significant contribution of the $\langle \tilde{v} \times \tilde{b} \rangle_{\parallel}$ dynamo term is unique to the RFP and limits the direct acceleration of the thermal particles. Thus, ion runaway alone cannot explain ion heating in the RFP. Additionally, because electrons are the most closely coupled to the magnetic field lines, electron runaway from the sawtooth electric field is expected to be minimal in the RFP even though it is observed in MAST.

This raises several new and interesting questions: at what energy does a particle become “decoupled enough” to ignore the fluctuating electromotive forces and experience runaway? Can regimes be defined that determine the relative importance of other heating/energization mechanisms? What relevance does this have for reconnection heating theories concerning very high energy astrophysical particles?

As mentioned above, the deviation of the fast ion rotational transform from the magnetic field rotational transform may cause the fast ions to have a resonant n number that does not match the resonance of the magnetic field. Suppose that the fast ion and magnetic fluctuations can be described as:

$$\tilde{b} \sim \sin\left(\frac{n_1}{R}\phi\right) \quad (5.7)$$

$$\tilde{v} \sim \sin\left(\frac{n_2}{R}\phi + \delta\right) \quad (5.8)$$

Then after one toroidal transit,

$$\int_0^{2\pi} \tilde{v} \times \tilde{b} = 0 \quad \text{for } n_1 \neq n_2 \quad (5.9)$$

In reality, the fluctuations will consist of a sum over many n numbers, but this simplified example demonstrates how the separation of q_{fi} from q_m may lead to a reduction in correlated fluctuation effects for the fast ions. Other theories that may shed light on the decoupling condition include work by Mynick on gyroaveraging effects due to large Larmor radii [78] and work by Hegna on the separation of the fast particle guiding center from an equilibrium magnetic field line [79].

Finally, to develop a picture encompassing a wider range of the heating observations in MST, first consider previous results from Magee and Kumar [18, 41]. In both references, a model is presented in which the impurities are heated by a perpendicular mechanism such as ion cyclotron damping, and parallel heating is achieved through collisional isotropization. This model successfully reproduces a number of previous measurements, such as the $T_{\perp}^{C+6} > T_{\parallel}^{C+6}$ anisotropy, the scaling of that anisotropy with plasma density, and the Z/m dependence of parallel impurity heating.

Although there is currently no measurement of T_{\parallel} for the primary ion species, there are preliminary ANPA measurements on both the tangential and radial viewports of the non-Maxwellian tail generated at a sawtooth crash (Figure 5.5). Magee predicted this tail should extend out to at least 20 keV to account for the measured neutron flux [18], and ANPA measurements indicate signal up to that approximate energy range (though the noise floor is not well defined for these measurements). Without

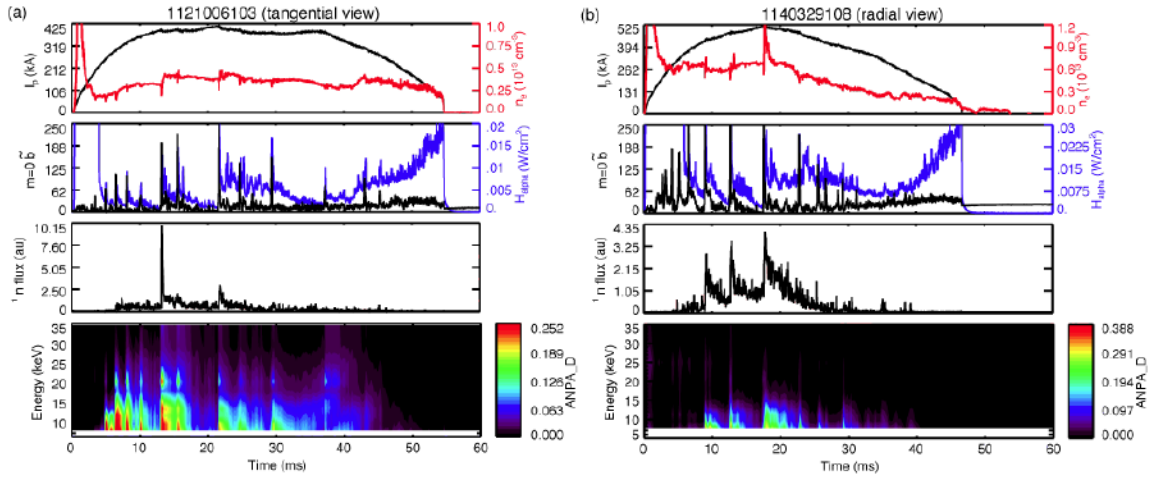


Figure 5.5: Without NBI, signals are measured during sawteeth on both the tangential (a) and radial (b) views. These figures should not be directly compared, as the plasma conditions are different and the tangential data is much older (from a time when the ANPA behavior and calibration was not as well understood). A more careful comparison of radial and tangential data should be conducted.

the large, core-localized NBI population, interpretation of the tangential view data becomes much harder, as the signal is likely dominated by charge exchange in the high neutral density edge of the plasma, and the ions that source those charge exchange products would need to have low (though nonzero) pitch. Thus, the tangential view cannot be interpreted as a purely parallel measurement, but rather as a convolution of high to low pitch measurements from the midradius to the edge. Nevertheless, the tangential view data suggests that there is some degree of parallel energization for the bulk distribution, and indeed Magee speculates that E_{\parallel} runaway could explain the observed non-Maxwellian tail [18].

Thus, a possible expansion of the Magee/Kumar picture would entail the perpendicular heating of the bulk deuterium distribution through some reconnection-based mechanism. Although thermal deuterium is not able to run away in the parallel inductive electric field due to opposing fluctuation-based electromotive forces, if a particle were able to pick up enough perpendicular energy to sufficiently decouple

from the magnetic fluctuations, the parallel runaway mechanism could take over, dragging those particles out into the non-Maxwellian tail.

Much of this discussion section is speculative, and many questions are left as future work. Those questions are strongly motivated by the findings of this thesis: a strong, parallel electric field clearly accelerates fast, NBI-sourced ions but has little or no effect on thermal ions. Multiple energization mechanisms, perhaps working synergistically, must be active and relevant for different classes of particles.

Chapter 6

Conclusions

6.1 Summary of key results

Decades after the initial observations, the mechanism responsible for anomalous ion heating during reconnection in laboratory and astrophysical plasmas remains elusive. Many experimental measurements have been made identifying key features of the process in the reversed-field pinch, including scaling with ion mass and charge-to-mass, directional anisotropy, and a high-energy, non-Maxwellian tail. Despite an abundance of possible theories explaining the process, no single theory has been able to fully describe all of the measurements.

This body of work contributes an additional experimental observation and guides future discussion of reconnection heating mechanisms by definitively identifying one ion energization process that is active during reconnection in the RFP while also showing that it must not be the only active process. Multiple heating and energization mechanisms must be active for ions in different regimes of magnetic coupling.

Development of the ANPA diagnostic

A key part of this work has been the development of the Advanced Neutral Particle Analyzer diagnostic. The ANPA utilizes a relatively compact and portable $E\parallel B$ design that is capable of time-resolved measurements of H and D energy distributions between 10-45 keV. Substantial work was required to calibrate and characterize the diagnostic, including in-depth modeling of convoluted signal contributions along the ANPA's line of sight. The model indicates the ANPA primarily measures core-localized, high-pitch NBI-sourced ions on its tangential viewport and low-pitch, spatially distributed fast ions on the radial viewport.

The ANPA has already been used in several other important studies of fast ion dynamics in the RFP, including measurements of fast ion loss rates associated with energetic-particle-driven modes [26], measurements of classical confinement for fast ions in standard and PPCD discharges [25], and a reduction of fast ion confinement in the 3D helical SHAx equilibrium [27].

Ion runaway during reconnection in the RFP

The primary experimental result of this thesis is the conclusive measurement of fast ion runaway during reconnection in the RFP. The ANPA was used to measure the change in the average energy of the fast ion distribution throughout a sawtooth reconnection event. Large quantities of data were obtained to characterize the energy gain in a variety of plasma and beam conditions. Figure 6.1(a) summarizes these measurements. When the direction of the electric field is reversed with respect to the fast ion motion, the ions decelerate rather than accelerate; this measurement rules out many other energization mechanisms and further demonstrates the intimate relationship between the fast ion energy and the inductive electric field.

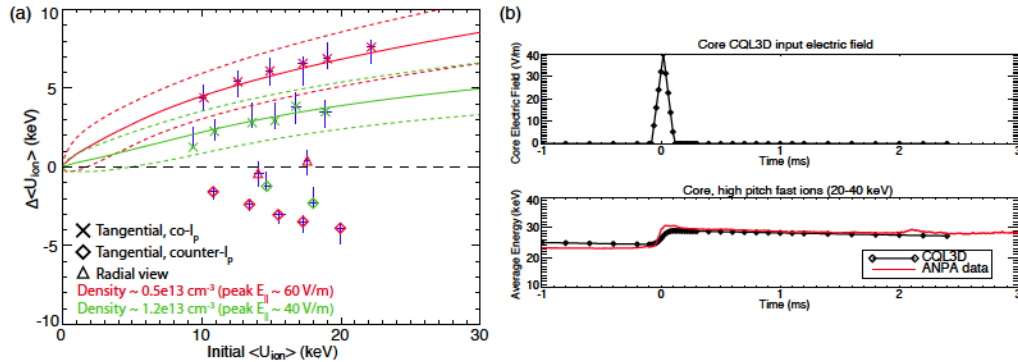


Figure 6.1: (a) Measurements agree well with test particle runaway modeling in a variety of conditions. (b) The CQL3D Fokker-Planck code evolves the entire fast ion distribution through the sawtooth electric field, also displaying good agreement with ANPA measurements.

The MSTFit equilibrium reconstruction code [61] was used to calculate the parallel electric field induced by the global magnetic flux change during a sawtooth event. This electric field was used with Furth and Rutherford’s formulation of ion runaway to estimate the expected acceleration of a fast test particle [59]. The ion runaway model agrees very well with measurements (Figure 6.1(a)). The evolution of the full fast ion distribution under the effects of a large pulsed electric field was also modeled using the CQL3D Fokker-Planck code [69]; this model also shows good agreement between measurements and electric-field-induced ion runaway (Figure 6.1(b)).

Applicability to thermal ion heating

Further modeling with CQL3D shows that ion runaway in a parallel electric field cannot explain previous thermal ion heating measurements, particularly the $T_{\perp} > T_{\parallel}$ anisotropic heating of C^{+6} impurities. This is contrary to a similar experiment in MAST in which ion runaway was determined to be fully responsible for all observed ion acceleration during internal reconnection events [60]. While the spherical tokamak also experiences magnetic fluctuations during reconnection, the significant correlation

of $\langle \tilde{v} \times \tilde{b} \rangle_{\parallel}$ is unique to the RFP. Additional fluctuation-driven electromotive forces must be considered for thermal particles, whereas the large orbit drifts of the fast ions allow them to ignore such forces. Because the direct runaway of the thermal ions is inhibited, their heating must be caused by some other reconnection-related process.

6.2 Suggestions for future work

Determining the threshold for runaway applicability

The most obvious question motivated by this research is: what is the condition that separates magnetically coupled ions (for which fluctuation-based electromotive forces must be considered) from decoupled, “fast” ions that can run away? Is there a sharp or gradual transition between the two regimes? A more careful scan of low beam energies could be performed, but the data in this thesis already pushes the lower bounds of the NBI and the ANPA measurement range. An upcoming modification to the CNPA [44] could allow for a high-resolution measurement at the energy range of interest (roughly 1-10 keV). An investigation should also be launched from the computation front. Full-orbit modeling using RIO [80] or in-house orbit tracking codes may be able to illuminate the energy at which ion orbits begin to decouple from field lines and magnetic perturbations.

Studies of core and edge reconnection events

Previous studies have shown drastically different behavior between the “normal” sawteeth studied in this thesis and two other cases: “core events” in which only the $m = 1$ tearing modes are active, and “edge events” in which only the $m = 0$ modes are active. Ion heating is absent during core events and is small and edge-localized during

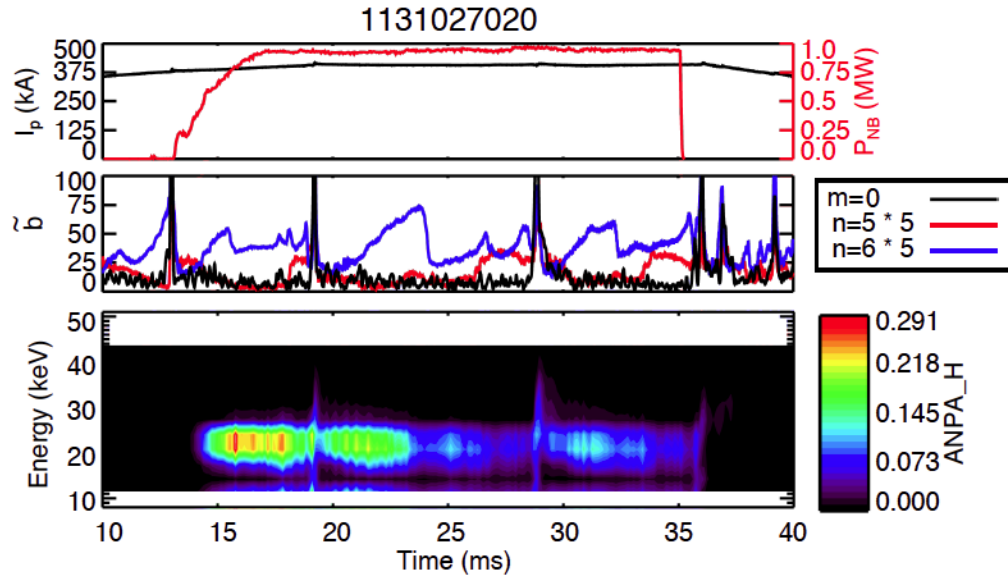


Figure 6.2: A core event occurs at 24 ms as the $n=6$ mode activity falls sharply after a gradual rise. There is no change in $m=0$ activity. The ANPA signal corresponding to beam-energy ions also drops off rapidly, and no acceleration is observed. Note that the amplitudes of the $n=5$ and $n=6$ mode amplitudes have been multiplied by 5 for visibility.

edge events [40].

ANPA signals corresponding to beam-energy ions typically drop in signal level after a core event (Figure 6.3). This is reminiscent of the behavior of the ANPA signal during QSH/SHAx [27]. It is unclear whether this is due to a loss of fast ion confinement or a shift in magnetic geometry yielding fewer orbits with favorable pitches for ANPA measurement. No acceleration of the fast ions is observed; this is consistent with the ion runaway mechanism as there is no change in stored equilibrium magnetic field energy and no change in magnetic flux. A careful ensemble of these events should be collected and characterized to learn more.

During edge bursts of $m=0$ activity in EC and $F=0$ plasmas, some enhancement of signal and small amounts of acceleration are observed, but no careful study has been performed. With smaller degrees of acceleration, more care needs to be taken

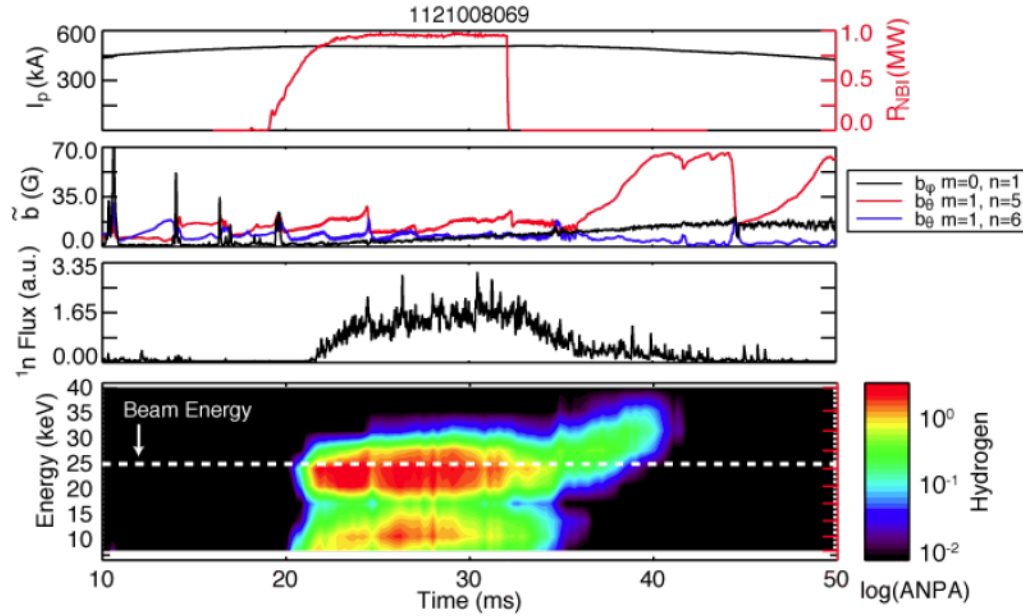


Figure 6.3: After NBI shuts off at 32 ms, the $n = 5$ amplitude begins to grow and significant ion acceleration is observed. The decay in neutron flux hesitates, reaching zero only after the remaining energized particles leave the plasma.

to properly eliminate noise and contributions from any increases in neutral density. Nevertheless, further study of these events is a very tractable problem.

Investigation of other energization phenomena

At the ends of SHAx and PPCD periods, acceleration of NBI-sourced ions is occasionally observed. The observations are inconsistent and occur most frequently during the ramp-down of the plasma current, a period that is typically not studied due to the rapidly changing equilibrium. It is possible that the decaying equilibrium generates an inductive electric field similar to a sawtooth event. These incidents should be cataloged more thoroughly, and equilibrium reconstructions may be beneficial in determining whether substantial electric fields are present.

Additionally, acceleration is observed during the ramp-up phase of QSH/SHAx,

as shown in Chapter 2. Again, this could be the result of an equilibrium change inducing an electric field, or it could be another process entirely. More study is needed to better understand these measurements.

Measurements of the high-energy tail

ANPA measurements of the sawtooth-generated fast ion tail (without NBI) may yield additional information about the mechanism that forms the tail. Using the ANPA's accelerating grid, the lower bound of the ANPA energy measurement can be brought as low as 5 keV, aligning nicely with the upper limit of the CNPA. Some measurements of the high-energy tail were already shown in Chapter 2. Thorough analysis of these measurements is difficult, however. Without the large population of core-localized NBI ions, signal levels are much lower and the origin of measured particles is likely from the high-neutral-density plasma edge. Because of the low signal levels, noise is a much bigger issue. The change in the background neutral density is also much more integral to the analysis.

To proceed with these measurements, further development of noise subtraction techniques and neutral density normalization is strongly encouraged. Without core NBI fast ions, a parallel measurement is exceptionally difficult, but comparisons of data between the radial and tangential ANPA views may yield interesting differences. The addition of a more powerful diagnostic neutral beam that would provide enough core neutral density for an active NPA measurement would be an expensive but effective way to enhance this measurement. The planned addition of an accelerating grid to the CNPA would also be beneficial for this study so that its energy range will better overlap with the ANPA and allow cross-calibration.

Development of additional ion diagnostics

Finally, the addition or development of new ion diagnostics is encouraged, though budgetary constraints are an obvious limitation. The most beneficial diagnostic would be a measure of the parallel bulk ion temperature to determine the heating anisotropy for the primary ion species. Additional Rutherford Scattering detectors could be installed with toroidal separation around the RS beam injector, allowing direct measurement of the core parallel temperature; however, this addition would require new holes to be drilled in the vacuum vessel.

Several other diagnostics would of course be useful. In the absence of funding limitations, a full wishlist of diagnostic improvements would include:

- As mentioned above, a parallel Rutherford Scattering measurement is essential to fully characterizing reconnection-driven ion heating.
- Additional neutron detectors with collimation would be useful to study the symmetry of neutron production during reconnection events.
- An array of solid-state NPA detectors could be used to gain more information about the spatial distribution of fast ions (with a loss in energy resolution).
- An improved mounting apparatus for the ANPA would allow reproducible, fine-tuned control of the ANPA sightline to better study spatial properties of the fast ion distribution.
- Improved measurement and modeling of the neutral density profile would raise confidence in the origin of measured NPA signals.
- A Fast Ion Loss Detector (FIELD) could be used to study loss orbits during magnetic activity.

- A DNB with higher current could provide an active ANPA view (either tangential or radial), greatly enhancing the spatial localization of the measurement.
- An off-axis NBI would allow sourcing of different fast ion distributions. This would have numerous scientific applications, one of which would be more control over the “test particles” used in energization studies.

Bibliography

- [1] B. Jones and R. Wilson. Spectroscopic studies of ion energies in ZETA. *Nuclear Fusion Supplement*, 3:889–893, 1962. (Cited on page 1).
- [2] R. B. Howell and H. J. Karr. Spectroscopic measurements of the plasma temperature in the ZT1 toroidal pinch. *Physics of Fluids*, 19(12), 1976. (Cited on page 1).
- [3] R. B. Howell and Y. Nagayama. Ion energy measurements on a reversedfield pinch experiment using Doppler broadening. *Physics of Fluids*, 28(2), 1985. (Cited on page 1).
- [4] G. A. Wurden, P. G. Weber, K. F. Schoenberg, A. E. Schofield, J. A. Phillips, C. P. Munson, G. Miller, J. C. Ingraham, R. B. Howell, J. N. Downing, and Others. Ion heating studies in the ZT-40M reversed field pinch. Technical report, Los Alamos National Lab., NM (USA), Dubrovnik, 1988. (Cited on page 1).
- [5] T. Fujita, K. Saito, J. Matsui, Y. Kamada, H. Morimoto, Z. Yoshida, and N. Inoue. Anomalous ion heating in REPUTE-1 ultra-low q and reversed field pinch plasmas. *Nuclear Fusion*, 31(1):3, 1991. (Cited on page 1).
- [6] J. W. Dungey. LXXVI. Conditions for the occurrence of electrical discharges in astrophysical systems. *Philosophical Magazine Series 7*, 44(354):725–738, 1953. (Cited on page 1).
- [7] E. G. Zweibel. The microphysics and macrophysics of cosmic rays. *Physics of Plasmas*, 20(5):055501, 2013. (Cited on page 1).
- [8] M. Øieroset, R. P. Lin, T. D. Phan, D. E. Larson, and S. D. Bale. Evidence for Electron Acceleration up to 300 keV in the Magnetic Reconnection Diffusion Region of Earths Magnetotail. *Physical Review Letters*, 89(19):195001, October 2002. (Cited on page 1).

- [9] R. P. Lin and H. S. Hudson. 10100 keV electron acceleration and emission from solar flares. *Solar Physics*, 17(2):412–435, 1971. (Cited on page 1).
- [10] A. A. Abdo, M. Ackermann, M. Ajello, A. Allafort, L. Baldini, J. Ballet, G. Barbiellini, D. Bastieri, K. Bechtol, R. Bellazzini, B. Berenji, R. D. Blandford, E. D. Bloom, E. Bonamente, A. W. Borgland, A. Bouvier, T. J. Brandt, J. Bregeon, A. Brez, M. Brigida, P. Bruel, R. Buehler, S. Buson, G. A. Caliandro, R. A. Cameron, et al. Gamma-Ray Flares from the Crab Nebula. *Science*, 331(6018):739–742, 2011. (Cited on page 1).
- [11] F. S. Mozer and P. L. Pritchett. Spatial, temporal, and amplitude characteristics of parallel electric fields associated with subsolar magnetic field reconnection. *Journal of Geophysical Research: Space Physics*, 115(A4), 2010. (Cited on page 1).
- [12] H. S. Hudson. Global Properties of Solar Flares. *Space Science Reviews*, 158(1):5–41, 2011. (Cited on page 1).
- [13] E. N. Parker. Intrinsic magnetic discontinuities and solar X-ray emission. *Geophysical Research Letters*, 17(11):2055–2058, 1990. (Cited on page 1).
- [14] E. R. Priest, C. R. Foley, J. Heyvaerts, T. D. Arber, J. L. Culhane, and L. W. Acton. Nature of the heating mechanism for the diffuse solar corona. *Nature*, 393(6685):545–547, June 1998. (Cited on page 1).
- [15] E. N. Parker. Sweet’s mechanism for merging magnetic fields in conducting fluids. *Journal of Geophysical Research*, 62(4):509–520, 1957. (Cited on page 1).
- [16] E. G. Zweibel and M. Yamada. Magnetic Reconnection in Astrophysical and Laboratory Plasmas. *Annual Review of Astronomy and Astrophysics*, 47(1):291–332, 2009. (Cited on pages 1, 11).
- [17] M. Yamada, R. Kulsrud, and H. Ji. Magnetic reconnection. *Reviews of Modern Physics*, 82(1):603–664, March 2010. (Cited on pages 1, 11).
- [18] R. Magee. *Ion energization during tearing mode magnetic reconnection in a high temperature plasma*. PhD thesis, University of Wisconsin - Madison, 2011. (Cited on pages 2, 12, 14, 98, 104, 104, 105).

- [19] D. C. Robinson and R. E. King. FACTORS INFLUENCING THE PERIOD OF IMPROVED STABILITY IN ZETA. Technical report, United Kingdom Atomic Energy Authority, Abingdon, Eng., 1969. (Cited on page 3).
- [20] J. Taylor. Relaxation of Toroidal Plasma and Generation of Reverse Magnetic Fields. *Physical Review Letters*, 33(19):1139–1141, 1974. (Cited on page 3).
- [21] R. Dexter, D. Kerst, and T. Lovell. THE MADISON SYMMETRIC TORUS. *Fusion Technology*, 19, 1991. (Cited on page 5).
- [22] J. Waksman, J. K. Anderson, M. D. Nornberg, E. Parke, J. a. Reusch, D. Liu, G. Fiksel, V. I. Davydenko, a. a. Ivanov, N. Stupishin, P. P. Deichuli, and H. Sakakita. Neutral beam heating of a RFP plasma in MST. *Physics of Plasmas*, 19(12):122505, 2012. (Cited on page 5).
- [23] J. Waksman. *Neutral beam heating of a reversed-field pinch in the madison symmetric torus*. PhD thesis, Univerisy of Wisconsin - Madison, 2013. (Cited on pages 5, 6, 137).
- [24] H. Sakakita, S. Kiyama, Y. Hirano, Y. Yagi, H. Koguchi, T. Shimada, Y. Sato, and K. Hayase. First Neutral Beam Injection Experiments in the TPE-RX Reversed-Field Pinch. In *30th EPS Conference on Contr. Fusion and Plasma Phys.*, number July, St. Petersburg, 2003. (Cited on page 5).
- [25] D. Liu, A. Almagri, J. Anderson, V. Belykh, B. Chapman, V. Davydenko, P. Deichuli, D. Den Hartog, S. Eilerman, G. Fiksel, C. Forest, A. Ivanov, M. Nornberg, S. V. Polosatkin, J. Sarff, N. Stupishin, and J. Waksman. Fast ion confinement studies in the MST reversed field pinch. In *38th EPS Conference on Plasma Physics*, volume 35G, page P2.101, Strasbourg, France, 2011. (Cited on pages 5, 7, 34, 46, 68, 75, 108, 137).
- [26] L. Lin, W. Ding, D. Brower, J. Koliner, S. Eilerman, J. Reusch, J. Anderson, M. Nornberg, J. Sarff, J. Waksman, and D. Liu. Measurement of energetic-particle-driven core magnetic fluctuations and induced fast-ion transport. *Physics of Plasmas*, 20(3):030701, 2013. (Cited on pages 5, 7, 40, 108).
- [27] J. Anderson, W. Capecchi, S. Eilerman, J. Koliner, L. Lin, M. Nornberg, J. Reusch, and J. Sarff. Fast ion confinement in the 3D helical RFP. *Plasma Physics and Controlled Fusion*, 56((accepted)), 2014. (Cited on pages 5, 9, 40, 50, 108, 111).

- [28] J. Koliner, C. Forest, J. Sarff, J. Anderson, D. Liu, M. Nornberg, J. Waksman, L. Lin, D. Brower, W. Ding, and D. Spong. Fast-Particle-Driven Alfvénic Modes in a Reversed Field Pinch. *Physical Review Letters*, 109(11):115003, September 2012. (Cited on pages 7, 40).
- [29] L. Lin, J. Anderson, D. Brower, W. Capecchi, W. Ding, S. Eilerman, C. Forest, J. Koliner, D. Liu, M. Nornberg, J. Reusch, and J. Sarff. Energetic-particle-driven instabilities and induced fast-ion transport in the reversed-field pinch. *Physics of Plasmas*, 21(5), 2014. (Cited on page 7).
- [30] J. Anderson, A. Almagri, D. Den Hartog, S. Eilerman, C. Forest, J. Koliner, V. Mirnov, L. a. Morton, M. Nornberg, E. Parke, J. Reusch, J. Sarff, J. Waksman, V. Belykh, V. Davydenko, A. Ivanov, S. V. Polosatkin, Y. Tsidulko, L. Lin, D. Liu, G. Fiksel, H. Sakakita, D. Spong, and J. Titus. Fast ion confinement and stability in a neutral beam injected reversed field pinch. *Physics of Plasmas*, 20(5):056102, 2013. (Cited on page 7).
- [31] G. Fiksel, B. Hudson, D. Den Hartog, R. Magee, R. OConnell, S. Prager, a. Beklemishev, V. Davydenko, A. Ivanov, and Y. Tsidulko. Observation of Weak Impact of a Stochastic Magnetic Field on Fast-Ion Confinement. *Physical Review Letters*, 95(12):125001, September 2005. (Cited on pages 9, 9, 88).
- [32] B. Hudson. *Fast Ion Confinement in The Reversed-Field Pinch*. PhD thesis, University of Wisconsin - Madison, 2006. (Cited on page 9, 9).
- [33] J. F. Drake, M. Opher, M. Swisdak, and J. N. Chamoun. A Magnetic Reconnection Mechanism for the Generation of Anomalous Cosmic Rays. *The Astrophysical Journal*, 709(2):963–974, February 2010. (Cited on pages 11, 83).
- [34] J. Egedal, W. Daughton, and a. Le. Large-scale electron acceleration by parallel electric fields during magnetic reconnection. *Nature Physics*, 8(4):321–324, February 2012. (Cited on page 11).
- [35] E. Scime, S. Hokin, and N. Mattor. Ion heating and Magnetohydrodynamic Dynamo Fluctuations in the Reversed-Field Pinch. *Physical Review Letters*, 68(14), 1992. (Cited on page 11).
- [36] M. S. Cartolano, D. Craig, D. Den Hartog, S. Kumar, and M. Nornberg. Statistical analysis of variations in impurity ion heating at reconnection events in

- the Madison Symmetric Torus. *Physics of Plasmas*, 21(1):012510, January 2014. (Cited on page 12, 12).
- [37] G. Fiksel, A. Almagri, B. Chapman, V. Mirnov, Y. Ren, J. Sarff, and P. Terry. Mass-Dependent Ion Heating during Magnetic Reconnection in a Laboratory Plasma. *Physical Review Letters*, 103(14):145002, September 2009. (Cited on pages 12, 14).
- [38] D. Den Hartog and R. Fonck. A fast spectroscopic diagnostic for the measurement of plasma impurity ion dynamics. *Review of scientific instruments*, 65(10), 1994. (Cited on page 12).
- [39] D. Craig, D. Den Hartog, G. Fiksel, V. Davydenko, and A. Ivanov. First charge exchange recombination spectroscopy and motional Stark effect results from the Madison Symmetric Torus reversed field pinch. *Review of Scientific Instruments*, 72(1):1008, 2001. (Cited on pages 12, 68, 98).
- [40] S. Gangadhara, D. Craig, D. Ennis, D. Den Hartog, G. Fiksel, and S. Prager. Ion heating during reconnection in the Madison Symmetric Torus reversed field pinch. *Physics of Plasmas*, 15(5):056121, 2008. (Cited on pages 12, 13, 111).
- [41] S. Kumar, A. Almagri, D. Craig, D. Den Hartog, M. Nornberg, J. Sarff, and P. Terry. Charge-to-mass-ratio-dependent ion heating during magnetic reconnection in the MST RFP. *Physics of Plasmas*, 20(5):056501, 2013. (Cited on pages 12, 104).
- [42] R. Magee, D. Den Hartog, S. Kumar, A. Almagri, B. Chapman, G. Fiksel, V. Mirnov, E. D. Mezonlin, and J. Titus. Anisotropic Ion Heating and Tail Generation during Tearing Mode Magnetic Reconnection in a High-Temperature Plasma. *Physical Review Letters*, 107(6):1–5, August 2011. (Cited on pages 12, 14, 50, 98).
- [43] E. D. Mezonlin, S. Roberson, C. Raynor, R. Appartaim, J. A. Johnson, V. I. Afanasyev, S. S. Kozlovsky, J. M. Moller, D. N. Hill, E. B. Hooper, H. S. McLean, and R. D. Wood. Neutral particle analyzer measurements on the SSPX spheromak. *Review of Scientific Instruments*, 78(5), 2007. (Cited on page 13).
- [44] J. Titus, E. D. Mezonlin, and J. A. Johnson III. Low Energy Ion Distribution Measurements in Madison Symmetric Torus Plasmas. *Journal of Applied Physics*, Submitted, 2014. (Cited on pages 13, 110).

- [45] V. A. Svidzinski, G. Fiksel, V. Mirnov, and S. Prager. Modeling of ion heating from viscous damping of reconnection flows in the reversed field pinch. *Physics of Plasmas*, 15(6), 2008. (Cited on page 14).
- [46] V. Tangri, P. Terry, and G. Fiksel. Anomalous impurity ion heating from Alfvénic cascade in the reversed field pinch. *Physics of Plasmas*, 15(11), 2008. (Cited on page 14).
- [47] S. S. Medley, a. J. H. Donné, R. Kaita, a. I. Kislyakov, M. P. Petrov, and a. L. Roquemore. Contemporary instrumentation and application of charge exchange neutral particle diagnostics in magnetic fusion energy experiments. *Review of Scientific Instruments*, 79(1):011101, January 2008. (Cited on page 15, 15).
- [48] S. V. Polosatkin, V. Belykh, and V. Davydenko. Neutral particle analyzer for studies of fast ion population in plasma. *Nuclear Instruments and Methods in Physics Research A*, pages 1–6, 2012. (Cited on page 16).
- [49] J. Reusch, J. Anderson, V. Belykh, S. Eilerman, D. Liu, G. Fiksel, and S. V. Polosatkin. Calibration of an advanced neutral particle analyzer for the Madison Symmetric Torus reversed-field pinch. *Review of Scientific Instruments*, 83(10):10D704, October 2012. (Cited on page 24).
- [50] B. Laprade and R. Starcher. The Development Of An Improved ElectronMultiplier For Mass Spectroscopy Applications. Technical report, BURLE Electro-optics, Inc. (Cited on page 32).
- [51] P. Beiersdorfer, a. L. Roquemore, and R. Kaita. Characteristics of compact solid-target charge exchange analyzers for energetic ion diagnostics on tokamaks. *Review of Scientific Instruments*, 58(11):2092, 1987. (Cited on page 33).
- [52] R. Goldston, D. McCune, H. Towner, S. Davis, R. Hawryluk, and G. Schmidt. New techniques for calculating heat and particle source rates due to neutral beam injection in axisymmetric tokamaks. *Journal of Computational Physics*, 43(1):61–78, September 1981. (Cited on pages 34, 95).
- [53] J. Sarff, N. Lanier, S. Prager, and M. Stoneking. Increased Confinement and β by Inductive Poloidal Current Drive in the Reversed Field Pinch. *Physical Review Letters*, 78(1):62–65, January 1997. (Cited on page 46).

- [54] R. Lorenzini, F. Auriemma, A. Canton, and L. Carraro. Particle transport in reversed field pinch helium plasmas. *Physics of Plasmas*, 13(11):112510, 2006. (Cited on pages 47, 132).
- [55] S. Eilerman and J. Anderson. Time-resolved ion energy distribution measurements using an advanced neutral particle analyzer on the MST reversed-field pincha). *Review of Scientific Instruments*, 6:3–6, 2012. (Cited on page 47).
- [56] P. Martin, L. Marrelli, G. Spizzo, P. Franz, P. Piovesan, I. Predebon, T. Bolzonella, S. Cappello, A. Cravotta, D. F. Escande, L. Frassinetti, S. Ortolani, R. Paccagnella, D. Terranova, the RFX team, B. Chapman, D. Craig, S. Prager, J. Sarff, the MST team, P. Brunzell, J.-A. Malmberg, J. Drake, the EXTRAP T2R team, Y. Yagi, et al. Overview of quasi-single helicity experiments in reversed field pinches. *Nuclear Fusion*, 43(12):1855, 2003. (Cited on page 49).
- [57] H. Dreicer. Electron and Ion Runaway in a Fully Ionized Gas. *Physical Review*, 115(2):238, 1959. (Cited on page 56).
- [58] H. Dreicer. Electron and Ion Runaway in a Fully Ionized Gas. II. *Physical Review*, 117(2), 1960. (Cited on page 57).
- [59] H. Furth and P. Rutherford. Ion runaway in tokamak discharges. *Physical Review Letters*, 28(February), 1972. (Cited on pages 57, 109).
- [60] P. Helander, L.-G. Eriksson, R. Akers, C. Byrom, C. Gimblett, and M. Tournianski. Ion Acceleration during Reconnection in MAST. *Physical Review Letters*, 89(23):235002, November 2002. (Cited on pages 59, 103, 109).
- [61] J. Anderson, C. Forest, T. Biewer, J. Sarff, and J. Wright. Equilibrium reconstruction in the Madison Symmetric Torus reversed field pinch. *Nuclear Fusion*, 44(1):162–171, January 2004. (Cited on pages 63, 109).
- [62] N. E. Lanier, J. K. Anderson, C. B. Forest, D. Holly, Y. Jiang, and D. L. Brower. First results from the far-infrared polarimeter system on the Madison Symmetric Torus reversed field pinch. *Review of Scientific Instruments*, 70(1):718, 1999. (Cited on pages 64, 66).
- [63] W. X. Ding, D. L. Brower, B. H. Deng, a. F. Almagri, D. Craig, G. Fiksel, V. Mirnov, S. C. Prager, J. S. Sarff, and V. Svidzinski. The Hall dynamo effect

- and nonlinear mode coupling during sawtooth magnetic reconnection. *Physics of Plasmas*, 13(11):112306, 2006. (Cited on pages 64, 66).
- [64] W. X. Ding, D. L. Brower, B. H. Deng, and T. Yates. Electron density measurement by differential interferometry. *Review of Scientific Instruments*, 77(10):10F105, 2006. (Cited on pages 64, 66).
- [65] D. J. Den Hartog, J. R. Ambuel, M. T. Borchardt, A. F. Falkowski, W. S. Harris, D. J. Holly, E. Parke, J. A. Reusch, P. E. Robl, H. D. Stephens, and Y. M. Yang. Pulse-burst laser systems for fast Thomson scattering. *Review of Scientific Instruments*, 81(10), 2010. (Cited on page 66).
- [66] J. C. Reardon, G. Fiksel, C. Forest, A. F. Abdrashitov, V. Davydenko, A. Ivanov, S. A. Korepanov, S. V. Murachtin, and G. I. Shulzhenko. Rutherford scattering diagnostic for the Madison symmetric torus reversed-field pinch. *Review of Scientific Instruments*, 72(1), 2001. (Cited on pages 68, 98).
- [67] J. Sarff and J. Laufenberg. Sawtooth detector circuit drawing. In *MST drawing library*, pages 10T03G-C-014-R01, 2006. (Cited on page 77).
- [68] F. E. Grubbs. Procedures for Detecting Outlying Observations in Samples. *Technometrics*, 11(1):1-21, 1969. (Cited on page 81).
- [69] R. Harvey and M. McCoy. The cql3d fokker-planck code. *Advances in Simulation and Modeling of Thermonuclear Plasmas*, (November), 1992. (Cited on pages 93, 109).
- [70] R. Harvey and M. G. Mccoy. The CQL3D Fokker-Planck Code. Technical report, CompX, 2011. (Cited on page 93).
- [71] R. Fowler, J. Holmes, and J. Rome. NFREYA: A Monte Carlo beam deposition code for noncircular Tokamak plasmas. Technical report, July 1979. (Cited on page 95).
- [72] J. A. Reusch. *Measured and Simulated Electron Thermal Transport in the Madison Symmetric Torus Reversed Field Pinch by*. PhD thesis, University of Wisconsin - Madison, 2011. (Cited on page 98).

- [73] A. Rechester and M. Rosenbluth. Electron Heat Transport in a Tokamak with Destroyed Magnetic Surfaces. *Physical Review Letters*, 40(1):38–41, 1978. (Cited on page 101).
- [74] T. Biewer, C. Forest, J. Anderson, G. Fiksel, B. Hudson, S. Prager, J. Sarff, J. Wright, D. Brower, W. Ding, and S. Terry. Electron Heat Transport Measured in a Stochastic Magnetic Field. *Physical Review Letters*, 91(4):045004, July 2003. (Cited on page 101).
- [75] D. Ennis, D. Craig, S. Gangadhara, J. Anderson, D. Den Hartog, F. Ebrahimi, G. Fiksel, and S. Prager. Local measurements of tearing mode flows and the magnetohydrodynamic dynamo in the Madison Symmetric Torus reversed-field pinch. *Physics of Plasmas*, 17(8):082102, 2010. (Cited on page 102).
- [76] T. D. Tharp, A. Almagri, M. Miller, V. Mirnov, S. Prager, J. Sarff, and C. C. Kim. Measurements of impulsive reconnection driven by nonlinear Hall dynamics. *Physics of Plasmas*, 17(12):120701, 2010. (Cited on page 102).
- [77] J. R. King, C. Sovinec, and V. Mirnov. First-order finite-Larmor-radius fluid modeling of tearing and relaxation in a plasma pinch. *Physics of Plasmas*, 19(5):055905, 2012. (Cited on page 102).
- [78] H. E. Mynick and J. Strachan. Transport of runaway and thermal electrons due to magnetic microturbulence. *Physics of Fluids*, 24(4):695, 1981. (Cited on page 104).
- [79] C. Hegna and A. Bhattacharjee. Suppression of the Tearing Mode by Energetic Ions. *Physical Review Letters*, 63(19):6–9, 1989. (Cited on page 104).
- [80] J. Reusch, J. Anderson, and Y. Tsidulko. Full particle orbit tracing with the RIO code in the presence of broad-spectrum MHD activity in a reversed-field pinch. *Nuclear Fusion*, (Special issue on energetic particles (accepted)), 2014. (Cited on page 110).
- [81] J. Anderson, P. L. Andrew, B. Chapman, D. Craig, and D. Den Hartog. Direct removal of edge-localized pollutant emission in a near-infrared bremsstrahlung measurement. *Review of Scientific Instruments*, 74(3):2107, 2003. (Cited on page 129).

- [82] J. Anderson. *Measurement of the Electrical Resistivity Profile in the Madison Symmetric Torus*. PhD thesis, University of Wisconsin - Madison, 2001. (Cited on pages 129, 130, 154).
- [83] K. Bockasten. Transformation of Observed Radiances into Radial Distribution of the Emission of a Plasma. *Journal of the Optical Society of America*, 51(9):943–947, September 1961. (Cited on page 131).
- [84] N. Lanier. *Electron Density Fluctuations and Fluctuation-Induced Transport in the Reversed-Field Pinch*. PhD thesis, University of Wisconsin - Madison, 1999. (Cited on page 131).
- [85] E. M. Jones and R. L. Freeman. *Atomic Collision Processes in Plasma Physics Experiments: Analytic Expressions for Selected Cross-sections and Maxwellian Rate Coefficients*. UKAEA, Culham Laboratory., 1974. (Cited on page 131).
- [86] M. Hughes and D. Post. A Monte Carlo algorithm for calculating neutral gas transport in cylindrical plasmas. *Journal of Computational Physics*, 28(1):43–55, 1978. (Cited on pages 132, 133).
- [87] J. P. Biersack and W. Eckstein. Sputtering studies with the Monte Carlo Program TRIM.SP. *Applied Physics A*, 34(2):73–94, 1984. (Cited on page 133).
- [88] V. D. Shafranov. EQUILIBRIUM OF A PLASMA TORUS IN THE MAGNETIC FIELD. *Atomic Energy*, 13, 1962. (Cited on page 135).
- [89] S. Kumar, D. Den Hartog, B. Chapman, M. O’Mullane, M. Nornberg, D. Craig, S. Eilerman, G. Fiksel, E. Parke, and J. Reusch. High resolution charge-exchange spectroscopic measurements of aluminum impurity ions in a high temperature plasma. *Plasma Physics and Controlled Fusion*, 54(1):012002, January 2012. (Cited on page 137).
- [90] S. Kumar, D. Den Hartog, K. J. Caspary, R. Magee, V. Mirnov, B. Chapman, D. Craig, G. Fiksel, and J. Sarff. Classical Impurity Ion Confinement in a Toroidal Magnetized Fusion Plasma. *Physical Review Letters*, 108(12):125006, March 2012. (Cited on page 137).
- [91] D. Stotler and C. Karney. Neutral Gas Transport Modeling with DEGAS 2. *Contributions to Plasma Physics*, 34(2-3):392–397, 1994. (Cited on page 140).

- [92] R. M. Magee, M. E. Galante, D. McCarren, E. E. Scime, R. L. Boivin, N. H. Brooks, R. J. Groebner, D. N. Hill, and G. D. Porter. A two photon absorption laser induced fluorescence diagnostic for fusion plasmas. *Review of Scientific Instruments*, 83(10), 2012. (Cited on page 140).

Appendix A

D_α emission measurements and neutral density modeling

A.1 Overview

While most plasma dynamics of interest stem from the charged electrons and ions, the background neutral atoms and molecules play several important roles; notably, they serve as a source term for thermal electrons and ions, and they are an important loss term for fast ions via the charge exchange process. Knowing the source and loss terms is vital for calculating the particle confinement time τ_p and particle diffusivity, important figures of merit for fusion plasmas. Knowing the background neutral density and the subsequent charge exchange rate is also critical for the analysis of several diagnostics, notably neutral particle analyzers (see Sections 2.4 and 2.5). Neutral particles also factor into collisional-radiative modeling of impurities and influence the thermal conductivity of the plasma.

Despite the importance of an accurate neutral density measurement, few diagnostics are designed to measure it. The technique used on MST and many other

magnetic confinement devices is based on measurements of the D_α or H_α emission line. D_α emission can occur when a neutral deuterium atom reaches an excited state, typically by collision with an electron. The Balmer-alpha line (n=3 to n=2) is the most common visible transition. The rate of D_α photon generation per unit volume γ_{D_α} can be calculated as:

$$\gamma_{D_\alpha} = n_0 n_e \langle \sigma v \rangle_{excitation} \quad (\text{A.1})$$

where n_0 is the neutral particle density, n_e is the electron density, and $\langle \sigma v \rangle_{excitation}$ is the reaction rate for electron impact excitation into the n=3 state.

If the D_α emission is known, one can easily obtain the electron source term from the same measurement. The source term S_e from electron impact ionization can be defined as:

$$S_e = n_0 n_e \langle \sigma v \rangle_{ionization} = \gamma_{D_\alpha} \cdot \frac{\langle \sigma v \rangle_{ionization}}{\langle \sigma v \rangle_{excitation}} \quad (\text{A.2})$$

The ratio of ionizations to excitations is roughly constant ($\simeq 11.8$) for MST parameters. Under the assumption that neutral deuterium ionization is the only electron source (i.e. neglecting impurities), a loss rate L_e and particle confinement time can also be calculated:

$$L_e = S_e - \frac{\partial n}{\partial t} \quad (\text{A.3})$$

$$\tau_p = \frac{\int n_e dV}{\int L_e dV} \quad (\text{A.4})$$

By considering the radial loss rate through a given flux surface, a radial diffusion coefficient can also be obtained:

$$\oint \Gamma_r^e dA = \int L_e dV \quad (\text{A.5})$$

$$D_r = \frac{\Gamma_r^e}{\nabla n_e} \quad (\text{A.6})$$

As part of this thesis, several major improvements were made to the estimate of neutral density in MST. The next section describes D_α hardware and calibration

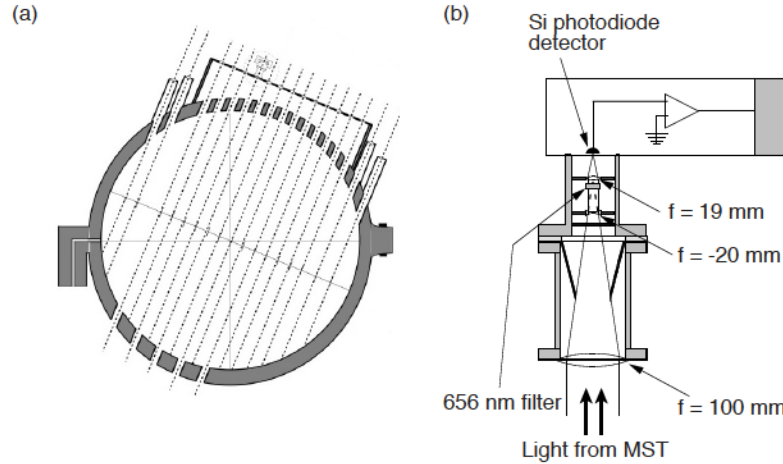


Figure A.1: (a) The bremsstrahlung/ D_α array has 17 viewing chords. 5 have matching ports on the opposite side of MST (currently plugged with view dumps). The four outer-most chords are not on the boxport and are separated 5° toroidally from the boxport chords. (b) The D_α detectors consist of a series of focusing optics, a silicone photodiode, and an I-to-V amplification circuit.

improvements, and Section A.3 details a new modeling code used to predict the neutral density based on D_α emission measurements.

A.2 Expansion and calibration of D_α detectors

D_α emission is measured on MST using an array of silicon photodiode detectors with bandpass filters centered on the D_α line (656.3 nm) [81,82]. The boxport for the array is located at 210T, ~ 10 -100P and was originally used for both D_α and bremsstrahlung emission measurements. Because of the shared boxport, only 7 of the 17 available viewing chords were fitted with D_α detectors. Through the course of this work, additional D_α detectors were constructed and used in place of the bremsstrahlung detectors, greatly enhancing the spatial resolution of the measurement. 16 detectors are now available, though at the time of writing, one is offline and another has been temporarily replaced with IDS optics. A diagram of the boxport and D_α detector

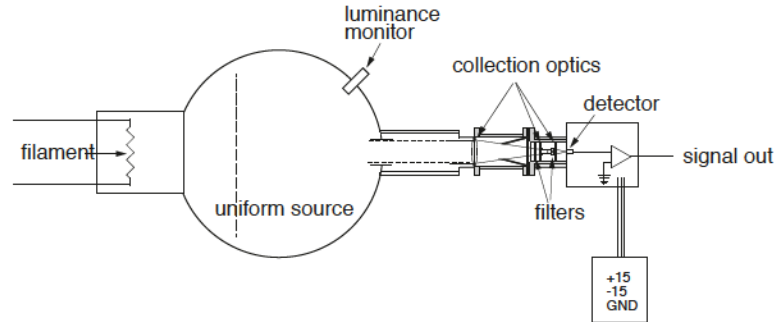


Figure A.2: Diagram of the D_{α} calibration setup

housing is shown in Figure A.1.

Full details of the detector hardware and calibration procedure are included in Anderson's thesis [82]; a brief summary will be presented here. The detectors are absolutely calibrated using a commercial, calibrated integrating sphere and a mockup of the path between MST's inner edge and the detector (Figure A.2). The integrating sphere emits a relatively uniform intensity of light across a wide wavelength spectrum and the bandpass filters have nonzero transmission from roughly 645-665 nm. This will cause error in the calibration if the intended measurement is precisely at 656 nm and the full transmission function is not accounted for. The transmission function for one of the filters in the initial batch of detectors was measured by Anderson, and initially this transmission curve was used for all detectors. However, it was discovered that the filters purchased for the new batch of detectors had significantly different transmission functions, and there was also variation from filter to filter. A high-resolution Ocean Optics HR200+ spectrometer was purchased to precisely measure the transmission of each individual filter (Figure A.3), providing a significant improvement in the accuracy of the calibration.

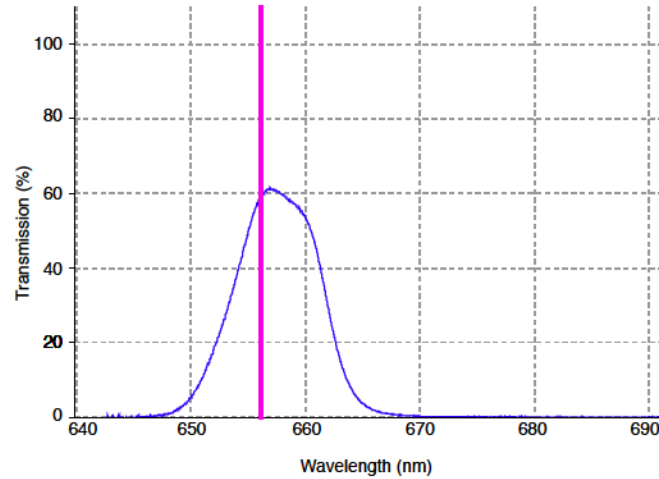


Figure A.3: The bandpass filter has significant transmission (blue) around the D_α line (purple).

A.3 NENE Monte Carlo code

Motivation

Prior to this work, an Abel inversion [83] was used to transform the collection of line-integrated D_α emission measurements into a radial emission map. Due to a consistent inboard-outboard asymmetry and the assumption that the outboard carbon limiter would source additional neutral atoms, an additional ad-hoc source of emission at the outboard midplane was added to the inversion results.

Neutral density profiles calculated with this method were consistently higher than expected. The extremely edge-peaked neutral density poses several problems: first, the core chords will be dominated by edge emission, causing difficulties in the inversion process. Second, $\langle\sigma v\rangle$ is flat for a large range of MST parameters [84, 85], but falls off by several orders of magnitude at the cold plasma edge where n_0 is highest (Figure A.4). When calculating n_0 from Equation A.1, $\langle\sigma v\rangle$ will appear in the denominator, and division by a rapidly-changing small number can lead to high

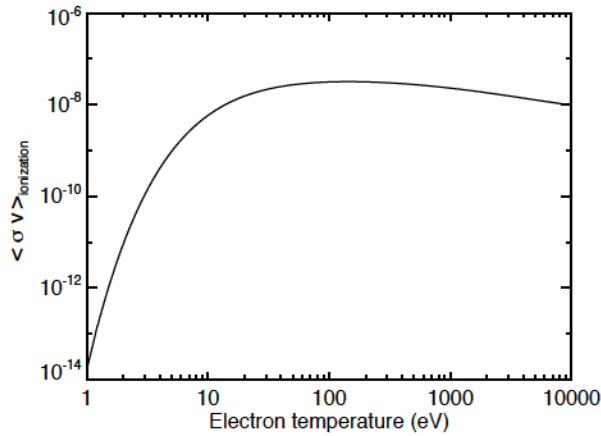


Figure A.4: $\langle \sigma v \rangle_{ionization}$ is relatively flat throughout most of MST parameter space, but falls off drastically at the cold plasma edge.

uncertainties.

These concerns motivated a new method of estimating the neutral density from the measured, line-integrated D_α emission. The NENE code, developed by R. Lorenzini and F. Auriemma at RFX, is a Monte Carlo code for tracking neutral particles through a plasma [54, 86]. By adjusting the input parameters, a number of realistic neutral density profiles can be calculated based on physical neutral sources. These profiles can then be compared against a synthetic D_α emission diagnostic, discussed later in this section.

Description of inputs, outputs, and particle tracking

NENE requires radial profiles of three plasma quantities as input: $n_e(r)$, $T_e(r)$, and $T_i(r)$. NENE has been integrated with the MSTFit equilibrium reconstruction code, and thus the necessary profiles are taken from the MSTFit output. n_i is assumed equal to n_e by quasineutrality, and the plasma is assumed to be toroidally symmetric.

Along with an input file describing basic machine geometry and parameters, the

user may also specify the source profile of neutral particles for each simulation. The source can be poloidally uniform or localized at a single poloidal location, and the neutrals can be sourced with a uniform energy or the energy can be calculated from plasma-wall interaction. Energy and particle reflection parameters must be input for the desired wall material; these parameters are typically calculated using the TRIM (Transport of Ions in Matter) code [87]. The user may also specify the ratio of atomic to molecular neutrals; for this work, only atomic neutrals are considered.

As described in reference [86], each of the sourced particles is tracked through the plasma, which is divided into many zones. Subtle Monte Carlo techniques are used to improve computational efficiency, but a generalized description of the particle tracking is provided here. In each zone, the mean free path is calculated, and thus the probability of collision within that zone can be found. A random number generator determines if the particle has a collision and what type of collision occurs (scattering or ionization). The particle is followed through a series of collisions until it is ionized or escapes the plasma. The particle contributes statistical information to each zone it passes through, not just its final location.

After the Monte Carlo process is complete, the code outputs the neutral density on a two-dimensional polar grid. Additional information such as cross sections for charge exchange and excitation are output on a radial grid.

Fitting to D_α measurements

Figure A.5 summarizes how NENE is used in conjunction with D_α emission measurements to estimate the neutral density profile in MST. For each fit, NENE is run three times with different neutral source profiles:

1. A poloidally uniform source with neutral energy determined by edge plasma

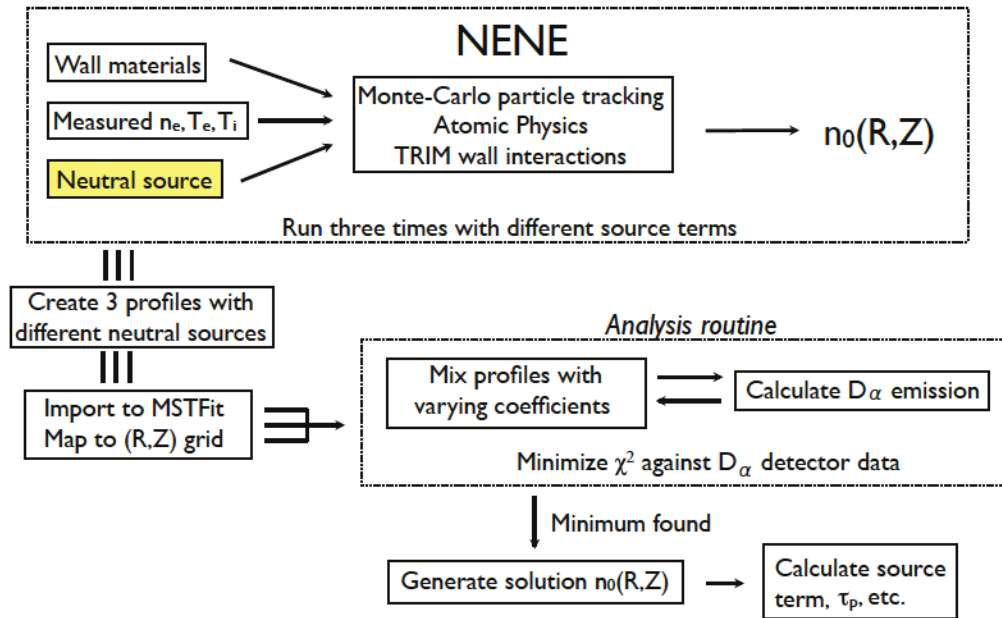


Figure A.5: Flowchart summarizing the interaction between NENE and D_α emission analysis.

interaction with aluminum

2. A poloidally localized source at the outboard limiter with neutral energy determined by edge plasma interaction with carbon
3. A poloidally uniform source with user-specified neutral energy (typically 1-25 eV, discussed later)

The first source is obviously a model of MST's aluminum wall, and the second models the carbon limiter. The third source is an ad-hoc source that produces neutrals with energies higher than source 1 for increased core penetration. While it does not correspond to a true physical source, it allows greater flexibility when matching to the D_α data.

Three separate neutral density profiles are output for the three sources. These are converted from the (r, θ) polar NENE grid to the (R, Z) grid used by MSTFit. The

three profiles are then used as neutral density basis functions and linearly combined such that:

$$n_0(R, Z) = \beta \sum_{i=1}^3 \alpha_i n_{0,i}(R, Z) \quad (\text{A.7})$$

where α_1, α_2 , and β are fit parameters that will be varied, and $\alpha_3 = 1 - \alpha_1 - \alpha_2$. The physical geometry of each D_α chord is mapped onto both the (R, Z) grid and the poloidal flux (ψ) grid used by MSTFit, and the simulated D_α emission is calculated along each detector chord:

$$\Gamma_{D_\alpha} = \int_L n_0(R(l), Z(l)) n_e(\psi(l)) \langle \sigma v(\psi(l)) \rangle_{excitation} dl \quad (\text{A.8})$$

The simulated D_α emission is compared to the measured D_α emission for each detector, and the reduced χ^2 is calculated:

$$\chi_{red}^2 = \frac{1}{(N_{meas} - 3)} \frac{(\Gamma_{D_\alpha}^{meas} - \Gamma_{D_\alpha}^{synthetic})^2}{\sigma_{meas}^2} \quad (\text{A.9})$$

where $(N_{meas} - 3)$ is the number of detectors used in the fit minus the three degrees of freedom in the fit. This procedure is repeated a number of times, varying the mixing coefficients of the three NENE profiles (α_i) and the total number of neutral particles (β) until χ_{red}^2 is minimized. After a best fit to the D_α data is found, the 2-D solution for the neutral density is calculated from Equation A.7.

Figure A.6 illustrates the fitting process. The neutral density, 2-D D_α emission, and line-integrated D_α emission are plotted for each basis profile. The last column shows the solution after linearly combining the profiles and minimizing against the D_α data (black points in bottom-right plot). Note that even though the D_α emission is higher on the outboard side, the fitting procedure often does not need substantial amounts of the poloidally localized profile; the Shafranov shift [88] of the electron

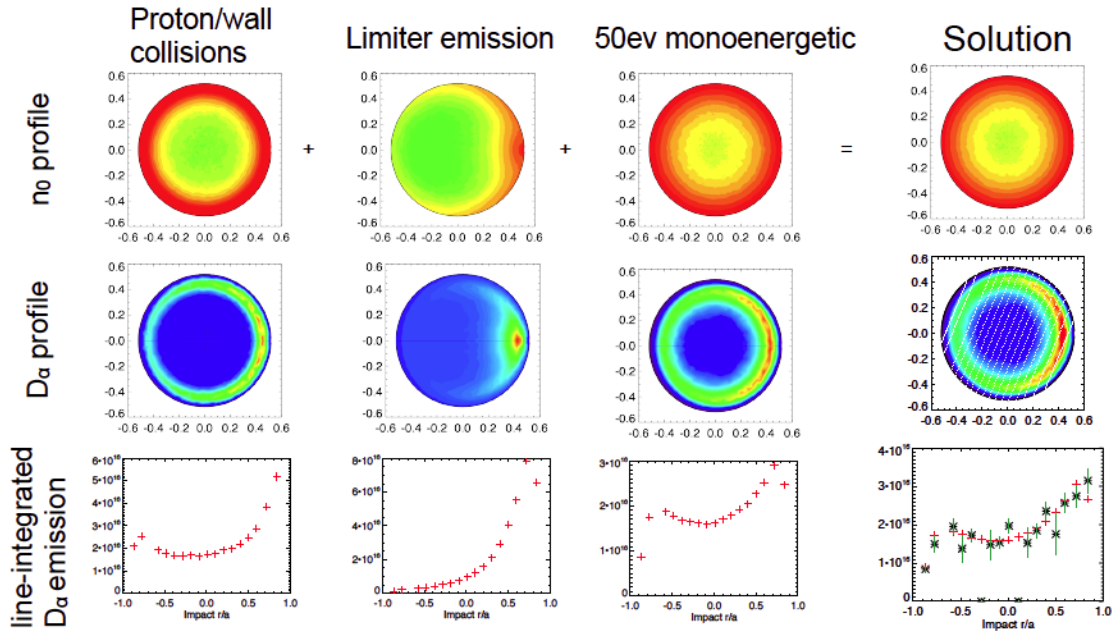


Figure A.6: n_0 and simulated D_α emission is plotted for three basis profiles (first three columns) and the data-constrained solution (last column, data in black).

density and temperature combined with a poloidally symmetric neutral density profile is often enough to reproduce the asymmetry in emission.

The increase in accuracy of the neutral density estimate is summarized in Figure A.7. The improvements in spatial resolution, calibration, and the transition from the direct Abel inversion to the NENE fitting procedure all improve the accuracy of the calculated neutral density profile.

Although computationally time consuming, MSTFit and NENE can be run for a series of equilibria to study the time behavior of the neutral density. A sample shot is shown in Figure A.8. Both the core and edge neutral density increase at sawtooth events and track well with the line-integrated D_α emission.

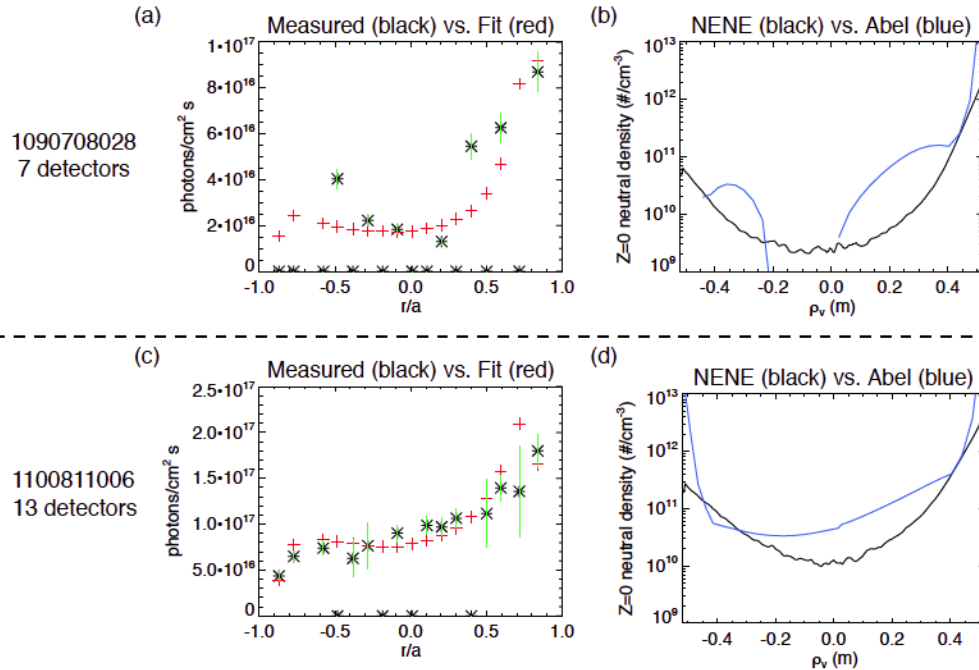


Figure A.7: Comparison of fit quality and midplane n_0 before and after improvement of the D_α array and fitting process. With only 7 detectors available, NENE does not match the D_α emission data well (a), but still produces a reasonable profile (b, black) when compared to the failed Abel inversion of the data (b, blue). When more detectors are available, NENE produces a profile much closer to the measurements (c), and the resulting profile (d, black) has substantially lower core neutral density than the Abel inversion (d, blue).

Uncertainty and comparison to other estimates

Despite the substantial improvement in the accuracy of neutral density fitting, there is still significant uncertainty in the calculated results, particularly in PPCD plasmas. In addition to the NPA modeling in this thesis, NENE neutral density profiles have been used in several other MST studies, including collisional-radiative modeling of impurities by Kumar [89, 90], and the calculation of fast ion loss rates due to charge exchange by Liu [25] and Waksman [23]. In order to match other data, reduction of the NENE core neutral density by factors of 2-30 were needed.

There are several possible reasons for the inaccuracy of the NENE profiles. The

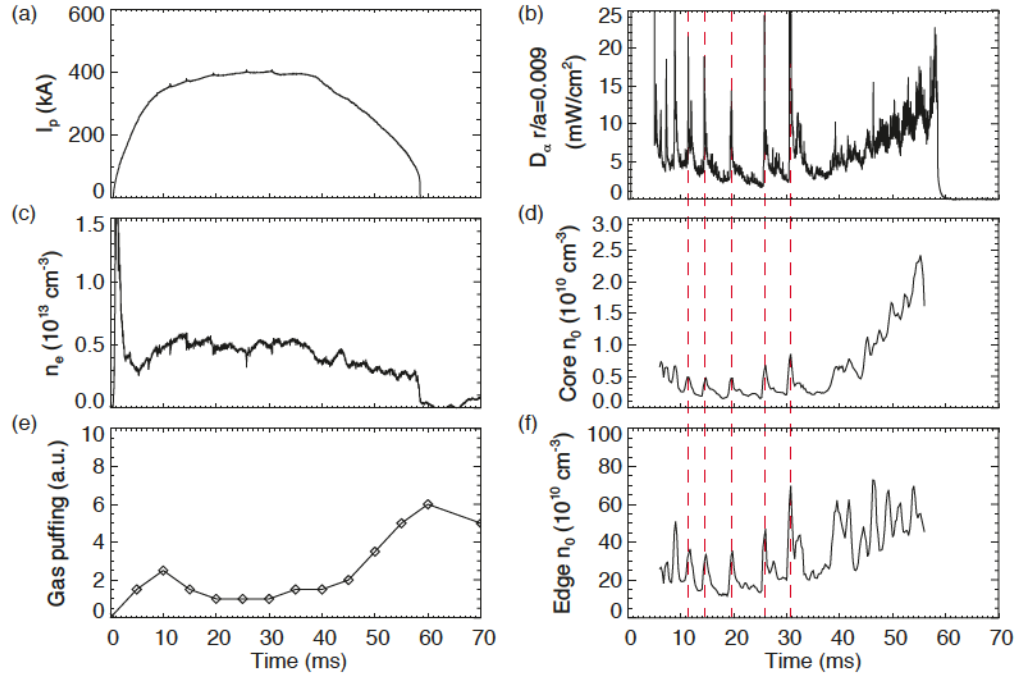


Figure A.8: The core (d) and edge (f) neutral density (as reconstructed by NENE at many time points) are plotted along with several other operational signals. Both quantities increase sharply at sawtooth events and generally follow the line-integrated D_α emission (b). The increase at the edge of the shot is due to increased puffing and ramp-down of the plasma current and temperature.

first is the same problem that was encountered with the Abel inversion: when line-integrated, the small amount of core D_α emission simply gets lost under the edge emission which is several orders of magnitude higher. Figure A.9 shows the core neutral density and χ_{red}^2 for several different NENE runs in which the neutral energy from the monoenergetic source was varied. While better fits to the D_α data are obtained for higher neutral energies, the energies used are unrealistically high; it's possible that the profiles corresponding to lower neutral energies produce more realistic profiles, and the data is simply not a good constraint.

The problem is likely exacerbated by the low signal level in PPCD. Neutral density and D_α emission drops substantially in PPCD as the better confinement limits plasma-wall interactions. The problem of core neutral density information being

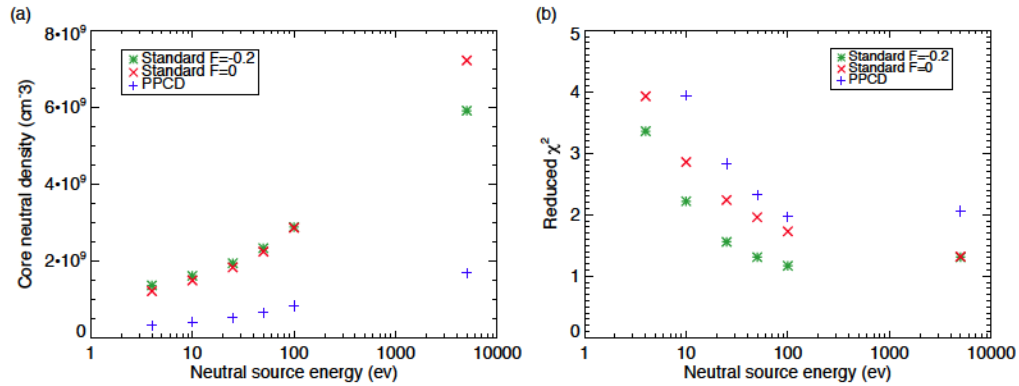


Figure A.9: With higher neutral source energy, the core neutral density increases (a) and the fit matches the data better (b). However, the high neutral energy and core density may be unrealistic. A default of 50 eV is used to compromise between fitting the data and modeling a relatively realistic neutral energy.

buried in an edge-peaked measurement is even harder to unravel when signal levels approach the noise floor.

Another possible reason for the inaccuracy is that NENE may not be able to fully model MST's neutral density profile. It is often suspected that the neutral density profile is toroidally asymmetric due to the poloidal gap and a variety of portholes and diagnostics scattered around the machine. The D_α measurement is at a single toroidal location which may not be representative of the plasma as a whole. Due to complications with the code and lack of measurement capabilities, NENE is not used to model molecular hydrogen which may factor into the observed emission. More complex physics like recombination and impurity interactions are also not modeled.

A.4 Summary and future work

Large steps have been taken to produce a more accurate estimate of the neutral density profile in MST. The number of active detectors was increased from 7 to 16,

nearly doubling the spatial resolution of the measurement, and the NENE Monte Carlo code was integrated with MSTFit to produce simulated neutral density profiles constrained by the available D_α emission data. Both of these improvements contribute to more consistent and accurate estimates of the core neutral density. Unfortunately, there is still significant uncertainty in the estimate, particularly in PPCD plasmas. Several suggestions for future work are offered if further refinement of the estimate is desired.

The DEGAS 2 code [91] has been licensed from PPPL but has not yet been implemented for MST. DEGAS 2 is a Monte Carlo neutral particle tracking code similar to NENE, but has seen extensive use (and thus development) in the tokamak community. A second estimation of the neutral density from a more sophisticated physics model would be extremely useful for comparison with NENE.

Another refurbishment of the D_α detector array would also be beneficial. In particular, the detectors need a larger dynamic range. This could be accomplished via improved amplification circuits or some method of adjustable gain (either an aperture or amplifier adjustment) so that the detectors could be tuned for particular run-day needs. The gain is currently set for a middle-of-the-road approach which results in complete saturation of the detectors in high-density plasmas and extremely low signals in PPCD plasmas. An adjustable gain would make calibration more challenging, but would greatly enhance the usefulness of the array. Additionally, the dynamic range varies from detector to detector due to mixing of old and new hardware, and some detectors have also developed oscillatory noise which should be diagnosed and repaired.

Other diagnostics capable of constraining the neutral density would obviously be advantageous. One example, the TALIF diagnostic [92], is capable of localized neutral density measurements. A direct measurement of the core neutral density

or even strong measurement constraints on the gradient in the mid-radius and edge would be the ideal method for further constraining the neutral density profile.

Finally, the use of Bayesian analysis techniques or integrated data analysis could facilitate a more accurate estimate neutral density profile as well as a better understanding of the uncertainty in the estimate.

Appendix B

Sign conventions in MSTFit, MDSPlus, and machine coordinates

B.1 Introduction

This appendix is intended to provide some insight and clarification about sign conventions used in MST and MSTFit for magnetic fields, electric fields, and voltages. It is not intended to be a comprehensive document, but rather a collection of notes that others may find useful should they need to perform calculations in which the directions of the fields become important.

First, a quick note on plasma current nomenclature. In many cases (MDSPlus database, MSTFit variable names, general discussion, etc.) the abbreviation I_p is used to represent the “plasma current” or the total current traveling in the toroidal direction. In the next section and in Figure B.1, I will take I_p to be the *poloidal* plasma current and I_t to be the toroidal plasma current, to match the typical abbreviations

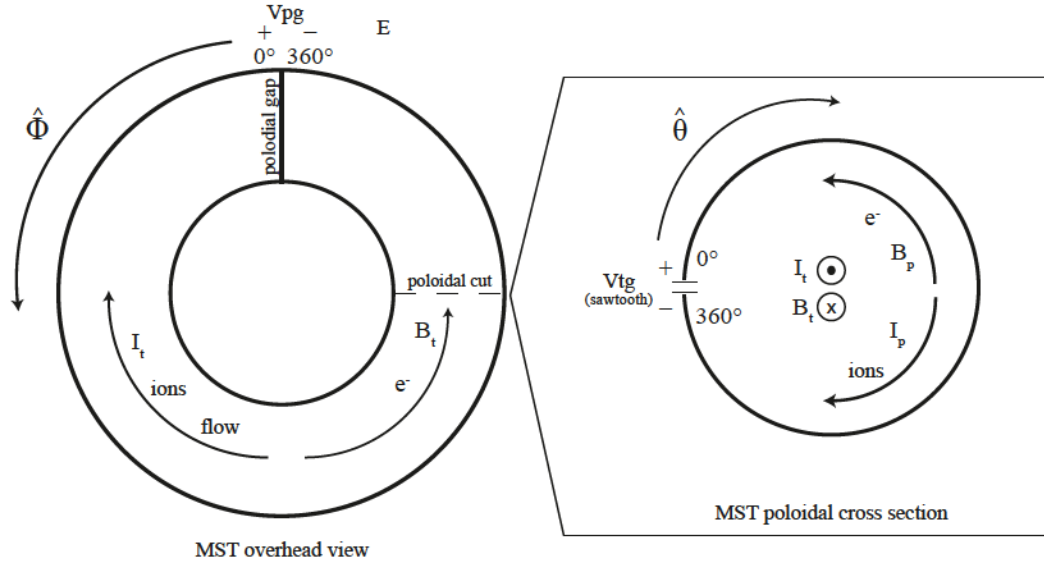


Figure B.1: Toroidal and poloidal cross-sections of MST with coordinate, current, field, and flow directions. Note that the $\hat{\theta}$ direction is the opposite of the convention used for porthole labels.

used for the magnetic field (B_t and B_p). At times, especially when discussing signal and variable names, it will be unavoidable to use I_p for the plasma current; I will try to be as explicit as possible in cases where the meaning is not clear.

B.2 MST sign conventions

We will first define the (R, θ, ϕ) coordinate system that will be used throughout this appendix and is the agreed-upon coordinate definition for MST. The major radius R is defined as one would expect, with the center of the torus being 0, the outer-most point on the shell being 2.52 m, and the direction \hat{R} pointing outward from the core. The poloidal coordinate θ is 0° right above the inboard midplane, 360° right below

the inboard midplane, and the direction $\hat{\theta}$ points clockwise (right-handed) if you are traveling in the $+\hat{\phi}$ direction. The toroidal coordinate $\hat{\phi}$ is 0° to the left of the poloidal gap (from an overhead perspective), 360° to the right of the poloidal gap, and the direction $\hat{\phi}$ points counter-clockwise if you are looking from above.

It is important at this point to note that a different convention for $\hat{\theta}$ is commonly used when discussing physical porthole locations. The portholes are labeled such that θ is 0° right above the outboard midplane, 360° right below the outboard midplane, and the direction $\hat{\theta}$ points counter-clockwise. Although more commonly used in conversation, these “machine coordinates” create a left-handed relationship between (R, θ, ϕ) and thus are not typically used for scientific calculations.

With our coordinate definitions in place, we can identify the directions of the primary plasma currents and magnetic fields during normal MST operation. During plasma startup, current is driven in the conducting shell to produce the toroidal magnetic field B_t in the $+\hat{\phi}$ direction. Once the main capacitor banks fire, a toroidal current I_t is inductively driven in the $-\hat{\phi}$ direction, creating a poloidal magnetic field B_p in the $-\hat{\theta}$ direction. During this process, the voltage across the poloidal gap V_{pg} is such that the electric field in the gap points in the $-\hat{\phi}$ direction (corresponding to an inductive loop voltage reinforcing the plasma current).

Away from sawteeth, the toroidal gap voltage V_{tg} is negative as the toroidal magnetic flux decreases, meaning that the electric field in the toroidal gap points in the $+\hat{\theta}$ direction. During a sawtooth, V_{tg} becomes positive as the toroidal magnetic flux increases, meaning that the electric field in the toroidal gap points from $+$ to $-$, or in the $-\hat{\theta}$ direction. Further clarification on the gap voltages is provided later in this appendix.

B.3 Sign inconsistencies in the MDSPlus database

At this point, I will explicitly mention several quantities that are “backwards” in the MDSPlus database and ops scopes. Often these quantities are more intuitive in their “backwards” form, but it is of course important to know whether a positive database signal corresponds to a positive or negative coordinate direction. Please note that this list is not comprehensive or complete, but simply includes the signals relevant to this thesis.

- “ I_p ” (the toroidal plasma current) is positive in the database although it travels in a $-\hat{\phi}$ direction.
- The convention used for V_{pg} is such that a positive value in the database corresponds to an in-gap electric field pointing in the $-\hat{\phi}$, $\text{co-}I_p$ direction (+ to – in Figure B.1).
- The convention used for V_{tg} is such that a positive value in the database corresponds to an in-gap electric field pointing in the $-\hat{\theta}$, direction (+ to – in Figure 1).
- Magnetic mode velocities (e.g. `bp_n06_vel`) are positive in the database although they actually travel with the plasma flow in the $-\hat{\phi}$ direction.

Reversing the direction of the plasma current (“counter-injection”)

The direction of the toroidal plasma current in MST can easily be switched by reversing the polarity of the current flowing through the PF windings. This setup is

often referred to as “counter-injection” because the fast ions injected with the NBI travel counter to the plasma current.

In counter-injection, the neutral beam injector is fixed and still injects ions in the $-\hat{\phi}$ direction, but the direction of “ I_p ” (I_t) is reversed ($+\hat{\phi}$). Since “ I_p ” generates the poloidal magnetic field B_p , it is also reversed. When we reverse “ I_p ”, polarity inverters are typically installed for I_p , I_{pri} , and V_{pg} . Therefore, **the signals in the MDS database do not change direction in “counter-injection” even though the real directions do change.** Be sure to identify and flip the signs of any of these polarity-inverted signals when used for calculations.

B.4 Sign conventions and inconsistencies in

MSTFit

The out structure

Let us first examine several elements of the `out` structure, which is defined on a 101-point 1-D flux surface grid and is used for many post-fit calculations. `out` contains flux-surface-averaged quantities as a function of normalized poloidal flux, and includes an effective radial coordinate ρ_V based on the square-root volume of a toroid projected from each poloidal flux surface.

- `out.ip` is a single positive number representing the toroidal plasma current “ I_p ” which is actually in the $-\hat{\phi}$ direction.
- `out.iphi` is an array of positive values representing the total toroidal plasma current enclosed by each flux surface. Like `out.ip`, a positive value corresponds to a current in the $-\hat{\phi}$ direction.

- `out.jphi` is an array of values for the parallel current density, $J_{\parallel} = \vec{J} \cdot \vec{B}$. These values are negative, which is correct since I_t and B_t (as well as I_p and B_p) are in opposite directions.
- `out.bp` is an array of values for the poloidal magnetic field on each flux surface. These values are positive and represent the magnitude of the poloidal field, although the direction of the real poloidal field is negative (B_p is in the $-\hat{\theta}$ direction).
- `out.bphi` is an array of values for the toroidal magnetic field on each flux surface. These values are positive, which is correct (B_t is in the $+\hat{\phi}$ direction).
- `out.psi` is an array of values for the poloidal magnetic flux enclosed by each flux surface. These values are negative which implies a $d\vec{A}$ element pointing in the $+\hat{\theta}$ direction.
- `out.phi` is an array of values for the toroidal magnetic flux enclosed by each flux surface. These values are positive which implies a $d\vec{A}$ element pointing in the $+\hat{\phi}$ direction.

The `bfield.pro` routine

The routine `bfield.pro` is an useful routine that will fetch the magnetic field at an (R, Z) point specified by the user, taking into account the inboard-outboard asymmetry due to toroidal effects. The routine returns a structure with the R , Z , and ϕ components of the magnetic field. While the B_{ϕ} component is correct, the B_R and B_Z components are backwards. When using this routine, if the correct direction of the R and Z components is important (i.e. you are not just going to square and add

them to get B_p), you should be sure to use code similar to the following:

```

bfield = bfield(in_r, in_z)
br = -bfield.r
bz = -bfield.z
bphi = bfield.phi

```

If you do square and add them to get B_p , you should remember that the result will be positive even though B_p points in the $-\hat{\theta}$ direction.

B.5 Calculating electric fields

The task of calculating the electric field and its direction at a sawtooth is what motivated this careful accounting of field signs. An abbreviated version of this derivation is given in Chapter 3, but a more detailed derivation is included here as well as an alternate derivation using magnetic fluxes instead of fields.

Using multiple MSTFit files to study time dependence

MSTFit is a single-time-point equilibrium, so the time derivative in the following equations will in practice be a finite difference between two different equilibria. However, we must be careful here, as the `out` array indices for two different equilibria will not necessarily correspond to the same flux surfaces. Indeed, I have found that throughout a sawtooth crash, the `out.area` value (which is a measure of the area enclosed by a given flux surface) changes substantially, enough to turn a drop in the core B into a positive flux change. To circumvent this, one should interpolate the values for the second equilibrium onto equivalent flux surfaces from

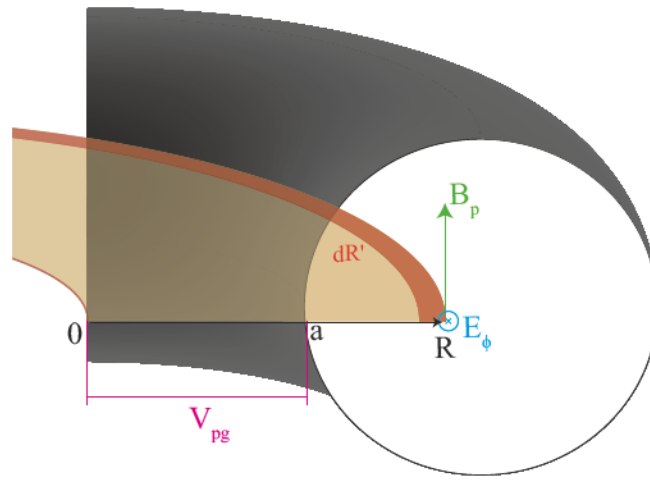


Figure B.2: Diagram showing the toroidal electric field generated by a change in poloidal magnetic flux.

the first equilibrium. `out.rhov` or `out.area` are good quantities to use for the interpolation.

Toroidal electric field using poloidal magnetic field

We begin with Faraday's Law in its integral form:

$$\oint \vec{E} \cdot d\vec{l} = -\frac{d}{dt} \int \vec{B} \cdot d\vec{A} \quad (\text{B.1})$$

If we wish to calculate the electric field in the toroidal direction E_ϕ at major radius R (and for simplicity, $Z=0$), we can consider the poloidal magnetic field B_p crossing through a disc of radius R :

$$\int_0^{2\pi} E_\phi R d\phi = -\int_0^R \int_0^{2\pi} \frac{\partial B_p}{\partial t} R' dR' d\phi \quad (\text{B.2})$$

Assuming toroidal symmetry and noting that $-V_{pg}$ is the voltage produced by the flux change between $R = 0$ and $R = R_0 - a$,

$$E_\phi(R, t) = \frac{1}{2\pi R} \left(V_{pg}(t) - 2\pi \int_{R_0-a}^R \frac{\partial B_p(R', t)}{\partial t} R' dR' \right) \quad (\text{B.3})$$

This is where we must begin being careful with signs and the information that we use. If we obtain the V_{pg} signal from the MDS database, we need to remember that a positive value is indicative of an electric field in the co-current $-\hat{\phi}$ direction. We should also be careful if we are using the `bfield.pro` routine from MSTFit and making assumptions about the midplane: for example, you could say that $B_p|_{z=0} = B_z$, but if you use the B_z output from `bfield.pro` without transforming it into a proper B_p , the sign will be incorrect. Thus, a correct expression for the toroidal electric field would be:

$$E_\phi(R, t) = \frac{1}{2\pi R} \left(-V_{pg}^{MDS}(t) + 2\pi \int_{R_0-a}^R \frac{\partial B_z^{\text{bfield.pro}}(R', t)}{\partial t} R' dR' \right) \quad (\text{B.4})$$

One final sign correction must be made. Once you cross the magnetic axis R_m , B_p at the midplane changes from the $-\hat{z}$ to the $+\hat{z}$ direction but our surface of integration remains in the same orientation. Although the direction B_p remains the same, the quantity $\vec{B} \cdot d\vec{A}$ changes sign. By making our equation piecewise, we arrive at a final expression for the toroidal electric field in terms of MDS and MSTFIT quantities:

$$E_\phi(R, t) = \begin{cases} R < R_m : \frac{1}{2\pi R} \left(-V_{pg}^{MDS}(t) + \right. \\ \quad \left. 2\pi \int_{R_0-a}^{R_m} \frac{\partial B_z^{\text{bfield.pro}}(R', t)}{\partial t} R' dR' + 2\pi \int_{R_m}^R \frac{\partial B_z^{\text{bfield.pro}}(R', t)}{\partial t} R' dR' \right) \\ R > R_m : \frac{1}{2\pi R} \left(-V_{pg}^{MDS}(t) + \right. \\ \quad \left. 2\pi \int_{R_0-a}^{R_m} \frac{\partial B_z^{\text{bfield.pro}}(R', t)}{\partial t} R' dR' - 2\pi \int_{R_m}^R \frac{\partial B_z^{\text{bfield.pro}}(R', t)}{\partial t} R' dR' \right) \end{cases} \quad (\text{B.5})$$

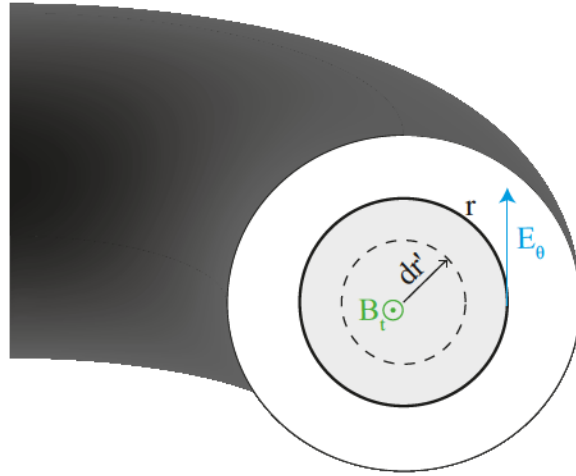


Figure B.3: Diagram showing the poloidal electric field generated by a change in toroidal magnetic flux.

Poloidal electric field using toroidal magnetic field

We now wish to calculate the poloidal electric field. Beginning again with Faraday's Law and considering the change in toroidal magnetic field through a circle in the poloidal plane:

$$\int_0^{2\pi} E_\theta r d\theta = - \int_0^r \int_0^{2\pi} \frac{\partial B_t}{\partial t} r' dr' d\theta \quad (\text{B.6})$$

The assumption of poloidal symmetry may not always be a good one due to $1/R$ effects, so we are left with:

$$E_\theta(r, t) = -\frac{1}{2\pi r} \int_0^r \int_0^{2\pi} \frac{\partial B_t(r', \theta, t)}{\partial t} r' dr' d\theta \quad (\text{B.7})$$

One can obtain the toroidal magnetic field from the `bfield.pro` routine or the `out` structure; both should have the correct sign, and the toroidal correction from `bfield.pro` will be averaged out in the integral.

Note that while we use the boundary condition V_{pg} in the toroidal electric field calculation, V_{tg} does not explicitly get used in the poloidal field calculation. However, you can still use it as a boundary value to check your work:

$$E_{\theta}(a, t) = -\frac{1}{2\pi a} \int_0^a \int_0^{2\pi} \frac{\partial B_t}{\partial t} r' dr' d\theta = V_{tg}(t) \quad (\text{B.8})$$

Using fluxes instead of fields

Because MSTFit has the toroidal and poloidal magnetic flux conveniently calculated, one may be tempted to use these quantities and skip some of the integration in the previous sections. I will briefly derive the electric field in terms of these fluxes and then explain why using the fields is the preferable method.

We begin again from Faraday's Law in terms of the total magnetic flux Φ_B :

$$\oint \vec{E} \cdot d\vec{l} = -\frac{d\Phi_B}{dt} \quad (\text{B.9})$$

If we wish to calculate the electric field in the toroidal direction E_{ϕ} at major radius R (and for simplicity, $Z=0$), we can consider the poloidal magnetic flux ψ crossing through a disc of radius R :

$$\int_0^{2\pi} E_{\phi} R d\phi = -\frac{d\psi}{dt} \quad (\text{B.10})$$

Our goal is to use the `out.psi` values from MSTFit. These values are defined on flux surfaces centered at `out.rsurf` with minor radius `out.rminor`. `out.psi` is defined to be zero at the wall, so we need to add the contribution from outside the vessel, which we already identified as V_{pg} . As a reminder, the `out` structures should all be interpolated to a single set of radial coordinates. I will use the notation R^* to

indicate the flux grid that we intend to use, and ψ^* will indicate that the flux has been interpolated onto a new flux surface grid. We now arrive at:

$$E_\phi(R, t) = \frac{1}{2\pi R} [(V_{pg}(t_2) - V_{pg}(t_1)) - (\psi^*(R^*, t_2) - \psi(R^*, t_1))] \quad (\text{B.11})$$

We can clean up the notation by using Δ to indicate the difference between two times points t_2 and t_1 :

$$E_\phi(R, t) = \frac{1}{2\pi R} [\Delta V_{pg}(t) - \Delta \psi^*(R^*, t)] \quad (\text{B.12})$$

Obtaining V_{pg} from the MDS database (and remembering to flip the sign), we can calculate the toroidal electric field as a function of **outboard** minor radius as:

$$E_\phi(r > R_0, t) = \frac{-\Delta V_{pg}^{MDS} - (\text{out.psi}^*(i^*, t_2) - \text{out.psi}(i^*, t_1))}{2\pi(\text{out.rsurf}(i^*) + \text{out.rminor}(i^*))} \quad (\text{B.13})$$

where i is the index of the **out** array corresponding to radius r . If we wish to look at the inboard sign of the machine, we simply need to change the sign in the denominator:

$$E_\phi(r < R_0, t) = \frac{-\Delta V_{pg}^{MDS} - (\text{out.psi}^*(i^*, t_2) - \text{out.psi}(i^*, t_1))}{2\pi(\text{out.rsurf}(i^*) - \text{out.rminor}(i^*))} \quad (\text{B.14})$$

The problem with this method arises from toroidal effects and flux surface averaging. Because $1/R$ is not constant around a flux surface, the expression $(\text{out.rsurf} - \text{out.rminor})$ is accurate in an average sense but not a local sense (in fact, the deviation is worst between the two midplane crossings which are the locations of interest). Using the flux surface averaged value ψ along with the flux surface averaged radii from **out** in Equations B.13 and B.14 will produce approximate but ultimately incorrect

values of the true $\vec{B} \cdot d\vec{A}$ as a function of R . This difference was discovered because the value of the calculated electric field did not reach the appropriate boundary condition ($V_{pg}/2\pi R$) at the plasma edge.

Following a similar derivation as the one we used for the toroidal electric field, one could obtain the following expressions for the poloidal electric field using the toroidal magnetic flux ϕ :

$$E_{\theta}(r, t) = \frac{1}{2\pi r}(\phi^*(r^*, t_2) - \phi(r^*, t_1)) \quad (\text{B.15})$$

$$E_{\theta}(r, t) = -\frac{(\text{out.phi}^*(i^*, t_2) - \text{out.phi}(i^*, t_1))}{2\pi \text{out.rminor}(i^*)} \quad (\text{B.16})$$

Because `out.rminor` is constant around a flux surface, we do not have the same flux surface averaging problem that we had with the toroidal electric field. However, there are additional complications from the change in the flux surface positions from one equilibrium reconstruction to the next. Until now, we have been interpolating each equilibrium onto a single MSTFIT grid. However, there is an additional term in E_{θ} relating to the shift in flux surface position that comes from taking the total time derivative of ϕ . For more information, see equations 6.11-6.13 in Jay Anderson's thesis (though, like everywhere else in life, several sign and algebra errors have been discovered in that derivation) [82]. It has been shown that for most cases this term is negligible, though it would be wise to confirm this for your particular case.

Due to these complications, I have chosen to use the magnetic fields from the `bfield.pro` routine and do the full integrations for both the poloidal and toroidal electric fields.

B.6 Clarification of gap voltage directions

One of the most confusing things while writing this document was the conventions used for the gap voltages V_{tg} and V_{pg} . My instinct when looking at the overhead layout of MST and the $+/-$ labels at the gaps was to interpret it as a circuit in which a voltage was applied at the gap with current flowing along the shell from $+$ to $-$. While currents do flow in the shell, the gaps are labeled such that the electric field in the gap points from $+$ to $-$. One can derive these field directions by considering integral form of Faraday's law (Eqn. B.9).

For example, to derive the direction of V_{tg} , consider the increase in toroidal flux at a sawtooth. From Eqn. B.9, the loop integral of $\vec{E} \cdot d\vec{l}$ must then be negative. If we consider $d\vec{l}$ to be positive as we travel across the gap in the $+\hat{\theta}$ direction, \vec{E} must then be pointing in the $-\hat{\theta}$ direction.

B.7 Sawtooth-generated electric fields with respect to NBI-born fast ions

The end goal for this work was to determine whether electric fields generated by magnetic equilibrium changes at a sawtooth event would accelerate or decelerate fast ions generated via neutral beam injection (NBI). In standard operation, NBI fast ions are injected co- I_t (counter- B_t). The ANPA-measured fast ions are core-localized and have a high negative pitch ($\gamma \equiv v_{\parallel}/|v|$); in other words, they will feel most of $E_{\parallel}(0)$ which will be largely toroidal. A more rigorous calculation of E_{\parallel} and its effects on fast ions is included in Chapter 3; here we will briefly get a qualitative sense of the field directions.

We first consider the toroidal electric field in Equation B.13 (although the flux

derivation is not used in practice, it is a bit easier to digest in terms of overall field signs). V_{pg}^{MDS} is a positive quantity and undergoes a negative then positive spike throughout the sawtooth, giving a small negative overall contribution to E_ϕ . `out.psi` increases at the sawtooth, giving another negative contribution to E_ϕ . Thus, E_ϕ is in the $-\hat{\phi}$ direction which will accelerate the NBI ions traveling in the $-\hat{\phi}$ direction.

If we want to also consider the contribution of the poloidal electric field, we examine Equation B.16. Although B_t in the core decreases at the sawtooth, `out.phi` is positive and increases at the sawtooth, so E_θ will be in the $+\hat{\theta}$ direction. The more detailed results in Chapter 3 indicate that towards the edge of the plasma, E_θ crosses zero and becomes negative.

In counter-injection, the neutral beam injector is fixed and still injects ions in the $-\hat{\phi}$ direction, but the direction of “ I_p ” (I_t) is reversed ($+\hat{\phi}$). Since “ I_p ” generates the poloidal magnetic field, it is also reversed. Thus, the absolute decrease in poloidal flux ψ produces a negative number rather than a positive one, resulting in a positive contribution to E_ϕ due to the negative sign in Faraday’s Law. This will outweigh the contribution from V_{pg} , resulting in an E_ϕ in the $(+\hat{\phi})$ direction. This will decelerate NBI fast ions. This matches ANPA observations in counter-injection.

B.8 Summary

- Magnetic fields and electron flows travel in the positive-coordinate directions.
- Currents and ion flows travel in the negative-coordinate directions.
- Electric fields at a sawtooth point co-current and accelerate NBI ions in standard-direction discharges.

- I_p , V_{pg} , and mode velocities are positive in the MDSPlus database even though they travel in negative-coordinate directions.
- In MSTFit, the R and Z components from `bfield.pro` are defined backwards, and care must be taken when using the various elements in the `out` structure to ensure the proper direction is understood (particularly with respect to the $d\vec{A}$ area element used for the fluxes).
- When taking a difference of `out.psi` and `out.phi` fluxes to get an electric field, you must first interpolate one of the equilibria onto the same flux surfaces as the other.